Collective forces and torques in active matter: The role of anisotropy

written by

Ashreya Jayaram

This dissertation is submitted to the Faculty of Physics, Mathematics and Informatics of Johannes Gutenberg University Mainz for the degree of "Doctor of Natural Sciences"

Mainz, August 2022

Abstract

Statistical mechanics played a key role in the development of modern physics. Going beyond equilibrium systems, the statistical description of non-equilibrium systems has gained significant attention. In particular, *active matter* has emerged as a paradigm to study the broader class of systems driven out of equilibrium. Motile active matter is composed of autonomous *active* "particles" which, unlike their passive counterparts, have a tendency to move persistently along the direction of preceding displacements. Ranging from nanomachines carrying cargo within our cells to human beings, such matter is ubiquitous in the natural world. Facilitated by advancement in fabrication techniques and computational capability, the past two decades have witnessed an enormous interest in understanding, engineering and controlling active matter.

This thesis explores the role of collective forces and torques in active matter with a focus on the effect of geometric anisotropy. In bulk, these forces and torques that result from a combination of propulsion and inter-particle interactions determine the collective behavior of active particles. Moreover, these can also be relayed to boundaries or objects suspended in active matter. The suspended object undergoes linear or angular propulsion depending on its shape. Microscopic engines that rotate in bacterial baths, for example, have been realized based on this principle. In this thesis, first, we study how the manifestation of collective forces and torques shapes the emergent phase behavior of ellipsoidal active particles. The resulting macroscopic structure is determined by how anisotropic the constituent particles are. Secondly, we probe into how an active fluid conveys forces onto passive objects immersed in it. We show that in a periodic system, the force on the object can be related to the vorticity of the polarization of the surrounding active fluid. Finally, we relate the origin of the force on an optically trapped probe in a confined active fluid to the microstructure of its neighborhood.

Zusammenfassung

Eine Schlüsselrolle bei der Entwicklung der modernen Physik spielte die statistische Mechanik, wobei in jüngerer Zeit die statistische Beschreibung von Nicht-Gleichgewichtssystemen große Bedeutung erlangt hat. Insbesondere aktive Materie hat sich hierbei als ein Paradigma für die Untersuchung der breiteren Klasse von Systemen erwiesen, die aus dem thermischen Gleichgewicht getrieben sind. Aktive Materie besteht aus autonomen Teilchen, die im Gegensatz zu ihren passiven Gegenstücken die Tendenz haben, sich in die Richtung der vorangegangenen Verschiebungen zu bewegen. Von Nanomaschinen, welche für Transportprozesse in unseren Zellen verantwortlich sind, bis hin zu Menschen sind solche Systeme in der natürlichen Welt allgegenwärtig. In den letzten zwei Jahrzehnten hat sich das Interesse am Verständnis, an der Entwicklung und an der Kontrolle aktiver Materie dank der Fortschritte bei der Herstellung und den Rechenkapazitäten enorm verstärkt.

In dieser Arbeit wird die Rolle von kollektiven Kräften und Drehmomenten in aktiver Materie untersucht, wobei der Schwerpunkt auf den Auswirkungen der geometrischen Anisotropie der Teilchen liegt. Diese Kräfte und Momente, die aus einer Kombination von Antrieb und Wechselwirkungen zwischen den Teilchen resultieren, bestimmen das kollektive Verhalten aktiver Teilchen. Darüber hinaus können sie auch auf Wände und Objekte, welche von aktiver Materie umschlossen sind, übertragen werden. Das Objekt erfährt je nach seiner Form eine gerichtete lineare oder Rotationsbewegung. Auf der Grundlage dieses Prinzips wurden z.B. mikroskopische Motoren realisiert, welche durch eine bakterielle Suspension in Rotation versetzt werden. In dieser Arbeit wird zunächst untersucht, wie kollektive Kräfte und Drehmomente das emergente Phasenverhalten ellipsoidischer aktiver Teilchen prägen. Die resultierende makroskopische Struktur wird dabei durch die Anisotropie der Teilchen bestimmt. Zweitens untersuchen wir, wie eine aktive Flüssigkeit Kräfte auf passive Objekte überträgt. Wir zeigen, dass in einem periodischen System die auf das Objekt wirkende Kraft mit der Wirbelstärke der Polarisation der umgebenden aktiven Flüssigkeit in Verbindung gebracht werden kann. Schließlich setzen wir den Ursprung der Kraft auf eine optisch gefangene Sonde in der Nähe einer begrenzenden Wand mit der Mikrostruktur der aktiven Flüssigkeit in Beziehung.

Contents

1 Introduction

When it is a matter of life and death, being out of equilibrium enables the former. Living things achieve this by constantly exchanging energy by eating food or absorbing sunlight, among other processes. A fundamental accomplishment of this exchange is the evasion of a lethal condition called *detailed balance* (or "reversibility of states") which stipulates that the flow of probability between any two states of the system is locally balanced. Because of the absence of a net probability flux between any two states [cf. fig. 1.1], a consequence of detailed balance is that any movie played forward could as well be played backward. This property is called *time-reversal symmetry*. Since banyan trees don't shrink to become seeds from which they developed, living organisms break time-reversal symmetry [1].

Physicists aim to develop a quantitative framework to describe the world. Equilibrium statistical mechanics, pioneered by Ludwig Boltzmann, lays down a link between the motion of several particles (atoms or molecules) and macroscopic thermodynamic properties like temperature. It dictates that the likelihood of any given state of a system that is coupled to a comparatively enormous heat bath is determined by its energy. More precisely, the probability distribution of states is governed by the Boltzmann distribution. Systems driven out of equilibrium, in general, neither heed to the Boltzmann distribution nor obey detailed balance.

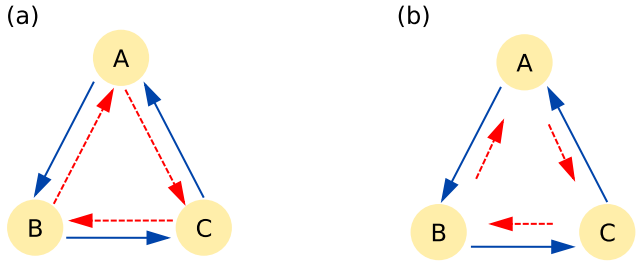

Figure 1.1.: (a) Transitions between states (A, B and C) are balanced in thermal equilibrium, prohibiting net fluxes (represented by length of arrows). (b) Since non-equilibrium systems violate detailed balance, they can manifest flux loops.

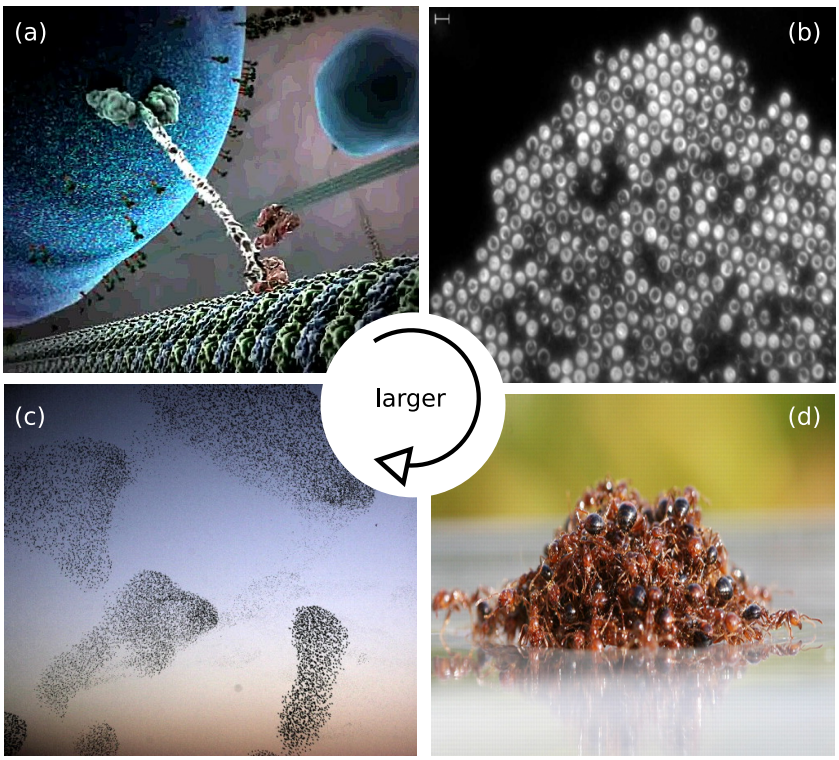

Figure 1.2.: Active matter in nature. (a) Cartoon of a motor protein transporting cargo by walking along a microtubule. Shown is a screenshot captured from a video titled 'The Inner Life of the Cell' created by XVIVO. The video is available at https://xvivo.com/examples/the-inner-life-of-the-cell/. (b) *Living crystal* composed of Thiovulum majus, a bacterium that can swim as fast as 60 body lengths per second. Reproduced from Ref. [5]. (c) A picturesque murmuration of starlings. Photo courtesy: FP6-NEST 12682 STARFLAG project, INFM-CNR. (d) A floating raft formed by a colony of fire ants. Reproduced from Ref. [6].

An early take on understanding life (or 'foci of activity' as Isaac Newton called it [2]) from a physicist's perspective was put forth by Erwin Schrödinger. In the monograph titled *What is life* [3], he underscores the importance of addressing this question from the standpoint of statistical physics and points out the failure of conventional equilibrium approaches. Often motivated by biology, since the latter half of the 20$^{\text{th}}$ century, huge efforts have been directed toward building a conceptual framework that describes systems out of equilibrium (see Ref. [4] for a review).

Capabilities like adaptation, self-replication, evolution and motility differentiate living organisms from inanimate matter. By deliberately ignoring every other aspect of an organism apart from the fact that it self-propels, one can contrive it as an agent which transforms free energy[1] to perform work on the environment in addition to

[1] In living organisms, energy is typically made available by hydrolyzing a nucleoside tri-phosphate into its corresponding di-phosphate. Most commonly, this nucleoside is adenosine.

producing heat as a by-product. Any material composed of these active agents is termed *active matter*[2]. What distinguishes active matter from other driven systems like a fluid under shear is that the source of energy is localized to the agent as opposed to energy provision at boundaries or through externally applied fields. By using energy from the local reservoir, these agents move in a directed manner despite being in a stochastic environment. This ability is important for nutrition search [7, 8], escape from predators and migration to better-suited environments [9].

Why does active matter matter? Apart from its evident prevalence in nature from load-carrying proteins in our cells to shoals of fish [cf. fig. 1.2], active systems serve as 'lab rats' whose understanding could unravel general features of non-equilibrium systems. For one, the fluctuations in particle number are *giant*[3] and its statistics deviates strongly from what one would expect from the law of large numbers [10, 11]. For another, they exhibit exotic phases like flocking that are inaccessible in thermal equilibrium [12, 13, 14]. Controllable and biocompatible active matter can be used for targeted delivery of drugs [15]. The use of active particles in decontamination of water and soil is being investigated with fervor [16]. Hence, active matter, over and above providing an avenue to explore non-equilibrium physics, can aid in progressing toward a healthier and more environmentally sustainable society.

Trying to reason the behavior of active matter has motivated the development of experimental and theoretical model systems, some of which are shown in fig. 1.3. Biomimetic active particles like artificial flagella driven by an oscillatory external magnetic field [20] and platinum-loaded stomatocytes powered by the catalysis of hydrogen peroxide [21] have been experimentally realized. At the microscale, active particles with fundamentally novel designs have also been conceived. An early invention is that of a Janus particle with gold and platinum segments [17]. When immersed in a solution of hydrogen peroxide, the platinum side catalyses the redox decomposition of peroxide into water and oxygen [cf. fig. 1.3 (a)]. The gold side is inert. This leads to the propulsion of the immersed particle through self-diffusiophoresis. The concept of using two-faced Janus particles with materials of different properties has been extended to drive particles through other mechanisms like thermophoresis [22] and electrophoresis [23]. Following a different route, colloidal particles can also be rendered active through Quincke rotation [24].

[2] Strictly speaking, active matter need not always be motile. However, in this thesis, we will restrict ourselves to the subclass of self-propelled active matter.

[3] As opposed to the expectation of $\sqrt{(N-\langle N\rangle)^2} \propto \sqrt{\langle N\rangle}$ from central limit theorem, the root-mean-square fluctuations of particle number N in active fluids $\sqrt{(N-\langle N\rangle)^2} \gg \sqrt{\langle N\rangle}$.

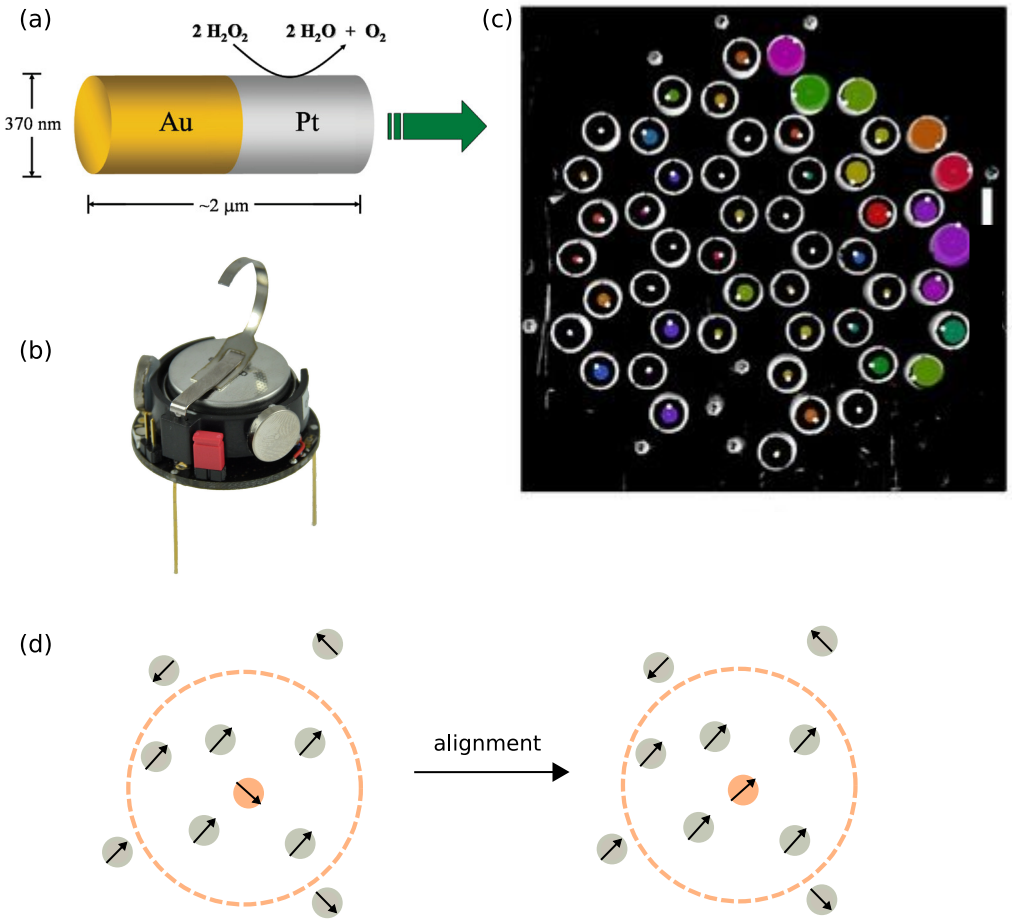

Figure 1.3.: Artificial models of active matter. (a) Sketch of a self-propelled Janus particle fuelled by the decomposition of hydrogen peroxide. Reproduced from Ref. [17]. (b) A three-legged kilobot capable of rotation and translation enabled by the action of two vibration motors powered by a lithium-ion battery. Reproduced from Ref. [18]. (c) An active metamaterial composed of motorized, fast spinning gyroscopes. Reproduced from Ref. [19]. (d) Depiction of the Vicsek model. The tagged particle (in orange) aligns to the mean orientation of all particles within an interaction radius (marked here with a dashed circle). It is unaffected by those outside.

On the computational front, broadly, there are two flavors of modelling active matter, *viz.*, *dry* models which disregard hydrodynamic interactions and *wet* models which explicitly resolve particle-fluid coupling. Since active particles are typically immersed in a fluid at a non-zero temperature, in addition to self-propulsion, they are subjected to rotational and translational diffusion. Dry models are employed to describe systems like dense bacterial suspensions in which steric interactions and stochastic effects overpower hydrodynamic interactions. A popular dry model is that of active Brownian particles [25, 26] that propel along their orientation vectors. Due to rotational noise, the direction of propulsion continuously reorients. Another way of modelling active particles is by treating them as run-and-tumble particles [27] which "run" in straight lines before reorienting during a "tumble". Active Ornstein-Uhlenbeck particles [28] that are subject to stochastic propulsion forces with temporally decaying correlations are yet another way to mimic active particles. More recently, kinetic Monte Carlo algorithms have also been put forth [29]. In contrast to the aforementioned dry models, wet models conserve momentum. The latter commonly treat active particles as force dipoles [30] or *squirmers* [31, 32] with an inhomogeneous surface slip velocity. The fluid can be considered using mesoscopic simulation techniques like the lattice-Boltzmann method [33] or multiparticle collision dynamics [34].

Alongside simulations and experiments, active matter has also been studied from a theoretical standpoint. A quintessential example is the bottom-up, mean-field theoretical description of motility-induced phase-separation (MIPS) in which a collection of interacting active particles separate into coexisting dense and dilute phases [35]. Another approach is to employ phenomenological field theories that describe the evolution of order parameter fields based on underlying symmetries [36]. Terms that break time-reversal symmetry and allow for steady-state currents are deliberately introduced. Such theories also explain characteristic features of scalar active matter like MIPS, albeit from a top-down perspective. Identifying the microscopic origins of parameters that enter field theories is a problem of contemporary interest.

In this thesis, we explore collective forces and torques in active matter using active Brownian particles as the model of our choice. We address different problems through numerical simulations and mean-field theory. The fundamentals of these techniques are provided in chapter 2. Bridging between scalar and polar active matter, in chapter 3, we study the effect of the aspect ratio of particles on the collective behavior of self-propelled ellipses through numerical simulations. Moreover, we

use mean-field theory to rationalize the emergence of these qualitatively different phases. Inspired by the ability of active particles to act as a working fluid that drives microscopic engines [37], in chapter 4, we develop a theory (backed by simulations of active Brownian particles) to understand how active particles transmit forces onto immersed passive objects. In the process, we cultivate the concept of an active stress which we then apply in chapter 5 to an experimental system of an optically trapped probe immersed in a confined active fluid.

2 Background

In this chapter, we lay conceptual foundations upon which the following chapters rely. We begin by discussing the concept of Brownian motion. We then introduce active Brownian particles and discuss how their hallmark property of motility-induced phase separation can be obtained in numerical simulations and understood using mean-field theory.

2.1 A particle in a fluid

Let us consider a 'large' colloidal particle immersed in a fluid maintained at a non-zero temperature T. The fluid is composed of particles (atoms) that are orders of magnitude smaller than the colloid. When viewed under a microscope, one sees that the colloid moves haphazardly. This apparently random movement of the colloid is an example of Brownian motion[1]. In this section, we formulate a theoretical description of such motion.

2.1.1 Langevin equation

The position vector of the colloid $\mathbf{r}$ evolves according to Newton's second law of motion

$$m\ddot{\mathbf{r}} = \mathbf{F}_{\text{net}} \tag{2.1}$$

where m is the mass of the colloid and $\mathbf{F}_{\text{net}}$ is the net force it experiences due to interactions with its surrounding fluid.

In principle, if we know the force that every particle in the fluid exerts at all times, the motion of the colloid can be exactly calculated using eq. (2.1). Since obtaining

[1] named after Robert Brown who observed the jittery motion of crushed pollen grains suspended in water under the microscope. He attributed this motion to an *active force* embedded in pollen. [38]. Albert Einstein's work [39] later corrected this view.

the exact value of $\mathbf{F}_{\text{net}}$ is often impractical and not very enlightening, we forgo this laborious pursuit of retaining all the degrees of freedom. The dynamics of the colloid can be alternatively modelled using a phenomenological stochastic differential equation called the *Langevin equation*

$$m\ddot{\mathbf{r}} = -\gamma\dot{\mathbf{r}} + \boldsymbol{\mathcal{F}}(t). \tag{2.2}$$

Here we take a bird's eye view and split the influence of the surrounding fluid in two parts:

(i) A systematic frictional force $-\gamma\dot{\mathbf{r}}$ with friction coefficient γ.

(ii) A random force $\boldsymbol{\mathcal{F}}(t)$ at time t that arises due to multiple collisions between miniscule fluid particles (water molecule's size is $\sim 1\,\text{Å}$) and the larger colloid ($\sim 1\,\mu\text{m}$). Since the time between successive collisions between the fluid and the colloid is much smaller than the Brownian time scale, it is reasonable to assume that the temporal correlation of this force is infinitely small and its different Cartesian components are uncorrelated[2]. In other words, the dynamics is Markovian and has no memory. Force correlations are thus given by

$$\langle \mathcal{F}_i(t')\mathcal{F}_j(t'')\rangle = g\delta_{ij}\delta(t''-t'), \tag{2.3}$$

where $\langle\ldots\rangle$ denotes an ensemble average, δ_{ij} is the Kronecker delta, $\delta(t''-t')$ is the Dirac delta function and g is a measure of the strength of the fluctuating force. Since the Fourier transform of eq. (2.3) is independent of frequency, we refer to such a fluctuation as white noise. Moreover, since a large number of these collisions take place even in a very small time interval and there is no net drift of the colloid, thanks to the central limit theorem, it is justifiable to consider that the distribution of this force is a Gaussian centered at zero ($\langle\boldsymbol{\mathcal{F}}(t)\rangle = 0$) for all t [40].

Given an initial velocity $\mathbf{v}(0)$ at time $t = 0$, the velocity decays exponentially with time t

$$\langle\mathbf{v}(t)\rangle = \mathbf{v}(0)\mathrm{e}^{-t/\tau_{\text{v}}} \tag{2.4}$$

[2] If the colloid is not much larger than the particles it interacts with, the frictional force should take retardation effects into account and can be written as $-\int_0^t \mathrm{d}t'\,\gamma(t-t')u(t')$. In this case, we must additionally do away with the model of a delta-correlated force since time-scale separation cannot be presumed [40].

with viscous relaxation time $\tau_{\mathrm{v}} = m/\gamma$. The velocity autocorrelation for $t_{1,2} \gg \tau_{\mathrm{v}}$ is [41]

$$\langle v_i(t_1) v_j(t_2) \rangle \approx \frac{g}{2\gamma m} \delta_{ij} \mathrm{e}^{-|t_1 - t_2|/\tau_{\mathrm{v}}}. \tag{2.5}$$

This shows that the velocity autocorrelation also decays exponentially with time scale τ_{v}. For a d-dimensional system, in the limit $|t_1 - t_2| \to \infty$, the system must relax to equilibrium. As dictated by the equipartition theorem, the mean-square velocity in equilibrium

$$\left\langle \mathbf{v}^2 \right\rangle_{\mathrm{eq}} = \frac{d k_{\mathrm{B}} T}{m}. \tag{2.6}$$

with Boltzmann's constant k_{B}. Comparing with eq. (2.5), we get

$$g = 2\gamma k_{\mathrm{B}} T, \tag{2.7}$$

a popular fluctuation-dissipation theorem called the Einstein relation which relates the strength of fluctuations that arise because the fluid is at a finite temperature to the drag experienced by the colloid by virtue of being surrounded by the thermalized fluid.

Using eq. (2.5), the mean-square displacement computed after the particle has reached equilibrium is given by [42]

$$\left\langle [\mathbf{r}(t) - \mathbf{r}(0)]^2 \right\rangle = \int_0^t \mathrm{d}t_1 \int_0^t \mathrm{d}t_2 \ \langle v_i(t_1) v_j(t_2) \rangle \tag{2.8}$$

$$= \frac{2 d k_{\mathrm{B}} T m}{\gamma^2} \left(\frac{\gamma}{m} t - 1 + \mathrm{e}^{-\frac{\gamma}{m} t} \right) \tag{2.9}$$

$$= \begin{cases} \left\langle \mathbf{v}^2 \right\rangle_{\mathrm{eq}} t^2 & \text{for } t \ll \tau_{\mathrm{v}}, \\ \frac{2 d k_{\mathrm{B}} T}{\gamma} t & \text{for } t \gg \tau_{\mathrm{v}}. \end{cases} \tag{2.10}$$

This indicates that the colloid moves ballistically ($\propto t^2$) at short times because the 'kick' it received is effective and yet to be erased by subsequent random collisions. At long times, the colloid moves diffusively ($\propto t$). In this limit, we can define a *passive* diffusion coefficient D_0 through

$$\left\langle [\mathbf{r}(t) - \mathbf{r}(0)]^2 \right\rangle = \frac{2 d k_{\mathrm{B}} T}{\gamma} t \equiv 2 d D_0 t \tag{2.11}$$

with $D_0 = k_{\mathrm{B}} T / \gamma$ [39].

In addition to random forces, the fluid also imparts fluctuating torques and rotational friction on the colloid. Since we work in two dimensions throughout the thesis, there

is only one angular degree of freedom and rotation is confined to the xy plane, say. Let $\varphi(t)$ be the angle subscribed by the orientation of the colloid with the positive x axis at time t. The corresponding Langevin equation is

$$I\ddot{\varphi} = -\gamma_{\mathrm{r}}\dot{\varphi} + \mathcal{T}(t) \tag{2.12}$$

where I is the moment of inertia, γ_{r} is the rotational friction coefficient and $\mathcal{T}(t)$ is a random torque at time t. Following a similar line of reasoning used for obtaining the passive translational diffusion coefficient, the passive rotational diffusion coefficient D_{r} can be read off the mean-square angular displacement in the long-time limit

$$\left\langle [\varphi(t) - \varphi(0)]^2 \right\rangle = 2D_{\mathrm{r}}t \quad \text{for } t \gg I/\gamma_{\mathrm{r}} \tag{2.13}$$

with $D_{\mathrm{r}} = k_{\mathrm{B}}T/\gamma_{\mathrm{r}}$.

In the case of a spherical colloid of diameter a, we know from Stokes' law that $\gamma = 3\pi\eta a$ and $\gamma_{\mathrm{r}} = \pi\eta a^3$. Therefore, the translational and rotational diffusion coefficients are related through

$$D_{\mathrm{r}} = \frac{3}{a^2}D_0. \tag{2.14}$$

2.1.2 Brownian dynamics: the overdamped limit

From eq. (2.10), we know that any massive particle undergoes ballistic motion at short time scales. In the case of colloids in a liquid or rarefied gas, high-precision experiments show that such a ballistic motion lasts for $\sim 0.1 - 100\,\mu\mathrm{s}$ [43, 44]. Since we are interested in the behavior of such systems at much larger time scales, for all practical purposes, we can assume that momentum relaxes instantaneously (see fig. 2.1) and work in the limit of $\tau_{\mathrm{v}} \to 0$.

Dividing eq. (2.2) by γ and setting $\tau_{\mathrm{v}} = 0$, we get the *overdamped* Langevin equation for the position

$$\dot{\mathbf{r}} = \sqrt{2D_0}\boldsymbol{\xi}(t) \tag{2.15}$$

with $\boldsymbol{\xi}(t) = \boldsymbol{\mathcal{F}}(t)/(\sqrt{2D_0}\gamma)$. Analogously, for time $t \gg I/\gamma_{\mathrm{r}}$, the orientation is governed by

$$\dot{\varphi} = \sqrt{2D_{\mathrm{r}}}\xi_{\mathrm{r}}(t) \tag{2.16}$$

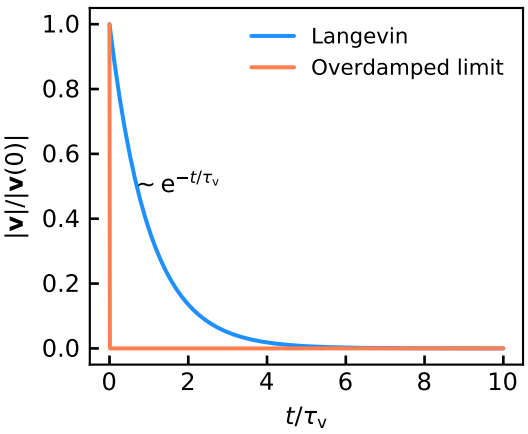

Figure 2.1: Relaxation of a particle governed by Langevin dynamics and overdamped Langevin dynamics. In the former case, an initial velocity $\mathbf{v}(0)$ relaxes exponentially as time progresses [see eq. (2.4)] and in the latter case, the velocity decays instantaneously.

where $\xi_{\mathrm{r}}(t) = \mathcal{T}(t)/(\sqrt{2D_{\mathrm{r}}}\gamma_{\mathrm{r}})$. The mean-square displacement and the mean-square angular displacement are

$$\left\langle [\mathbf{r}(t) - \mathbf{r}(0)]^2 \right\rangle = 2dD_0 t, \qquad \left\langle [\varphi(t) - \varphi(0)]^2 \right\rangle = 2D_{\mathrm{r}} t. \tag{2.17}$$

Since we neglected the inertial term in the Langevin equation, the initial ballistic regime is absent and the dynamics is purely diffusive for all times in the overdamped limit.

2.2 Active Brownian particles

Active (or self-propelled) particles are fundamentally different from their passive counterparts (discussed in section 2.1) due to the fact that they consume energy from a (replenishable) source and use this to propel directionally. As we will discuss in section 2.3, by and large, active particles realized in experiments move through a solvent phoretically. When any of these particles move, they disturb the surrounding solvent which in turn affects the motion of other particles. These many-body, long-ranged hydrodynamic interactions mediated by the flow of the solvent alters the particles' dynamics [45, 46]. A thorough description of the system would thus need to account for hydrodynamic, phoretic, steric and, in general, Coloumb interactions. Though desirable, such a description is often overwhelmingly complex and computationally expensive. However, depending on the question we ask, certain simplifications can be made. For example, phoretic interactions [47, 48, 49] are shown to play important roles in the description of Au-Pt Janus particles fuelled by

hydrogen peroxide. Hydrodynamic interactions, for instance, are key to describe motion of microorganisms through body deformations [46]. On the other hand, steric interactions alone are sufficient to describe features like dynamical clustering of carbon-coated Janus particles that propel via local demixing of the solvent [50].

In this section, we introduce the active Brownian particle (ABP) model, a widely used description of an active particle. It is obtained by extending the equations of motion employed for describing passive Brownian particles. After studying the dynamics of an isolated ABP, we move on to review the behavior of multiple ABPs that interact sterically with each other. This computationally economical model considers the following salient features: (1) self-propulsion, (2) excluded-volume interactions and (3) coupling to a heat bath maintained at a fixed temperature. With an aim to capture qualitative features seen in experiments with a model that is as simple as possible, we neglect all other interactions.

2.2.1 Dynamics of a single active Brownian particle

To include directed motion we modify eq. (2.15) as

$$\dot{\mathbf{r}} = v_0\mathbf{e} + \sqrt{2D_0}\boldsymbol{\xi}(t) \tag{2.18}$$

where v_0 is the propulsion speed and $\mathbf{e} \equiv (\cos\varphi, \sin\varphi)^T$. The first term is the self-propulsion term which is responsible for the persistent motion of the ABP along its orientation $\mathbf{e}$. As before, $\boldsymbol{\xi}(t)$ is Gaussian white noise with $\langle \xi_i(t) \rangle = 0$ and $\langle \xi_i(t)\xi_j(t') \rangle = \delta_{ij}\delta(t-t')$. Figure 2.2 (a) shows representative trajectories of ABPs for different propulsion speeds.

In general, we could additionally impart a persistent rotation[3] by adding an angular speed ω_0. This would lead to the particle spinning if $v_0 = 0$ and if not, to the circular motion of the particle [53]. However, we will restrict ourselves to purely diffusive rotation given by eq. (2.16).

The dimensionless Peclét number given by [54]

$$\mathrm{Pe} \equiv \frac{3v_0}{aD_\mathrm{r}} = \frac{3\ell_\mathrm{p}}{a} \tag{2.19}$$

[3] Such persistence in rotation and translation could, for example, arise due to anisotropic propulsion of the particle [51] or anisotropy in shape [52].

quantifies the relative weight of propulsive and diffusive motion. The limits Pe=0 and Pe=∞ respectively correspond to the purely Brownian and purely ballistic motion of the particle. Here we have introduced the persistence length $\ell_\mathrm{p} \equiv v_0/D_\mathrm{r}$. For passive particles ($v_0 = 0$), as expected, $\ell_\mathrm{p} = 0$.

The average distance travelled in time t is

$$\langle |\mathbf{r}(t) - \mathbf{r}(0)| \rangle = \ell_\mathrm{p} \left(1 - \mathrm{e}^{-D_\mathrm{r} t}\right). \tag{2.20}$$

The mean-square displacement is given by [25]

$$\left\langle [\mathbf{r}(t) - \mathbf{r}(0)]^2 \right\rangle = 4D_0 t + 2\frac{v_0^2}{D_\mathrm{r}^2}\left(D_\mathrm{r} t - 1 + \mathrm{e}^{-D_\mathrm{r} t}\right). \tag{2.21}$$

Integrating eqs. (2.18, 2.16) numerically[4], we find that the mean-square displacement perfectly agrees with the theoretical result (see fig. 2.2). Taking the short and long-time limits, we get

$$\left\langle [\mathbf{r}(t) - \mathbf{r}(0)]^2 \right\rangle = \begin{cases} 4D_0 t + v_0^2 t^2 & \text{for } D_\mathrm{r} t \ll 1, \\ 4\left(D_0 + \frac{v_0^2}{2D_\mathrm{r}}\right) t & \text{for } D_\mathrm{r} t \gg 1. \end{cases} \tag{2.22}$$

On comparing with eq. (2.15), we realize that in the long-time limit, the dynamics of an active particle is similar to that of a passive particle with an enhanced diffusion given by coefficient $D_0 + v_0^2/(2D_\mathrm{r})$. This is why active matter is sometimes referred to as 'hot' matter.

Since the orientation φ performs free diffusion, the mean angular displacement is zero and the mean-square angular displacement is given by eq. (2.17).

2.2.2 System of interacting active Brownian particles

Let us now consider a system of N active Brownian particles that interact with each other such that they mutually exclude volume (*i.e.*, no overlaps). We will consider this interaction to be short-ranged and repulsive. Extending eq. (2.18), we can write the equations of motion that govern the position $\mathbf{r}_i$ and orientation φ_i of the ith particle as

$$\dot{\mathbf{r}}_i = v_0 \mathbf{e}_i - \mu_0 \nabla_i U + \sqrt{2D_0}\boldsymbol{\xi}_i, \qquad \dot{\varphi}_i = \sqrt{2D_\mathrm{r}}\xi_i. \tag{2.23}$$

[4]See section 2.2.3 on numerical methods for details on how these simulations are performed.

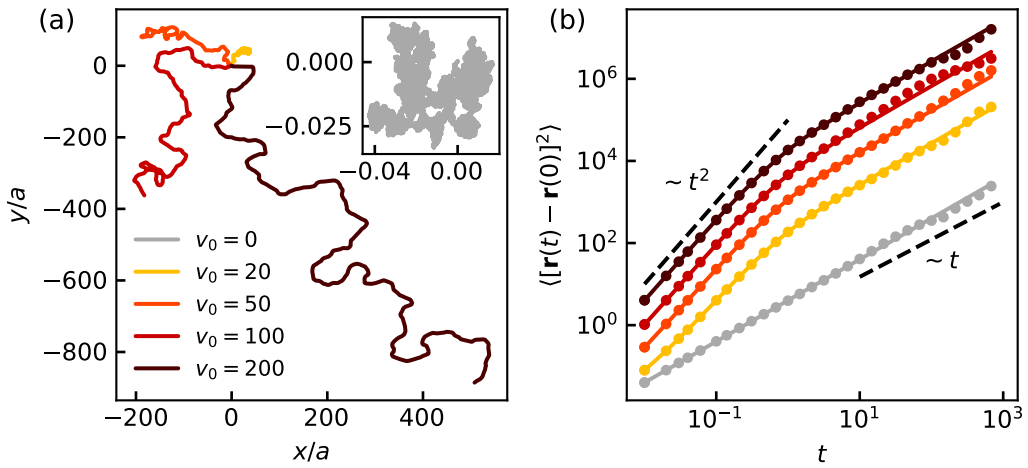

Figure 2.2.: (a) Trajectories of active Brownian particles in two dimensions for different propulsion speeds v_0. In all cases, the equations of motion [eqs. (2.18, 2.16)] have been integrated for the same total time. The trajectory in grey (inset) corresponds to the passive case. As v_0 increases, since the persistence length ℓ_p correspondingly increases, the particle covers a larger distance. (b) Mean-square displacement (MSD) for different v_0. At small times, the particle exhibits ballistic motion (MSD $\propto t^2$) whereas at large times, the dynamics is diffusive (MSD $\propto t$). The markers represent data from simulations and the solid lines correspond to eq. (2.21).

Here $\mu_0 = D_0/(k_\mathrm{B}T)$ is the (passive) translational mobility, ∇ is the Del operator in two dimensions[5] and U is the total potential energy due to interactions.

Smoluchowski equation

As an alternative to describing the evolution of the degrees of freedom of individual particles, we can represent the dynamics of the system in terms of the evolution of a probability density. We now outline how a switch to the latter description can be done.

In general, the Langevin equation corresponding to an $\mathcal{N}$-component process $\boldsymbol{\mathcal{C}} = (\mathcal{C}_1, \ldots, \mathcal{C}_\mathcal{N})^T$ is a stochastic differential equation of the form [41]

$$\frac{\mathrm{d}\mathcal{C}_i}{\mathrm{d}t} = h_i(\boldsymbol{\mathcal{C}}, t) + g_{ik}(\boldsymbol{\mathcal{C}}, t)\xi_k(t) \tag{2.24}$$

[5] In Cartesian coordinates, $\nabla \equiv \left(\frac{\partial}{\partial x}, \frac{\partial}{\partial y}\right)$.

where h_i and $g_{ik}\xi_k$ are the drift and diffusion terms respectively, and ξ_k is Gaussian white noise. We have used the Einstein convention of summing over repeated indices. On rewriting eq. (2.24) as an integral equation, we get

$$\boldsymbol{\mathcal{C}}(t+\Delta t) = \boldsymbol{\mathcal{C}} + \int_t^{t+\Delta t} \mathrm{d}t'\; h_i(\boldsymbol{\mathcal{C}}(t'),t') + \int_t^{t+\Delta t} \mathrm{d}t'\; g_{ik}(\boldsymbol{\mathcal{C}}(t'),t')\xi_k(t') \tag{2.25}$$

where $\boldsymbol{\mathcal{C}} \equiv \boldsymbol{\mathcal{C}}(t)$. On Taylor expanding $h_i(\boldsymbol{\mathcal{C}}(t'),t')$, we get

$$h_i(\boldsymbol{\mathcal{C}}(t'),t') = h_i(\boldsymbol{\mathcal{C}},t') + \mathcal{J}_{ij}[\boldsymbol{\mathcal{C}}(t') - \boldsymbol{\mathcal{C}}]_j + \ldots. \tag{2.26}$$

where $\mathcal{J}_{ij} = \partial h_i/\partial \mathcal{C}_j$ is the Jacobian matrix evaluated at $\boldsymbol{\mathcal{C}}$. We analogously expand g_{ik}. Plugging the expansions and $\boldsymbol{\mathcal{C}}(t+\Delta t) - \boldsymbol{\mathcal{C}}$ obtained by rearranging eq. (2.25) into eq. (2.25), we obtain

$$\begin{aligned}\boldsymbol{\mathcal{C}}(t+\Delta t) = \boldsymbol{\mathcal{C}} &+ \int_t^{t+\Delta t} \mathrm{d}t'\; h_i(\boldsymbol{\mathcal{C}},t') + \int_t^{t+\Delta t} \mathrm{d}t'\; \mathcal{J}_{ij} \int_t^{t'} \mathrm{d}t''\; h_j(\boldsymbol{\mathcal{C}},t'') \\ &+ \int_t^{t+\Delta t} \mathrm{d}t'\; \mathcal{J}_{ij} \int_t^{t'} \mathrm{d}t''\; g_{jk}(\boldsymbol{\mathcal{C}},t'')\xi_k(t'') + \int_t^{t+\Delta t} \mathrm{d}t'\; g_{ik}(\boldsymbol{\mathcal{C}},t')\xi_k(t') \\ &+ \int_t^{t+\Delta t} \mathrm{d}t'\; \tilde{\mathcal{J}}_{ijk}\xi_k(t') \int_t^{t'} \mathrm{d}t''\; h_j(\boldsymbol{\mathcal{C}},t'') + \int_t^{t+\Delta t} \mathrm{d}t'\; \tilde{\mathcal{J}}_{ijk}\xi_k(t') \int_t^{t'} \mathrm{d}t''\; g_{jl}(\boldsymbol{\mathcal{C}},t'')\xi_l(t'').\end{aligned} \tag{2.27}$$

Here $\tilde{\mathcal{J}}_{ijk} = \partial g_{ik}/\partial \mathcal{C}_j$ evaluated at $\boldsymbol{\mathcal{C}}$. On taking the mean, we get

$$\begin{aligned}\langle \boldsymbol{\mathcal{C}}(t+\Delta t) - \boldsymbol{\mathcal{C}} \rangle = &\int_t^{t+\Delta t} \mathrm{d}t'\; h_i(\boldsymbol{\mathcal{C}},t') + \int_t^{t+\Delta t} \mathrm{d}t'\; \mathcal{J}_{ij} \int_t^{t'} \mathrm{d}t''\; h_j(\boldsymbol{\mathcal{C}},t'') \\ &+ 2D \int_t^{t+\Delta t} \mathrm{d}t'\; \tilde{\mathcal{J}}_{ijk} \int_t^{t'} \mathrm{d}t''\; g_{jk}(\boldsymbol{\mathcal{C}},t'')\delta(t''-t')\end{aligned} \tag{2.28}$$

where we have used the properties: $\langle \xi_k(t) \rangle = 0$ and $\langle \xi_k(t)\xi_l(t') \rangle = \delta_{kl}\delta(t-t')$. The second term evaluates to zero. Using the identity $\int_a^b \mathrm{d}x\; \delta(x-a)f(x) = \frac{1}{2}f(a)$, we get

$$\mathbf{c}_1 \equiv \lim_{\Delta t \to 0} \frac{\langle \boldsymbol{\mathcal{C}}(t+\Delta t) - \boldsymbol{\mathcal{C}} \rangle}{\Delta t} = h_i(\boldsymbol{\mathcal{C}},t) + \frac{1}{2}\tilde{\mathcal{J}}_{ijk}g_{jk}(\boldsymbol{\mathcal{C}},t). \tag{2.29}$$

Along similar lines, we get

$$\mathbf{c}_2 \equiv \lim_{\Delta t \to 0} \frac{\langle [\boldsymbol{\mathcal{C}}(t+\Delta t) - \boldsymbol{\mathcal{C}}]^2 \rangle}{\Delta t} \tag{2.30}$$

$$= \lim_{\Delta t \to 0} \frac{1}{\Delta t} \int_t^{t+\Delta t} \mathrm{d}t'\; g_{ik}(\boldsymbol{\mathcal{C}},t') \int_t^{t'} \mathrm{d}t''\; g_{jk}(\boldsymbol{\mathcal{C}},t'')\delta(t'-t'') \tag{2.31}$$

$$= g_{ik}(\boldsymbol{\mathcal{C}},t)g_{jk}(\boldsymbol{\mathcal{C}},t). \tag{2.32}$$

The quantities $\mathbf{c}_1$ and $\mathbf{c}_2$ are the Kramers-Moyal coefficients that enter the (multivariate) Fokker-Planck equation

$$\partial_t \psi = -\frac{\partial}{\partial \mathcal{C}_i}\left\{\left[h_i(\boldsymbol{\mathcal{C}},t) + g_{jk}(\boldsymbol{\mathcal{C}},t)\frac{\partial g_{ik}(\boldsymbol{\mathcal{C}},t)}{\partial \mathcal{C}_j}\right]\psi\right\} + \frac{1}{2}\frac{\partial^2}{\partial \mathcal{C}_i \partial \mathcal{C}_j}[g_{ik}(\boldsymbol{\mathcal{C}},t)g_{jk}(\boldsymbol{\mathcal{C}},t)]\psi \tag{2.33}$$

where ψ is the probability density. For active Brownian particles described by eqs. (2.23), $\boldsymbol{\mathcal{C}}$ is a $3N$-dimensional vector comprising of the positions and orientations of all N particles. The second term in the curly brackets vanishes. The drift coefficients are

$$h_i = \begin{cases} v_0 \cos\varphi_i - \mu_0 \nabla_i U, & \forall i \in \{x_i\} \\ v_0 \sin\varphi_i - \mu_0 \nabla_i U, & \forall i \in \{y_i\} \\ 0, & \forall i \in \{\varphi_i\} \end{cases} \tag{2.34}$$

and the diffusion coefficients are

$$g_{ik}g_{jk} = \begin{cases} D_0, & \forall i \in \{\{x_i\},\{y_i\}\} \\ D_\mathrm{r}, & \forall i \in \{\varphi_i\} \end{cases} \tag{2.35}$$

On plugging eqs. [(2.34),(2.35)] in eq. (2.33), we find that the Smoluchowski equation[6] that describes the evolution of the N-particle probability distribution $\psi_N = \psi_N(\{\mathbf{r}_i\},\{\varphi_i\};t)$ is

$$\partial_t \psi_N = \sum_{i=1}^{N}\left\{-\nabla_i \cdot \left[\left(v_0 \mathbf{e}_i - \mu_0 \nabla_i U\right)\psi_N\right] + D_0 \nabla_i^2 \psi_N + D_\mathrm{r}\partial_{\varphi_i}^2 \psi_N\right\}. \tag{2.36}$$

One-body Smoluchowski equation

In general, the n-particle joint probablity distribution $\psi_n(\{\mathbf{r}_1,\ldots,\mathbf{r}_n\},\{\varphi_1,\ldots,\varphi_n\};t)$ that describes finding n particles at positions $\{\mathbf{r}_1,\ldots,\mathbf{r}_n\}$ with orientations $\{\varphi_1,\ldots,\varphi_n\}$ at time t is given by

$$\psi_n = \frac{N!}{(N-n)!}\int \mathrm{d}\mathbf{r}_{n+1}\ldots\mathrm{d}\mathbf{r}_N \int \mathrm{d}\varphi_{n+1}\ldots\mathrm{d}\varphi_N\, \psi_N. \tag{2.37}$$

Here, the spatial integrals are performed between the limits $-\infty$ and ∞, and the angular integrals are performed between the limits 0 and 2π. The combinatorial factor $N!/(N-n)!$ is included to account for the number of ways in which n particles

[6] The Fokker-Planck equation in the overdamped limit is called Smoluchowski equation.

can be chosen from N indistinguishable particles. Setting $n = 1$, we get the one-body probability density $\psi_1 = N \int \mathrm{d}\mathbf{r}_2 \ldots \mathrm{d}\mathbf{r}_N \int \mathrm{d}\varphi_2 \ldots \mathrm{d}\varphi_N \, \psi_N$. Henceforth we will drop the subscript and, for convenience, rename $\psi_1 \to \psi, \mathbf{r}_1 \to \mathbf{r}$ and $\varphi_1 \to \varphi$. On performing the integral to obtain an evolution equation for ψ, the drift term becomes

$$
\begin{aligned}
&- N \sum_{i=1}^{N} \left\{ \int \mathrm{d}\mathbf{r}_2 \ldots \mathrm{d}\mathbf{r}_N \int \mathrm{d}\varphi_2 \ldots \mathrm{d}\varphi_N \, \left[\nabla_i \cdot (v_0 \mathbf{e}_i \psi_N) - \mu_0 (\nabla_i U) \psi_N \right] \right\} \\
&= -\nabla \cdot (v_0 \mathbf{e} \psi) - \mu_0 \nabla \cdot \int \mathrm{d}\mathbf{r}_2 \ldots \mathrm{d}\mathbf{r}_N \int \mathrm{d}\varphi_2 \ldots \mathrm{d}\varphi_N \, N \sum_{i=2}^{N} \left[-\nabla U \right] \psi_N \\
&- \sum_{i=2}^{N} \int \mathrm{d}\mathbf{r}_2 \ldots \mathrm{d}\mathbf{r}_{i-1} \mathrm{d}\mathbf{r}_{i+1} \ldots \mathrm{d}\mathbf{r}_N \int \mathrm{d}\varphi_2 \ldots \mathrm{d}\varphi_N N \underbrace{\int \mathrm{d}\mathbf{n}_i \cdot (\mathbf{e}_i \psi_N)}_{=0} \\
&+ \mu_0 \sum_{i=2}^{N} \int \mathrm{d}\mathbf{r}_2 \ldots \mathrm{d}\mathbf{r}_{i-1} \mathrm{d}\mathbf{r}_{i+1} \ldots \mathrm{d}\mathbf{r}_N \int \mathrm{d}\varphi_2 \ldots \mathrm{d}\varphi_N \, N \underbrace{\int \mathrm{d}\mathbf{n}_i \cdot (\mathbf{e}_i \psi_N)}_{=0} .
\end{aligned}
\tag{2.38}
$$

We have used the divergence theorem (with normal vector $\mathbf{n}_i$) in the second step. Also, we demand that ψ_N as $|\mathbf{r}_i| \to \pm\infty$ is zero. By using the fact that the particles are identical, the sum becomes a sum over identical terms. The expression subsequently simplifies to

$$
\begin{aligned}
&- \nabla \cdot (v_0 \mathbf{e} \psi) - \mu_0 N (N-1) \nabla \cdot \int \mathrm{d}\mathbf{r}_2 \mathrm{d}\mathbf{r}_3 \ldots \mathrm{d}\mathbf{r}_N \int \mathrm{d}\varphi_2 \mathrm{d}\varphi_3 \ldots \mathrm{d}\varphi_N \left[-\nabla U \right] \psi_N \\
&= -\nabla \cdot (v_0 \mathbf{e} \psi) - \mu_0 \nabla \cdot \int \mathrm{d}\mathbf{r}' \int \mathrm{d}\varphi' \left[-\nabla U \right] \psi_2(\mathbf{r}, \mathbf{r}', \varphi, \varphi'; t)
\end{aligned}
\tag{2.39}
$$

Here we have plugged in the definition given in eq. (2.37) for the case $n = 2$. We have also renamed the variables $\mathbf{r}_2 \to \mathbf{r}'$ and $\varphi_2 \to \varphi'$. The diffusion term is given by

$$
\begin{aligned}
&N \int \mathrm{d}\mathbf{r}_2 \ldots \mathrm{d}\mathbf{r}_N \int \mathrm{d}\varphi_2 \ldots \mathrm{d}\varphi_N \left\{ D_0 \sum_{i=1}^{N} \nabla_i^2 \psi_N + D_\mathrm{r} \sum_{i=1}^{N} \partial_{\varphi_i}^2 \psi_N \right\} \\
&= D_0 \nabla^2 \psi + D_\mathrm{r} \partial_\varphi^2 \psi \\
&+ D_0 \sum_{i=2}^{N} \int \mathrm{d}\mathbf{r}_2 \ldots \mathrm{d}\mathbf{r}_{i-1} \mathrm{d}\mathbf{r}_{i+1} \ldots \mathrm{d}\mathbf{r}_N \int \mathrm{d}\varphi_2 \ldots \mathrm{d}\varphi_N \, N \underbrace{\int \mathrm{d}\mathbf{n}_i \cdot (\nabla_i \psi_N)}_{=0} \\
&+ D_\mathrm{r} \sum_{i=2}^{N} \int \mathrm{d}\mathbf{r}_2 \ldots \mathrm{d}\mathbf{r}_N \int \mathrm{d}\varphi_2 \ldots \mathrm{d}\varphi_{i-1} \mathrm{d}\varphi_{i+1} \ldots \mathrm{d}\varphi_N \, N \underbrace{\left[\partial_{\varphi_i} \psi_N \right]_{\varphi_i = 0}^{\varphi_i = 2\pi}}_{=0}
\end{aligned}
\tag{2.40}
$$

where we have used the divergence theorem is the second step and set $\nabla_i \psi_N = 0$ as $|\mathbf{r}_i| \to \pm\infty$. Moreover, since ψ_N and its angular derivatives are 2π-periodic, the last term vanishes.

Gathering all terms, we get

$$\partial_t \psi = -\nabla \cdot [v_0 \mathbf{e}\psi + \mu_0 \mathbf{f} - D_0 \nabla \psi] + D_\mathrm{r} \partial_\varphi^2 \psi \tag{2.41}$$

with mean force density $\mathbf{f}$ defined as

$$\mathbf{f} \equiv -\int \mathrm{d}\mathbf{r}' \int \mathrm{d}\varphi' [\nabla U] \psi_2(\mathbf{r}, \mathbf{r}', \varphi, \varphi'; t) = -\int \mathrm{d}\mathbf{r}' [\nabla U] \bar{\psi}_2(\mathbf{r}, \mathbf{r}', \varphi; t). \tag{2.42}$$

where $\bar{\psi}_2 = \int \mathrm{d}\varphi' \psi_2$. Note that we have assumed the potential U to be independent of the particles' orientations in the last step. As we will discuss in chapter 3, this does not hold true for elongated particles.

Orientational moments

To gain further insight into eq. (2.41), it is useful to expand ψ (a 2π-symmetric function) into its angular Fourier modes as [55]

$$\psi(\mathbf{r}, \varphi; t) = \frac{1}{2\pi} \sum_{k=-\infty}^{\infty} \hat{\psi}_k(\mathbf{r}, t) \mathrm{e}^{-ik\varphi}, \quad \hat{\psi}_k(\mathbf{r}, t) = \int_{-\pi}^{\pi} \mathrm{d}\varphi \; \psi(\mathbf{r}, \varphi; t) \mathrm{e}^{ik\varphi} \tag{2.43}$$

where $\hat{\psi}_k$ are Fourier coefficients. We identify the following order parameter fields:

$$\rho(\mathbf{r}, t) \equiv \hat{f}_0 = \int_{-\pi}^{\pi} \mathrm{d}\varphi \; \psi \tag{2.44}$$

$$\mathbf{p}(\mathbf{r}, t) \equiv \begin{pmatrix} \mathrm{Re}\hat{f}_1 \\ \mathrm{Im}\hat{f}_1 \end{pmatrix} = \int_{-\pi}^{\pi} \mathrm{d}\varphi \; \mathbf{e}\psi \tag{2.45}$$

$$\mathbf{Q}(\mathbf{r}, t) \equiv \frac{1}{2} \begin{pmatrix} \mathrm{Re}\hat{f}_2 & \mathrm{Im}\hat{f}_2 \\ \mathrm{Im}\hat{f}_2 & -\mathrm{Re}\hat{f}_2 \end{pmatrix} = \int_{-\pi}^{\pi} \mathrm{d}\varphi \; \left(\mathbf{e}\mathbf{e}^T - \frac{1}{2}\mathbf{1} \right) \psi \tag{2.46}$$

where $\mathbf{1}$ is the 2×2 identity matrix, ρ is the density, $\mathbf{p}$ is the polarization density and $\mathbf{Q}$ is the symmetric and traceless nematic tensor. We can readily obtain the equations governing the dynamics of these quantities by using eq. (2.41) and performing the corresponding integrals.

Closure and mean-field theory

Since the force density [see eq. (2.42)] involves ψ_2, the evolution of which depends on ψ_3 and so on, we obtain a system of coupled equations akin to the Bogoliubov-Born-Green-Kirkwood-Yvon (BBGKY) hierarchy [56]. To progress further, we must truncate this hierarchy. A way to perform this truncation was proposed by Bialké *et al* [35]. We will now outline the procedure used therein.

First, we rewrite the expression for $\bar{\psi}_2$ as a function of the one-body density through

$$\bar{\psi}_2 = \psi_1(\mathbf{r}, \varphi; t)\rho g(\mathbf{r}, \mathbf{r}', \varphi; t) \tag{2.47}$$

where $g(\mathbf{r}, \mathbf{r}', \varphi; t)$ is the pair correlation function[7].

We now change the reference frame such that it is centered at $\mathbf{r}$, the position of an (arbitrary) tagged particle. An other (arbitrary) particle is located at $\mathbf{r}'$ and in the frame of the tagged particle, at $\mathbf{r}' - \mathbf{r}$. The angle enclosed by $\mathbf{r}' - \mathbf{r}$ and $\mathbf{e}$ is θ. Assuming that the pair correlation is time-independent and translationally invariant, the force can be approximated as

$$\mathbf{F}(\mathbf{r}, \varphi; t) \approx \rho(\mathbf{r}, t) \int_0^\infty \mathrm{d}r \int_0^{2\pi} \mathrm{d}\theta \; r[-\nabla u(r)]g(r, \theta). \tag{2.48}$$

Decomposing the force as a projection onto the orientation $\mathbf{e}$ and a remainder $\delta\mathbf{F}$, we get

$$\mathbf{F} = (\mathbf{e}\cdot\mathbf{F})\mathbf{e} + \delta\mathbf{F} \approx (\mathbf{e}\cdot\mathbf{F})\mathbf{e} = -\rho\zeta\psi \tag{2.49}$$

with force-imbalance coefficient [35]

$$\zeta \equiv \int_0^\infty \mathrm{d}r \; [-\nabla u(r)] \int_0^{2\pi} \mathrm{d}\theta \; \cos\theta g(r, \theta). \tag{2.50}$$

The effect of including of $\delta\mathbf{F}$ can be captured by introducing a modified diffusion coefficient [57]. Due to the anisotropy of $g(r, \theta)$ for active particles [35], $\zeta > 0$. For passive particles, $g(r, \theta) = g(r)$ is isotropic and $\zeta = 0$. Substituting eq. (2.49) in eq. (2.41), we get a closed equation given by

$$\partial_t\psi = -\nabla\cdot\left[v(\rho)\mathbf{e}\psi - D_0\nabla\psi\right] + D_\mathrm{r}\partial_\varphi^2\psi \tag{2.51}$$

[7] Here we assume that the density is homogeneous on length-scales at which the potential is non-zero [57].

with density-dependent speed

$$v(\rho) = v_0 - \mu_0 \rho \zeta. \tag{2.52}$$

For repulsive interactions described by the WCA potential, $v(\rho)$ decreases linearly with density ρ [35]. For softer potentials however, this relation does not necessarily hold [58].

2.2.3 Numerical methods

To understand the dynamical behavior of several interacting particles, one often has to resort to performing computer simulations as an analytical solution is elusive. Moreover, simulations serve as a wind tunnel for analytically tractable systems. As a first step toward performing simulations, we discretize and propagate the governing equations of motion [eq. (2.23)] through the Euler-Maruyama scheme [59] given by

$$\begin{aligned} \mathbf{r}_i(t + \Delta t) &= \mathbf{r}_i(t) + [v_0 \mathbf{e}_i(t) - \mu_0 \nabla_i U(t)]\Delta t + \sqrt{2D_0 \Delta t}\boldsymbol{\Xi}_i(t), \\ \varphi_i(t + \Delta t) &= \varphi_i(t) + \sqrt{2D_\mathrm{r} \Delta t}\Xi_{\mathrm{r},i}(t) \end{aligned} \tag{2.53}$$

where Δt is the time step and $t \geq 0$. The components of $\boldsymbol{\Xi}_i$ and $\Xi_{\mathrm{r},i}$ are drawn from a unit normal distribution at every time step. Alternatively, a uniform distribution centered at zero with unit variance may also be used [60] to improve efficiency. Note that the initial conditions $\{\mathbf{r}_i(t = 0)\}$ and $\{\varphi_i(t = 0)\}$ must be provided.

The total potential energy U is determined by the interactions we choose to consider in the model. We consider repulsive, short-ranged excluded volume interactions modelled using the purely repulsive Weeks-Chandler-Andersen (WCA) pair potential [61], a truncated and shifted variant of the Lennard-Jones (LJ) pair potential [62], given by

$$u_{ij}(r_{ij}) = 4\varepsilon \left[\left(\frac{\sigma}{r_{ij}} \right)^{12} - \left(\frac{\sigma}{r_{ij}} \right)^{6} + \frac{1}{4} \right] \Theta\left(2^{1/6}\sigma - r_{ij} \right), \tag{2.54}$$

where $r_{ij} = |\mathbf{r}_{ij}|$ is the distance between the ith and jth particles, σ is the length scale of the potential (typically taken to be the diameter of the particle), ε is the depth of the energy well and $\Theta(\cdot)$ is the Heaviside step function.

The LJ potential only depends on the distance r_{ij} between the two interacting particles. It is thus be used to emulate spherical (discoidal in two dimensions) particles. To model aspherical particles, several LJ sites may be used [63, 64]. Here, we employ the Gay-Berne pair (GB) potential [65], a modified version of the LJ potential that takes anisotropy into consideration, given by

$$u_{\mathrm{GB}}(\mathbf{r}_{ij}, \mathbf{e}_i, \mathbf{e}_j) = 4\varepsilon\hat{\varepsilon}\left(\iota^{-12} - \iota^{-6}\right) \tag{2.55}$$

where $\iota \equiv r_{ij}/\sigma - \hat{\sigma} + 1$. The orientation-dependent well-depth and contact distance are $\hat{\varepsilon}(\hat{\mathbf{r}}_{ij}, \mathbf{e}_i, \mathbf{e}_j)$ and $\hat{\sigma}(\hat{\mathbf{r}}_{ij}, \mathbf{e}_i, \mathbf{e}_j)$ respectively. Furthermore, to make the potential purely repulsive, we cut it off at its minimum $r_{\mathrm{cut}} = \sigma[2^{1/6} - 1 + \hat{\sigma}]$ and shift it by $\varepsilon_{\mathrm{min}} = \varepsilon\hat{\varepsilon}(r_{\mathrm{cut}}\hat{\mathbf{r}}_{ij}, \mathbf{e}_i, \mathbf{e}_j)$ so that it smoothly approaches zero at the cut-off, *i.e.*,

$$u_{\mathrm{RGB}}(\mathbf{r}_{ij}, \mathbf{e}_i, \mathbf{e}_j) = (u_{\mathrm{GB}} + \varepsilon_{\mathrm{min}})\Theta(r_{\mathrm{cut}} - r_{ij}). \tag{2.56}$$

For isotropic particles, the GB potential reduces to the WCA potential thereby allowing the systematic study of the effect of particle shape from disks to elongated ellipses. For further details about the GB potential, see appendix A.1.

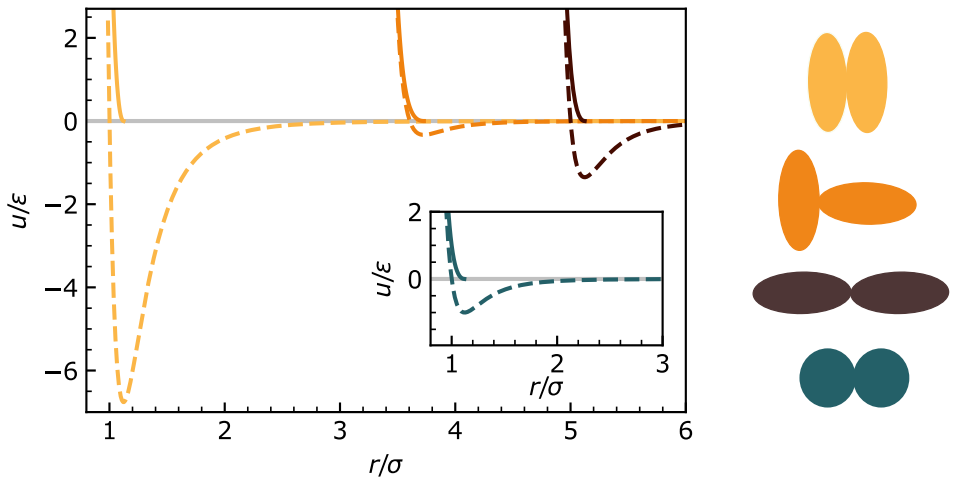

Figure 2.3.: The dashed lines represent the full Gay-Berne potential [eq. (2.55)] and the solid lines represent the repulsive Gay-Berne potential [eq. (2.56)]. In the inset, the Lennard-Jones potential (dashed line) and the Weeks-Chandler-Andersen potential (solid line) used for modelling spherical particles are plotted. The particle configurations that correspond to these potentials are shown on the right with the same color.

Given the pair potential u, the total potential energy $U = \sum_{i<j} u$ can be obtained by summing over all pairs of particles. Neighbor lists are often used to accelerate this calculation [62].

Computer simulations are necessarily performed in a finite domain. However the behavior of infinite systems is often of interest. In such cases, we use periodic boundary conditions to retain properties of the bulk and eliminate surface effects [66]. This is done by replicating the simulation domain (spanning between $-L_{x,y}/2$ and $L_{x,y}/2$ along the x, y-axis) along both coordinate axes [cf. fig. 2.4 (a)]. A particle with position $r_{i,k}$ leaving this domain is wrapped into it using

$$r_{i,k} = \begin{cases} r_{i,k} + L_k & \text{if } r_{i,k} < -L_k/2, \\ r_{i,k} - L_k & \text{if } r_{i,k} > L_k/2 \end{cases} \tag{2.57}$$

where $k = \{1, 2\}$ represents the x and y directions and L_k is the length of the simulation domain along the kth direction. Any particle property $\mathcal{Q}_i$ associated with the ith particle is thus periodic with periodicity L_k along the kth direction, *i.e.*, $\mathcal{Q}_i = \mathcal{Q}_i + L_k$. Quantities like pair potentials and forces that depend on the distance between two particles are calculated by employing the minimum image convention according to which a given particle interacts with the closest image of another particle.

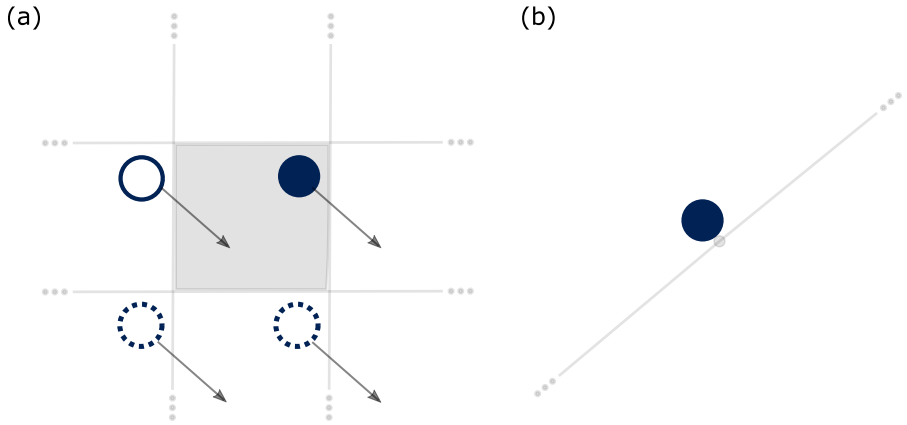

Figure 2.4.: (a) Periodic boundary conditions. The particle leaving the simulation domain (filled circle) re-enters from a replica (empty circle). Other images of the particle are depicted as dashed circles. (b) Interaction with a planar wall. The point on the wall closest to the particle (indicated by a grey dot) interacts repulsively with the particle (filled circle).

Presence of confinements can be handled by introducing an appropriate potential at the site of the confinement. For example, a planar, repulsive wall can be modelled through a WCA potential between a particle and the point on the wall nearest to the particle as depicted in fig. 2.4 (b).

2.2.4 Phase separation of active Brownian particles

Phases are states of matter which can be associated with characteristic (macroscopic) physical properties. Upon varying the *control parameter*, a system transitions from one phase to an other. Such changes are parametrized using one or more *order parameter(s)*. A prototypical example of a phase transition is ice melting to water and water vaporizing to steam upon increasing temperature. In this case, liquid and gaseous phases form as a result of a tug-of-war between entropy and energy whose relative importance is determined by the temperature. At low temperatures, entropy is outweighed by cohesive interactions between molecules, thereby favouring a liquid state. On increasing temperature, entropy begins to dominate, thus prompting the formation of a gaseous state.

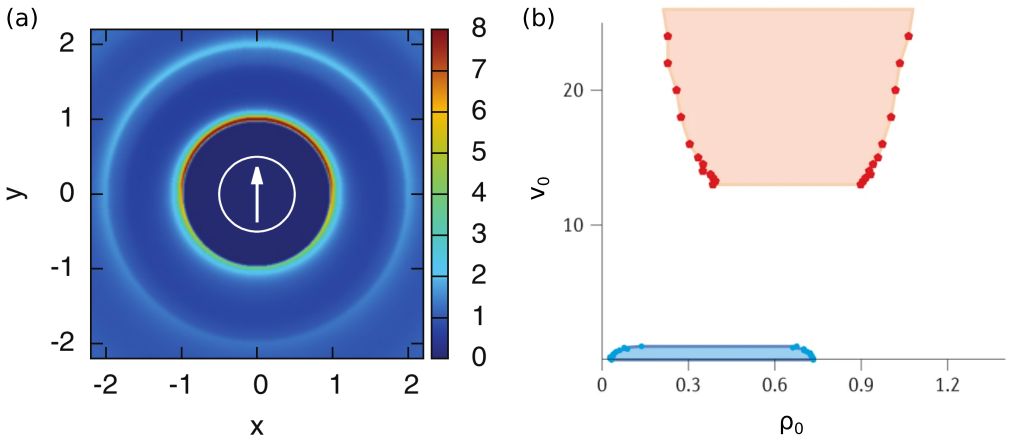

Figure 2.5.: (a) Pair distribution function $g(r, \theta)$ calculated in the reference frame of a tagged particle located at the origin and oriented along the y axis. The distribution shows that it is highly probable to find another particle at the front of the tagged particle. Reproduced from Ref. [35]. (b) Coexisting densities obtained from simulations of active particles interacting through the Lennard-Jones potential. The phase diagram shows a re-entrant behavior on increasing the propulsion speed v_0. Reproduced in adapted form from Ref. [67].

Let us now systematically increase the propulsion speed starting from the passive limit ($v_0 = 0$). As anticipated, for small v_0, the system is close to equilibrium and exhibits time-honoured liquid-gas phase separation. Beyond a threshold, the system becomes homogeneous. On increasing v_0 further, the system undergoes phase separation akin to that seen in equilibrium ($v_0 = 0$). The corresponding binodals are shown in fig. 2.5 (b). Interestingly, such a motility-induced phase separation (MIPS) occurs even in the absence of attractive inter-particle interactions at densities much smaller than closed packing. Since phase separation in passive

systems necessarily requires attractive interactions, MIPS is an inherently out-of-equilibrium phenomenon triggered by a positive-feedback mechanism: When two (or more) particles interact, they block each other and slow down, leading to the formation of small aggregates. If more particles join the cluster during the time it takes for particles at the boundary to reorient due to rotational diffusion and dissociate, the cluster grows in size making it further difficult for particles away from the boundary to leave. This dynamical instability leads to a steady state with coexisting dense and dilute regions.

In the mean-field description discussed in section 2.2.2, the effect of particles slowing down due to crowding is captured by the density-dependent speed $v(\rho)$ and the region of instability is determined by the force-imbalance coefficient ζ. Figure 2.5 shows the pair distribution function $g(r, \theta)$ that enters the definition of ζ [see eq. (2.50)]. The manifestly higher density in the direction of propulsion leads to slow down of the (arbitrarily chosen) tagged particle. MIPS occurs when ζ is large enough.

2.3 Active particles in experiments

Despite the vast number of studies performed with bacteria like *Bacillus subtilis* and *Escherichia coli* [68], animals like sheep [69, 70], fish [71] and birds [72], the ability to exercise control over the motion of living active matter is largely limited. This shortcoming has motivated the development of synthetic active particles. A common strategy is to use Janus particles which have surfaces made of two different materials with distinct physical properties. Usually, gradients in temperature (thermophoresis), electric potential (electrophoresis) or solute concentration (diffusiophoresis) results in the directed motion of these particles. An archetypal example is that of a Janus particle with gold and platinum parts immersed in a hydrogen peroxide solvent. The platinum side catalyses the decomposition of peroxide upon shining light whereas the gold side is chemically inert. The propulsion of the particle results from a combination of diffusiophoresis and electrophoresis [73, 48].

Self-propulsion of carbon-coated silica particles immersed in a binary mixture of water and propylene glycol n-propyl ether (PnP) has been achieved by exploiting a phase transition [74], as depicted in fig. 2.6. The solvent, formulated at the critical mass fraction of PnP ϕ_c, is maintained at a temperature slightly below the

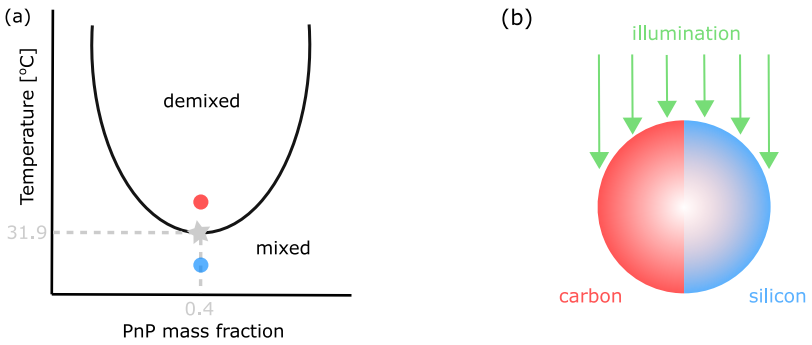

Figure 2.6.: (a) Phase diagram of water-PnP mixture. The critical point (marked with a star) is at $(\phi_c, T_c) = (0.4, 31.9\,^\circ\mathrm{C})$. (b) Schematic depiction of a self-propelled carbon-silica Janus particle. Upon shining green light, the carbon cap heats up to a temperature above the critical value [red dot in (a)], whereas the temperature on the silicon segment remains below this value [blue dot in (a)]. Local demixing of the solvent on the carbon side results in the self-propulsion of the particle by diffusiophoresis.

critical demixing temperature T_c. The system is uniformly illuminated with green light. Compared to silica, carbon absorbs light better. This leads to a non-isotropic increase in surface temperature. On the carbon side, the temperature increases above T_c and the solvent demixes into water-rich and PnP-rich phases. The mixture remains homogeneous on the silica side. The ensuing chemical gradient leads to diffusiophoretic propulsion of the colloidal Janus particle.

Besides exploiting compositional diversity, self-propulsion can also be achieved by taking advantage of, *inter alia*, Quincke rotation [24] or Marangoni stresses [75].

3 Collective behavior of elongated self-propelled particles

In contrast to isotropic (radially symmetric) particles, interactions between anisotropic particles induce aligning torques. This leads to fascinating collective phenomena like dynamical clustering of *Bacillus subtilis* [76] and *Myxococcus xanthus*, formation of ripples (counter-propagating density waves) [77] and mesoscale turbulence [78]. In this chapter, we study the collective behaviors that emerge due to anisotropy by systematically increasing the aspect ratio of constituent particles. Futhermore, we interpret observations from simulations using mean-field theory.

3.1 Brownian dynamics simulations

We perform two-dimensional simulations of $N = 1976$ elongated particles with aspect ratio κ. For a circular particle, $\kappa = 1$. A more anisotropic particle has a larger κ. Each particle propels along its long axis. We neglect translational and rotational noise; therefore the Péclet number is infinity. The dynamics of the ith particle with orientation $\tilde{\varphi}_i$ at position $\tilde{\mathbf{r}}_i$ is governed by the following overdamped equations of motion

$$\dot{\tilde{\mathbf{r}}}_i = v_0 \mathbf{e}_i - \mu_0 \nabla_i \tilde{U}, \qquad \dot{\tilde{\varphi}}_i = -\mu_\mathrm{r} \frac{\partial \tilde{U}}{\partial \tilde{\varphi}_i} \tag{3.1}$$

where v_0 is the propulsion speed, $\tilde{U} = \sum_{i<j} u_\mathrm{RGB}(\mathbf{r}_{ij}, \mathbf{e}_i, \mathbf{e}_j)$ [see eq. (2.56)] is the total potential energy of the system and $\mathbf{e}_i \equiv (\cos\varphi_i, \sin\varphi_i)^T$ is the orientation of the ith particle. The translational and rotational mobilities of each particle are μ_0 and μ_r respectively. By employing the length of the particles' shorter axis σ_0 as the

unit of length, the strength of the repulsive potential ε as the unit of energy and σ_0/v_0 as the unit of time, we get the non-dimensional equations of motion

$$\dot{\mathbf{r}}_i = \mathbf{e}_i - \nabla_i U, \qquad \dot{\varphi}_i = -3\frac{\partial U}{\partial \varphi_i}. \tag{3.2}$$

Here we have used $\mu_\mathrm{r} = 3\mu_0/\sigma_0^2$ and set μ_0 to unity. We employ periodic boundary conditions and integrate the equations of motion with a time step $\Delta t \leq 2 \times 10^{-5}$. The simulation box is rectangular with $L_x = 3L_y$. An elongated box urges the formation of a slab whose interface aligns with the shorter edge of the simulation box (here, along the y axis) [79]. We vary κ and accordingly change the dimensions of the simulation box so that the global packing fraction $\bar{\phi} = N\pi\kappa/(4L_xL_y) \simeq 0.55$ is fixed. These parameters yield a dense domain surrounded by a dilute active gas in simulations of isotropic, athermal active Brownian particles [80].

3.1.1 Local packing fraction and polarization

After the system reaches steady state, we divide it along the x axis into bins of width Δx to measure the local packing fraction

$$\phi(x_i) = \frac{N_i\pi\kappa}{4\Delta x L_y}, \tag{3.3}$$

mean polarization along the x axis (perpendicular to the interface)

$$P_x(x_i) = \frac{1}{N_i}\sum_{k\in i}\cos\varphi_k \tag{3.4}$$

and the mean absolute polarization along the y axis (parallel to the interface)

$$P_y(x_i) = \left|\frac{1}{N_i}\sum_{k\in i}\sin\varphi_k\right|. \tag{3.5}$$

The summation is performed over all particles in the ith bin. We shift the coordinates of the particles such that the center-of-mass of the system is at the origin and perform an ensemble average over 20 runs for improved statistics. The polarization along the y direction is spontaneously determined. The ensemble average is thus expected to be zero even if, in each run, the system is polarized along $\pm y$ direction. To circumvent this, we take the absolute value of the polarization to define P_y.

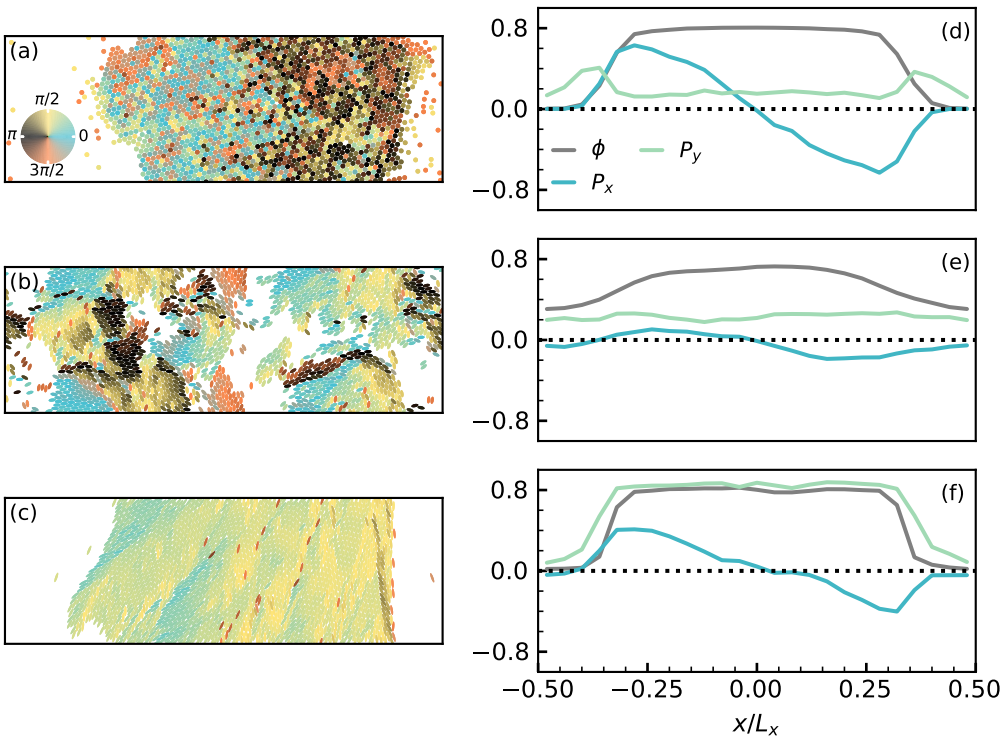

Figure 3.1.: Snapshots of the system for three different aspect ratios: (a) $\kappa = 1.0$ [discs], (b) $\kappa = 2.25$ and (c) $\kappa = 4.25$. Particles are colored according to their orientation [see the cyclic color map shown in panel (a)]. The profiles of the local packing fraction and polarization corresponding to these aspect ratios shown in panels (a–c) are respectively plotted in panels (d–f).

In fig. 3.1, we show representative snapshots of the steady state for different aspect ratios. Moreover, we plot the profiles of the local packing fraction and the components of the polarization corresponding to these aspect ratios. For $\kappa = 1$ (discs), the system forms a high-density slab surrounded by a rarefied gas of particles. The density within in the dense and dilute phases are constant. Additionally, fig. 3.1 (d) shows that P_x is antisymmetric with $P_x(x) = -P_x(-x)$. Barring the two peaks at the interface (due to "coasting" particles), the parallel polarization P_y is constant and small.

On increasing the aspect ratio to $\kappa = 2.25$, we notice that several small polarized pockets appear. These transient *polar domains* explore the entire simulation box leading to an approximately homogeneous density profile. Both P_x and P_y are small and constant. Global polar order is hence absent.

On increasing the aspect ratio further to $\kappa = 4.25$, we observe the emergence of *polar bands* characterized by global polar order. The system again separates into a dense domain that coexists with a dilute gas. In contrast to discs, as implied by the profile of P_y, the dense domain is highly polarized along the y direction. Similar to discs, the polarization perpendicular to the interface P_x is antisymmetric with particles at the interface pointing toward the dense region, thereby stabilizing the inhomogeneous polar band.

To put in a nutshell, simulations indicate two transitions: from MIPS at small aspect ratios to transient polar domains at intermediate aspect ratios and from polar domains to an inhomogeneous state with global polar order at large aspect ratios.

3.1.2 Phase diagram from simulations

To summarize these observations, we construct a phase diagram using relevant order parameters (packing fraction and polarization). To this end, we extract the value of the order parameter $\mathcal{P}$ in the dense region $\mathcal{P}^+$ and dilute region $\mathcal{P}^-$ using the functional form

$$\mathcal{P}(x) = \frac{\mathcal{P}^+ + \mathcal{P}^-}{2} + \frac{\mathcal{P}^+ - \mathcal{P}^-}{2} \tanh\left(\frac{x - x_0}{2w}\right) \tag{3.6}$$

where x_0 is the position of the interface and w is a measure of the width of the interface. As shown in fig. 3.2, the density is well-fitted by eq. (3.6). For $\kappa \geq 2.9$, the parallel polarization P_y can also be fitted with the same functional form. Before fitting, we split the profile into two halves that lie on either side of the origin and average over them.

For $1 \leq \kappa < 1.15$, the density of the dense and dilute regions are largely different. On increasing κ, in the polar domains phase ($1.15 \leq \kappa < 2.9$), this difference narrows down and eventually in the polar bands phase ($\kappa \geq 2.9$), the difference widens again. In the polar bands phase, the dense region is highly polarized and the dilute region has a lower, albeit non-zero, polarization. On introducing rotational diffusion, we expect the polarization of the dilute region to be zero.

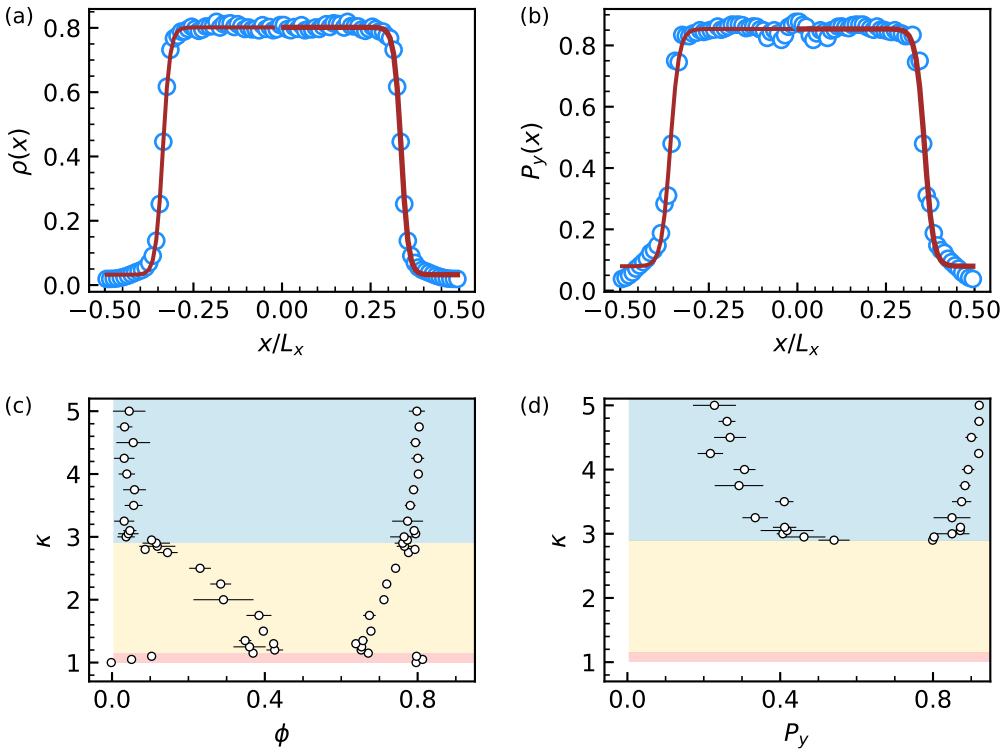

Figure 3.2.: Phase behavior of active ellipsoids. (a) Density profile $\rho(x)$ (blue circles) and the corresponding fit using eq. (3.6) (maroon line). (b) Parallel polarization $P_y(x)$ (blue circles) and the corresponding fit. (c) Packing fraction $\phi^{\pm}$ and (d) polarization $P_y^{\pm}$ of the coexisting phases for different κ. Error bars represent the standard error. The colors in the background indicate the three distinct phases: MIPS, polar domains and polar bands (from bottom to top). Panels (c) and (d) are reproduced in adapted form from Ref. [81].

3.2 Mean-field theory

In this section, we will extend the mean-field theory outlined in section 2.2.2 to describe the collective behavior of anisotropic particles.

3.2.1 Evolution equation for the one-body density

The evolution equation for the joint probability distribution $\psi_N(\{\mathbf{r}_i, \varphi_i\}; t)$, which now includes a torque term, is given by

$$\partial_t \psi_N = -\sum_{i=1}^{N} \left\{ \nabla_i \cdot \left[\mathbf{e}_i - \nabla_i U \right] \psi_N + 3 \sum_{i=1}^{N} \frac{\partial}{\partial \varphi_i} \left(\frac{\partial U}{\partial \varphi_i} \psi_N \right) \right\}. \tag{3.7}$$

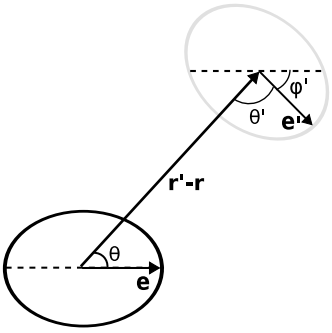

Figure 3.3: Tagged particle's frame of reference. The positions and orientations of other particles (for *e.g.*, the particle shown in grey here) are measured in this reference frame. Without loss of generality, we align the orientation of the tagged particle $\mathbf{e}$ to the x axis. With this, $\theta + \varphi' + \theta' = \pi$.

On integrating both sides over $\int \mathrm{d}\mathbf{r}_2 \ldots \mathrm{d}\mathbf{r}_N \int \mathrm{d}\varphi_2 \ldots \varphi_N$, we get the following evolution equation for the one-body density $\psi(\mathbf{r}, \varphi; t)$

$$\partial_t \psi = -\nabla \cdot [\mathbf{e}\psi - \mathbf{f}] - 3\frac{\partial(\tau\psi)}{\partial\varphi} + D_\mathrm{r}\partial_\varphi^2\psi \tag{3.8}$$

with force density

$$\mathbf{f}(\mathbf{r}, \varphi; t) = \int \mathrm{d}\mathbf{r}' \int \mathrm{d}\varphi' \, [-\nabla u(\mathbf{r}' - \mathbf{r}, \varphi')]\psi_2(\mathbf{r}, \varphi, \mathbf{r}', \varphi'; t) \tag{3.9}$$

where $\psi_2(\mathbf{r}, \varphi, \mathbf{r}', \varphi'; t)$ is the two-body density and u is the repulsive Gay-Berne pair potential[1] defined in eq. (2.56). Here we have introduced an effective rotational diffusion (with diffusion constant D_r) that arises from coarse-graining. We decompose ψ_2 as

$$\psi_2(\mathbf{r}, \varphi, \mathbf{r}', \varphi'; t) = \psi_c(\mathbf{r}', \varphi'|\mathbf{r}, \varphi; t)\psi(\mathbf{r}, t) \tag{3.10}$$

where ψ_c is the conditional probability density of finding a particle with orientation φ' at $\mathbf{r}'$ given a particle with orientation φ at $\mathbf{r}$. For short-ranged potentials like those employed here, we can perform a Taylor expansion of the density about $\mathbf{r}$ to obtain the density at position $\mathbf{r}'$ and retain only the lowest order term[2] to get $\rho(\mathbf{r}', t) \approx \rho(\mathbf{r}, t)$. Assuming that the pair correlation function $g(\mathbf{r}, \mathbf{r}', \varphi, \varphi'; t)$ is time-independent and translationally invariant, we can further factorize ψ_c eventually yielding

$$\psi_2 = \rho(\mathbf{r}, t)g(\mathbf{r} - \mathbf{r}', \varphi, \varphi')\psi(\mathbf{r}, t). \tag{3.11}$$

Note that in contrast to isotropic particles [see eq. (2.47)], the φ'-dependence of the pair distribution function is retained here. We now shift to the frame of reference of an arbitrary tagged particle at $\mathbf{r}$. In this frame, as shown in fig. 3.3, the other

[1] As long as the potential is short-ranged, its exact form is irrelevant to the theory.
[2] $\rho(\mathbf{r}', t) = \rho(\mathbf{r}, t) + \nabla\rho|_{(\mathbf{r},t)} \cdot (\mathbf{r}' - \mathbf{r}) + \cdots \approx \rho(\mathbf{r}, t)$

particle is at a distance of $|\mathbf{r}-\mathbf{r}'|$. The angle enclosed by the orientation of the tagged particle $\mathbf{e}$ with $\mathbf{r}-\mathbf{r}'$ is θ. The orientation of the other particle $\mathbf{e}'$ subtends an angle θ' with $\mathbf{r}-\mathbf{r}'$. In this coordinate system, the force density in eq. (3.9) becomes

$$\mathbf{f}(\mathbf{r},\varphi;t)=\rho(\mathbf{r},t)\int_0^{2\pi}\mathrm{d}\varphi'\int_0^{2\pi}\mathrm{d}\theta\int_0^{\infty}\mathrm{d}r\;r[-\nabla u(\mathbf{r}-\mathbf{r}',\varphi,\varphi')]g(r,\theta,\varphi'). \quad (3.12)$$

On projecting the force density $\mathbf{f}$ on the orientation $\mathbf{e}$, we get

$$\begin{aligned}\mathbf{e}\cdot\mathbf{f} &=: -\zeta\rho\psi\\ &= \frac{\partial u}{\partial r}\cos\theta+\frac{1}{r}\frac{\partial u}{\partial\theta}\sin\theta.\end{aligned} \quad (3.13)$$

The force-imbalance coefficient ζ, defined as

$$\zeta\equiv\int_0^{2\pi}\mathrm{d}\varphi'\int_0^{2\pi}\mathrm{d}\theta\int_0^{\infty}\mathrm{d}r\;r\left[-\frac{\partial u}{\partial r}\right]\cos\theta g(r,\theta,\varphi'), \quad (3.14)$$

is a measure of anisotropy in the distribution of particles around the tagged particle [35]. Due to symmetry, the sine term in eq. (3.13) does not contribute to the integral. Similarly, the torque can be written as

$$\begin{aligned}\tau(\mathbf{r},\varphi;t) &= \rho(\mathbf{r},t)\int_0^{2\pi}\mathrm{d}\varphi'\int_0^{2\pi}\mathrm{d}\theta\int_0^{\infty}\mathrm{d}r\;r[-\partial_\varphi u(\mathbf{r}-\mathbf{r}',\varphi,\varphi')]g(r,\theta,\varphi')\\ &=: \mathbf{n}\cdot\mathbf{R}\cdot\mathbf{e}\end{aligned} \quad (3.15)$$

with

$$n_i(\mathbf{r},t)=\rho(\mathbf{r},t)\int_0^{2\pi}\mathrm{d}\varphi'\int_0^{2\pi}\mathrm{d}\theta\int_0^{\infty}\mathrm{d}r\;r\left[-\frac{\partial u}{\partial e_i}\right]g(r,\theta,\varphi') \quad (3.16)$$

and rotation matrix

$$\mathbf{R}=\begin{pmatrix}0 & -1\\ 1 & 0\end{pmatrix}. \quad (3.17)$$

In terms of the quantities we have introduced, the evolution equation for the one-body density [eq. (3.8)] becomes

$$\partial_t\psi=-\nabla\cdot\left[v(\rho)\mathbf{e}\psi\right]-3\frac{\partial}{\partial\varphi}[\mathbf{n}\cdot\mathbf{R}\cdot\mathbf{e}\psi]+D_\mathrm{r}\partial_\varphi^2\psi \quad (3.18)$$

with density-dependent speed $v(\rho)=1-\zeta\rho$ that captures the effect of inter-particle forces. To gain insight into the implications of eq. (3.18), we now derive evolution

equations for the orientational moments of ψ introduced in section 2.2.2. At this stage, a closure for the field $\mathbf{n}$ also remains to be obtained.

3.2.2 Hydrodynamic equations

Integrating both sides of eq. (3.18) over φ, we find that the density $\rho(\mathbf{r}, t)$ is governed by

$$\begin{aligned}\partial_t \rho &= -\nabla \cdot \left[v(\rho) \int_0^{2\pi} \mathrm{d}\varphi \; \mathbf{e}\psi \right] - 3 \int_0^{2\pi} \mathrm{d}\varphi \; \frac{\partial}{\partial \varphi} [\mathbf{n} \cdot \mathbf{R} \cdot \mathbf{e}\psi] + D_\mathrm{r} \int_0^{2\pi} \mathrm{d}\varphi \; \partial_\varphi^2 \psi \\ &= -\nabla \cdot [v(\rho)\mathbf{p}] \end{aligned} \tag{3.19}$$

where $\mathbf{p}$ is the polarization density. The contributions from torques and rotational diffusion vanish due to 2π-periodicity of ψ and its derivatives. This is expected because neither directly affect the position of particles. Due to the absence of translational diffusion, the evolution of ρ is solely determined by the active current $v(\rho)\mathbf{p}$. On multiplying both sides of eq. (3.18) by $\mathbf{e}$ and integrating over φ, we get

$$\partial_t \mathbf{p} = -\nabla \cdot \left[v(\rho) \int_0^{2\pi} \mathrm{d}\varphi \; \mathbf{e} \otimes \mathbf{e} \right] - 3 \int_0^{2\pi} \mathrm{d}\varphi \; \mathbf{e} \frac{\partial}{\partial \varphi} [\mathbf{n} \cdot \mathbf{R} \cdot \mathbf{e}\psi] + D_\mathrm{r} \int_0^{2\pi} \mathrm{d}\varphi \; \mathbf{e} \frac{\partial^2 \psi}{\partial \varphi^2}. \tag{3.20}$$

Using the definition of $\mathbf{Q}$, the first term can be simplified as

$$-\nabla \cdot \left\{ v(\rho) \left[\mathbf{Q} + \frac{\mathbf{1}}{2} \int_0^{2\pi} \mathrm{d}\varphi \; \psi \right] \right\} = -\nabla \cdot \left\{ v(\rho) \left[\mathbf{Q} + \frac{\mathbf{1}}{2} \rho \right] \right\}. \tag{3.21}$$

On performing partial integration, the contribution from torques becomes

$$-3 \left[\underbrace{\mathbf{e}(\mathbf{n} \cdot \mathbf{R} \cdot \mathbf{e})\psi|_0^{2\pi}}_{=0} - \int_0^{2\pi} \mathrm{d}\varphi \; (\mathbf{R} \cdot \mathbf{e})(\mathbf{n} \cdot \mathbf{R} \cdot \mathbf{e})\psi \right]. \tag{3.22}$$

For convenience, we rewrite the expression in Einstein notation and approximate $\mathbf{n}$ to be φ-independent to get

$$3 R_{il} n_k R_{kj} \int_0^{2\pi} \mathrm{d}\varphi \; e_l e_j \psi = 3 \left(R_{il} Q_{lj} R_{kj} n_k + \frac{1}{2} R_{ij} R_{kj} n_k \rho \right). \tag{3.23}$$

Using $\mathbf{R} \cdot \mathbf{Q} \cdot \mathbf{R}^T = -\mathbf{Q}$ and $\mathbf{R} \cdot \mathbf{R}^T = -\mathbf{1}$, the above expression simplifies to

$$3 \left(-\mathbf{Q} \cdot \mathbf{n} + \frac{1}{2} \rho \mathbf{n} \right). \tag{3.24}$$

The contribution of rotational diffusion can be readily obtained by performing partial integration twice as

$$D_{\mathrm{r}}\left[\underbrace{\mathbf{e}\frac{\partial\psi}{\partial\varphi}\Big|_0^{2\pi}}_{=0}-\left\{\underbrace{\frac{\partial\mathbf{e}}{\partial\varphi}\Big|_0^{2\pi}}_{=0}-\int_0^{2\pi}\mathrm{d}\varphi\;\frac{\partial^2\mathbf{e}}{\partial\varphi^2}\psi\right\}\right]=-D_{\mathrm{r}}\int_0^{2\pi}\mathrm{d}\varphi\;\mathbf{e}\psi=-D_{\mathrm{r}}\mathbf{p}. \quad (3.25)$$

Here we have used $\frac{\partial^2\mathbf{e}}{\partial\varphi^2}=-\mathbf{e}$. Putting all terms together we obtain the evolution equation for $\mathbf{p}$ to be

$$\partial_t\mathbf{p}=-\nabla\cdot\left[v(\rho)\left(\frac{1}{2}\rho\mathbf{1}+\mathbf{Q}\right)\right]-D_{\mathrm{r}}\mathbf{p}-3\left(\mathbf{Q}\cdot\mathbf{n}-\frac{1}{2}\rho\mathbf{n}\right). \quad (3.26)$$

To obtain the equation governing the second moment $\mathbf{Q}$, we multiply both sides of eq. (3.18) by $(\mathbf{e}\otimes\mathbf{e}-\frac{\mathbf{1}}{2})$ and integrate over φ. The integral involving $v(\rho)$ evaluates to

$$-\nabla\cdot\left[v(\rho)\int_0^{2\pi}\mathrm{d}\varphi\;\left(\mathbf{e}\otimes\mathbf{e}-\frac{\mathbf{1}}{2}\right)\otimes\mathbf{e}\psi\right]=-\nabla\cdot\left[v(\rho)\left(\mathbf{W}-\frac{1}{2}\mathbf{1}\otimes\mathbf{p}\right)\right] \quad (3.27)$$

where $W_{ijk}=\int_0^{2\pi}\mathrm{d}\varphi\;e_ie_je_k\psi$. The second term involving torques becomes

$$-3\left[\underbrace{\left(e_ie_j-\frac{1}{2}\delta_{ij}\right)n_kR_{kl}e_l\psi\Big|_0^{2\pi}}_{=0}-\int_0^{2\pi}\mathrm{d}\varphi\;\frac{\partial}{\partial\varphi}\left(e_ie_j-\frac{1}{2}\delta_{ij}\right)n_kR_{kl}e_l\right]$$
$$=3n_kR_{kl}\left(R_{jn}W_{lni}+R_{im}W_{lmj}\right) \quad (3.28)$$

where we have used $\frac{\partial}{\partial\varphi}(e_ie_j)=e_iR_{jn}e_n+e_jR_{im}e_m$. On evaluating the contribution from rotational diffusion by performing partial integration, the only term that remains is

$$D_{\mathrm{r}}\int_0^{2\pi}\mathrm{d}\varphi\;\frac{\partial^2}{\partial\varphi^2}\left(e_ie_j\right)\psi=2D_{\mathrm{r}}\int_0^{2\pi}\mathrm{d}\varphi\;\frac{\partial^2}{\partial\varphi^2}(e_i)e_j+\frac{\partial e_i}{\partial\varphi}\frac{\partial e_j}{\partial\varphi}=-4D_{\mathrm{r}}Q_{ij}. \quad (3.29)$$

We have plugged in $(\partial_\varphi e_i)(\partial_\varphi e_j)=\delta_{ij}-e_ie_j$ in the last step. On gathering terms, we obtain the evolution equation for $\mathbf{Q}$ to be

$$\partial_tQ_{ij}=-\partial_k\left[v(\rho)\left(W_{ijk}-\frac{1}{2}\delta_{ij}p_k\right)\right]+3n_kR_{kl}\left(R_{jn}W_{lni}+R_{im}W_{lmj}\right)-4D_{\mathrm{r}}Q_{ij}. \quad (3.30)$$

The field $\mathbf{n}(\mathbf{r}, t)$

To make eq. (3.18) an equation with only one-body contributions, we should approximate $\mathbf{n}$. To gain insight into the form of the closure, we turn to simulations. To this end, we divide the system along the x axis and extract the mean field experienced by particles

$$N_x(x_i) = \left\langle \frac{1}{N_i} \sum_{k \in i} -\frac{\partial u}{\partial e_{x_k}} \right\rangle$$
$$N_y(x_i) = \left\langle \left| \frac{1}{N_i} \sum_{k \in i} -\frac{\partial u}{\partial e_{y_k}} \right| \right\rangle \tag{3.31}$$

in bin i. The measured field for different aspect ratios is shown in fig. 3.4. We find that N_x fluctuates about zero for all aspect ratios, albeit visibly stronger for larger aspect ratios. On the other hand, N_y is negligibly small for small aspect ratios but becomes qualitatively similar[3] to P_y for $\kappa = 4.25$. Thus, for polar bands (seen at large κ), $N_y \sim P_y$. We thus propose that the field is proportional to the polarization, *i.e.*, $\mathbf{n} = \chi \mathbf{p}$. The strength with which $\mathbf{n}$ is coupled to $\mathbf{p}$ is quantified by the coupling constant χ. A larger χ is indicative of stronger alignment. In Ref. [82], the authors perform the closure by considering the field to be proportional to $\nabla\rho$. On inspecting the density in fig. 3.1, this should mean N_x displays two hummocks at the interface between the dilute and dense regions. Since this is not what we observe, we infer that the field is determined by the polarization rather than the density gradient.

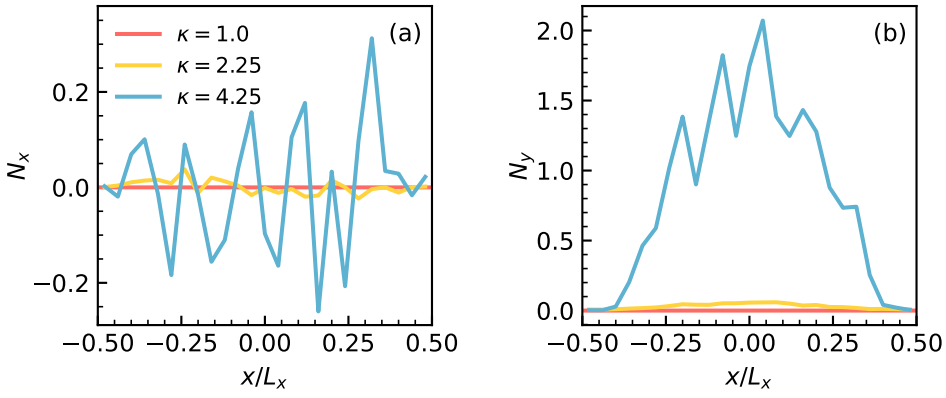

Figure 3.4.: Profiles of (a) N_x and (b) N_y [defined in eq. (3.31)] for different aspect ratios κ. Consistent with fig. 3.2, the colors are representative of the phases into which the system emerges. The aspect ratios chosen here correspond to those shown in fig. 3.1. Reproduced from Ref. [81].

[3] Since most particles point in the same direction, it is arduous to obtain improved statistics.

Closure

To proceed further, we must close the hierarchy of moments. We do so by setting the third moment to zero, *i.e.*, $\int_0^{2\pi} \mathrm{d}\varphi \, \left(e_i e_j e_k - \frac{3}{4}\delta_{ij} e_k\right) \psi = 0$. Through this, we can relate the components of $\mathbf{W}$ to $\mathbf{p}$ as follows

$$\begin{aligned} W_{111} &= \frac{3}{4} p_1, \\ W_{222} &= \frac{3}{4} p_2, \\ W_{122} = W_{212} = W_{221} &= \frac{1}{4} p_1, \\ W_{112} = W_{121} = W_{211} &= \frac{1}{4} p_2. \end{aligned} \tag{3.32}$$

On applying the closure to the first term in eq. (3.30), it reduces to

$$-\frac{1}{4}\left[\nabla(v\mathbf{p}) + (\nabla(v\mathbf{p}))^T - (\nabla \cdot v\mathbf{p})\mathbf{1}\right]. \tag{3.33}$$

Substituting $\mathbf{n} = \chi\mathbf{p}$ in the second term in eq. (3.30) and applying the closure [eq. (3.32)], we get

$$3\left(n_k R_{kl} R_{im} W_{lmj} + n_k R_{kl} R_{jn} W_{lni}\right) = \underbrace{\frac{3}{4}\begin{pmatrix} n_1 p_1 - n_2 p_2 & 3n_1 p_2 - n_2 p_1 \\ 3n_2 p_1 - n_1 p_2 & n_2 p_2 - n_1 p_1 \end{pmatrix}}_{=\mathbf{A}} + \mathbf{A}^T \tag{3.34}$$

$$= 3\chi\left(\mathbf{p}\otimes\mathbf{p} - \frac{1}{2}p^2\mathbf{1}\right). \tag{3.35}$$

Note that the matrix is symmetric and traceless. Furthermore, by assuming $\partial_t \mathbf{Q} = 0$, we find that the nematic tensor and polarization are related through

$$\mathbf{Q} = \mathbf{Q}_\nabla + \frac{\gamma}{4}\left(\mathbf{p}\otimes\mathbf{p} - \frac{1}{2}p^2\mathbf{1}\right) \tag{3.36}$$

with

$$\mathbf{Q}_\nabla = -\frac{1}{16 D_\mathrm{r}}\left[\nabla(v\mathbf{p}) + (\nabla(v\mathbf{p}))^T - (\nabla\cdot v\mathbf{p})\mathbf{1}\right]. \tag{3.37}$$

With this relation, eq. (3.26) can be written as

$$\partial_t \mathbf{p} + \Lambda_-(\mathbf{p}\cdot\nabla)\mathbf{p} = -\frac{1}{2}\nabla(v\rho) - \mathbf{Q}\cdot\nabla v + \frac{\gamma p^2}{16}\nabla v + \frac{v}{16}\nabla^2(v\mathbf{p}) - \Lambda_+\left[(\nabla\cdot\mathbf{p})\mathbf{p} - \frac{1}{2}\nabla p^2\right] - \left(1 - \frac{\gamma\rho}{2} + \frac{\gamma^2 p^2}{8}\right)\mathbf{p} \quad (3.38)$$

where $\Lambda_\pm(\rho) = \frac{4\pm1}{16}\gamma v(\rho)$. Here we have non-dimensionalized the equation by choosing l_0 as the length scale and $\tau_0 = D_\mathrm{r}^{-1}$ as the time scale. This equation is identical to that obtained by Farrell *et al.* [83] apart from terms originating from $\mathbf{Q}\cdot\nabla v$.

Homogeneous steady state

When the system is homogeneous and in steady state, all temporal and spatial derivatives in the evolution equations vanish. While referring to variables in this state, we use an overbar. With $\mathbf{n} = \chi\mathbf{p}$, we have $\bar{\mathbf{Q}}\cdot\bar{\mathbf{n}} = (\bar{p}^2/8)\bar{\mathbf{p}}$. From eq. (3.26), we get

$$\left(1 - \frac{\gamma\bar{\rho}}{2} + \frac{\gamma^2\bar{p}^2}{8}\right)\bar{p} = 0. \quad (3.39)$$

The polarization has two solutions:

$$\bar{p} = 0, \quad \frac{2}{\gamma}\sqrt{\gamma\bar{\rho} - 2}. \quad (3.40)$$

Since $\bar{p}$ has to be real, the second solution only exists if $\gamma\bar{\rho} \geq 2$. The direction of $\bar{\mathbf{p}}$ is spontaneously determined and not stipulated.

3.2.3 Linear stability analysis

To examine the dynamics of the system near the steady state, we perform a linear stability analysis. We are interested in determining if this state is stable or unstable based on whether small perturbations to it decays or grows. By definition, the steady state Ψ_0 satisfies $\partial_t\Psi_0 = \mathcal{L}_\Psi\Psi_0 = 0$ where $\mathcal{L}_\Psi$ is the time-evolution operator. On perturbing Ψ_0 by $\varepsilon\Psi'$ to get to state $\Psi = \Psi_0 + \varepsilon\Psi'$ and neglecting terms of order $\mathcal{O}(\varepsilon^2)$ and higher, we obtain a linearized differential equation given by

$$\partial_t\Psi' = \mathcal{L}\Psi' \quad (3.41)$$

where $\mathcal{L}$ is the linearized version of $\mathcal{L}_\Psi$. The (linear) stability of the system is governed by the sign of the real part of $\mathcal{L}$'s eigenvalues with positive eigenvalues indicating instability of the steady state.

On considering perturbations of density and polarization about their values in steady state, we get

$$\rho = \bar{\rho} + \delta\rho, \qquad \mathbf{p} = \bar{\mathbf{p}} + \delta\mathbf{p}. \tag{3.42}$$

Without loss of generality, we set the direction of the polarization of the homogeneous state to be along the y axis, *i.e.*, $\bar{\mathbf{p}} = \bar{p}\mathbf{e}_y$. Linearizing eqs. (3.19) by ignoring terms containing perturbations of order larger than unity, we get the evolution equation for $\delta\rho$ to be

$$\partial_t \delta\rho = -\bar{v}\nabla\cdot\delta\mathbf{p} + \zeta\bar{p}\mathbf{e}_y\cdot\nabla\delta\rho \tag{3.43}$$

where $\bar{v} = v(\bar{\rho}) = 1 - \zeta\bar{\rho}$. Following similar procedure, the perturbation to the polarization evolves according to

$$\begin{aligned}\partial_t\delta\mathbf{p} = &-\frac{1}{2}\left(\bar{v} - \zeta\bar{\rho} + \frac{\zeta}{2\gamma}\varepsilon\right)\nabla\delta\rho + \zeta\bar{\mathbf{Q}}\cdot\nabla\delta\rho + D\nabla^2\delta\mathbf{p} \\ &- \frac{\bar{v}\sqrt{\varepsilon}}{8}\left[5(\nabla\cdot\delta\mathbf{p})\mathbf{e}_y - 3(\partial_x\delta p_y - \partial_y\delta p_x)\mathbf{e}_x - 2\nabla(\mathbf{e}_y\cdot\delta\mathbf{p})\right] \\ &+ \sqrt{\varepsilon}\mathbf{e}_y\delta\rho - \frac{\bar{v}\bar{\rho}\zeta\sqrt{\varepsilon}}{8(2+\varepsilon)}\mathbf{e}_y\nabla^2\delta\rho - \frac{\varepsilon}{2}\delta\mathbf{p} - \gamma\bar{\mathbf{Q}}\cdot\delta\mathbf{p}\end{aligned} \tag{3.44}$$

where $D = \bar{v}^2/16$, $\gamma\bar{\rho} = 2+\varepsilon$ and $\gamma\bar{p} = 2\sqrt{\varepsilon}$. The steady-state nematic tensor $\bar{\mathbf{Q}}$ is

$$\bar{\mathbf{Q}} = \frac{\varepsilon}{2\gamma}\begin{pmatrix} -1 & 0 \\ 0 & 1 \end{pmatrix}. \tag{3.45}$$

We now gather the perturbations in a vector $\mathbf{X} \equiv (\delta\rho, \delta p_x, \delta p_y)^T$. The Fourier counterpart of $\mathbf{X}$ is

$$\tilde{\mathbf{X}}(\mathbf{q}, t) = \int \mathrm{d}^2\mathbf{r}\ \mathbf{X}(\mathbf{r}, t)\mathrm{e}^{-\mathrm{i}\mathbf{q}.\mathbf{r}}. \tag{3.46}$$

The evolution of $\tilde{\mathbf{X}}$ can be written, in general, as

$$\partial_t\tilde{\mathbf{X}}(\mathbf{q}, t) = -\mathbf{M}(\mathbf{q})\cdot\tilde{\mathbf{X}}(\mathbf{q}, t). \tag{3.47}$$

The entries of $\mathbf{M}$ are obtained from the evolution equations of the components of $\mathbf{X}$ (or, equivalently $\tilde{\mathbf{X}}$). The solution of the eigenvalue equation is

$$\tilde{\mathbf{X}}(\mathbf{q},t) = \sum_{i=1}^{3} c_i(\mathbf{q})\mathbf{w}_i(\mathbf{q})\mathrm{e}^{-\lambda_i(\mathbf{q})t} \tag{3.48}$$

where λ_i are the eigenvalues corresponding to the eigenvectors $\mathbf{w}_i$. Negativity of λ_i indicates instability. At this stage, we will handle the apolar and polar homogeneous steady states separately.

Case 1: Homogeneous apolar state ($\bar{\mathbf{p}} = 0$)

In this case, $\bar{\mathbf{p}} = 0$ and $\mathbf{p} = \delta\mathbf{p}$. Equations (3.43) and (3.44) respectively reduce to

$$\partial_t \delta\rho = -\bar{v}\nabla\cdot\delta\mathbf{p} \tag{3.49}$$

and

$$\partial_t \delta\mathbf{p} = -\frac{1}{2}\left(\bar{v} - \zeta\bar{\rho}\right)\nabla\delta\rho + D\nabla^2\delta\mathbf{p} - \frac{\varepsilon}{2}\delta\mathbf{p}. \tag{3.50}$$

The matrix $\mathbf{M}$ is given by

$$\mathbf{M} = \begin{pmatrix} 0 & \mathrm{i}\bar{v}q_x & \mathrm{i}\bar{v}q_y \\ \frac{1}{2}(\bar{v}-\zeta\bar{\rho})\mathrm{i}q_x & \frac{\varepsilon}{2} + Dq^2 & 0 \\ \frac{1}{2}(\bar{v}-\zeta\bar{\rho})\mathrm{i}q_y & 0 & \frac{\varepsilon}{2} + Dq^2 \end{pmatrix}. \tag{3.51}$$

Here $\frac{\varepsilon}{2} = 1 - \frac{1}{2}\gamma\bar{\rho}$ is the rate at which the polarization relaxes: larger the γ, slower the relaxation. The eigenvalues of $\mathbf{M}$ are

$$\begin{aligned} \lambda_0 &= \frac{\varepsilon}{2} + Dq^2, \\ \lambda_\pm &= \frac{1}{2}\left(\frac{\varepsilon}{2} + Dq^2\right) \pm \frac{1}{2}\sqrt{\left(\frac{\varepsilon}{2} + Dq^2\right)^2 - 2\bar{v}(\bar{v}-\zeta\bar{\rho})q^2}. \end{aligned} \tag{3.52}$$

Since ε is positive, $\lambda_0 > 0$. We expand $\lambda_\pm$ about $q = 0$. To lowest order, we find λ_+ is positive and

$$\lambda_- = \frac{\bar{v}(\bar{v}-\zeta\bar{\rho})}{\varepsilon}q^2. \tag{3.53}$$

For $(1-\zeta\bar{\rho})(1-2\zeta\bar{\rho}) < 0$, this eigenvalue becomes negative. The homogeneous apolar state is therefore unstable if $\frac{1}{2} \le \zeta\bar{\rho} \le 1$. This criterion is independent of γ.

Case 2: Homogeneous polar state ($\bar{\mathbf{p}} \neq 0$)

On considering plane-wave perturbations ($\sim \mathrm{e}^{\mathrm{i}qx}$) perpendicular to $\bar{\mathbf{p}}$, the matrix $\mathbf{M}$ becomes

$$\mathbf{M} = \begin{pmatrix} 0 & \mathrm{i}\bar{v}q & 0 \\ \mathrm{i}bq & Dq^2 & -5\mathrm{i}aq \\ -(1+\frac{\bar{v}\zeta\bar{\rho}}{8(2+\varepsilon)}q^2)\sqrt{\varepsilon} & 5\mathrm{i}aq & \varepsilon + Dq^2 \end{pmatrix} \tag{3.54}$$

with coefficients $a \equiv (\bar{v}/8)\sqrt{\varepsilon}$ and

$$b \equiv \frac{1}{2}\left(\bar{v} - \zeta\bar{\rho} + \frac{3\zeta}{2\gamma}\varepsilon\right) = \frac{1}{2} - \frac{8+\varepsilon}{8+4\varepsilon}\zeta\bar{\rho}. \tag{3.55}$$

The characteristic polynomial of $\mathbf{M}(q)$ given by $P(\lambda) = a_0 + a_1\lambda + a_2\lambda^2 + \lambda^3$ with $(\lambda \to -\lambda)$ has coefficients

$$\begin{aligned} a_0(q) &= (\bar{v}b - 10D)\,\varepsilon q^2 + \bar{v}\left(b - \frac{5\varepsilon}{8+4\varepsilon}\zeta\bar{\rho}\right)Dq^4, \\ a_1(q) &= \left(\bar{v}b - \frac{21}{4}\varepsilon D\right)q^2 + D^2q^4, \\ a_2(q) &= \varepsilon + 2Dq^2. \end{aligned} \tag{3.56}$$

The Routh-Hurwitz stability criteria [84] is a test to conclude whether or not the roots of a polynomial have negative real parts. For our purpose, this test is useful in determining stability.[4] The criteria for a third degree polynomial are:

$$a_0 > 0, \qquad a_1a_2 > a_0, \qquad a_2 > 0. \tag{3.57}$$

For $a_0 > 0$, we require

$$\varepsilon > \frac{6\zeta\bar{\rho}+2}{3\zeta\bar{\rho}-1}, \qquad \zeta\bar{\rho} > \frac{1}{3}. \tag{3.58}$$

Since $\varepsilon = \gamma\bar{\rho} - 2 > 0$ for a polar homogeneous state, $a_2 > 0$. The second condition $a_1a_2 > a_0$ reduces to

$$\left(10 - \frac{21}{4}\varepsilon\right)D\varepsilon q^2 + \left[\bar{v}\left(\frac{1}{2} - \frac{8-4\varepsilon}{8+4\varepsilon}\zeta\bar{\rho}\right) - \frac{19}{2}\varepsilon D\right]Dq^4 + 2D^3q^6 > 0. \tag{3.59}$$

Considering the limit of small q and examining the q^2 term, we find that the inequality is satisfied if $\varepsilon < \frac{40}{21}$. This condition cannot be satisfied alongside the inequality

[4] Note that we have changed $\lambda \to -\lambda$ while writing down $P(\lambda)$. This is done to be consistent with the form of the Routh-Hurwitz criteria we employ.

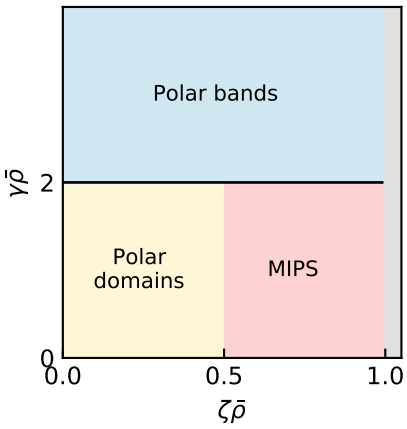

Figure 3.5: Phase diagram obtained from linear stability analysis of polar and apolar homogeneous steady-states. The boundary between MIPS and polar domains corresponds to a spinodal and the solid line at $\gamma\bar{\rho}$ is critical line. Non-negativity of $v(\rho)$ renders the grey region physically inaccessible. The colors corresponding to the qualitatively different phases follow the scheme shown in fig. 3.2. Reproduced in adapted form from Ref. [81].

in (3.58). Therefore, the homogeneous polar state is unconditionally unstable and emerges into polar bands with global polar order.

We summarize the results of the stability analysis in fig. 3.5. For $\gamma\bar{\rho} < 2$, the spinodal is located at $\zeta\bar{\rho} = \frac{1}{2}$. If $\zeta\bar{\rho} < \frac{1}{2}$, the homogeneous, apolar state is stable and dynamical polar domains are observed; if not, density perturbations grow exponentially and give rise to macroscopic phase separation induced by motility. On the other hand, at $\gamma\bar{\rho} = 2$, the rate at which the polarization decays (given by $1 - \frac{\gamma\bar{\rho}}{2}$) vanishes, indicating a critical transition to polar bands which exhibits global polar order.

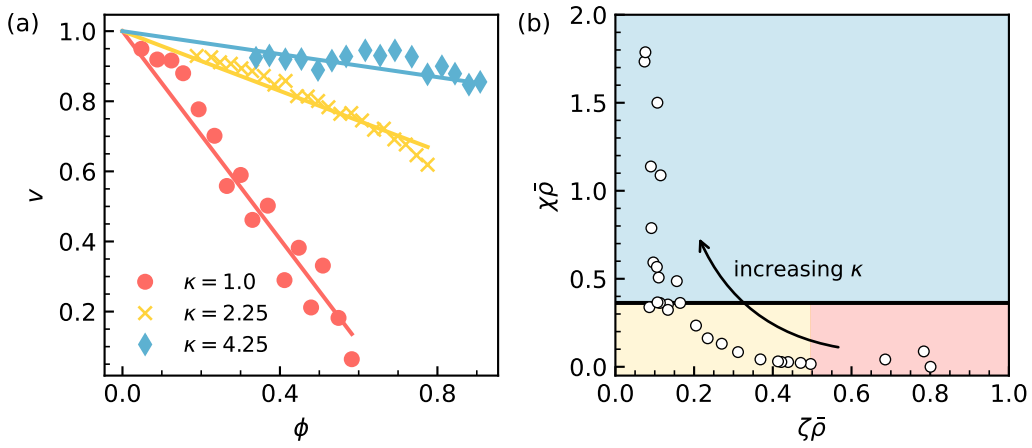

Figure 3.6.: (a) Density-dependent speed v as a function of local packing fraction ϕ. The markers correspond to simulation data and the solid lines are fits to the function $f(\phi) = 1 - \zeta\phi$. (b) Coupling strength χ and force-imbalance coefficient ζ extracted from simulations. The background colors denote the three phases observed on increasing κ (indicated by the arrow): MIPS $\rightarrow$ Polar domains $\rightarrow$ Polar bands. Reproduced in adapted form from Ref. [81].

We now proceed to verify the result of linear stability analysis by extracting the coefficients χ and ζ from simulations. From the profiles of $\rho(x)$, $P_y(x)$ and $N_y(x)$, we fit for a proportionality constant $\chi = N_y/(\rho P_y)$ for varying aspect ratios. To determine ζ, we bin the system along the x axis, calculate the mean projection of the velocity on the orientation vector $v(x_i) = \langle \sum_{k \in i} \dot{\mathbf{r}}_k \cdot \mathbf{e}_k \rangle$ and plot it as a function of local packing fraction $\phi(x_i)$. The sum runs over all particles within bin i. We fit the linear decay of v with ϕ [cf. fig. 3.6] to extract the slope ζ.

Figure 3.6 shows that as κ increases, the speed of particles is less affected by local crowding. Alignment provides an escape from slow down of particles' dynamics. This is reflected in the decrease in ζ. Concurrently, the coupling strength χ is practically unchanged. Below $\zeta\bar{\rho} \approx \frac{1}{2}$, MIPS breaks down into several mobile clusters. On increasing κ further, the orientational coupling χ increases significantly while ζ is small (but non-zero) and independent of κ. This leads to the transition into a highly polarized and dense band that travels parallel to the y axis.

4 Forces and torques on objects immersed in active fluids

Liberated from the shackles of detailed balance due to persistent directed motion, active matter can produce non-vanishing currents in steady state. This also allows for exertion of non-zero forces or torques on objects immersed in a bath of active particles, a phenomenon that is impossible in a passive bath [85]. Facilitated by the rectification of active matter [86, 87], fabricated microscopic gears placed in bacterial baths rotate along the direction dictated by the orientation of the teeth [88, 37, 89]. It is thus possible to harvest useful mechanical work by conceiving engines fuelled by active particles [90]. Moreover, long-range currents sustained by the interplay of directed motion and interactions can be exploited to aid self-assembly of multiple passive objects immersed in an active bath [91].

To enable the rational design of immersed bodies that is optimized for a specific goal, it is imperative to formulate a theoretical framework that describes how active particles transmit forces to passive inclusions. In this chapter, we develop a theory that relates the net force/torque on an object to the particle current and the vorticity of the polarization. We verify its predictions with simulations of active Brownian particles.

4.1 Force on inclusions

Let us consider a dry, non-interacting active fluid with global number density $\bar{\rho}$. Its components are propelled with speed v_0. The evolution equation of the joint probability $\psi(\mathbf{r}, \varphi; t)$ is given by

$$\partial_t \psi = -\nabla \cdot \left[v_0 \mathbf{e} + \mu_0 \mathbf{F} - D_0 \nabla \right] \psi + D_\mathrm{r} \frac{\partial^2 \psi}{\partial \varphi^2} \tag{4.1}$$

where $\mathbf{e} \equiv (\cos\varphi, \sin\varphi)^T$ is the orientation vector which diffuses on the timescale given by D_r^{-1}. The bare mobility is related to the translational diffusion constant D_0 through $\mu_0 = D_0/(k_\mathrm{B}T)$ where T is the temperature and k_B is Boltzmann's constant. Since particles do not interact, the force $\mathbf{F}$ is completely determined by interactions with immersed objects.

Integrating eq. (4.1) over orientation φ, we get

$$\partial_t \rho = -\nabla \cdot [v_0 \mathbf{p} + \mu_0 \mathbf{F}\rho - D_0 \nabla\rho] \equiv -\nabla \cdot \mathbf{j} \tag{4.2}$$

with density $\rho = \int_0^{2\pi} \mathrm{d}\varphi\ \psi$, polarization density $\mathbf{p} = \int_0^{2\pi} \mathrm{d}\varphi\ \mathbf{e}\psi$ and current $\mathbf{j}$. Multiplying eq. (4.1) by $\mathbf{e}$ and integrating over φ, we get the evolution equation for the polarization density $\mathbf{p}$ to be

$$\partial_t \mathbf{p} = -\nabla \cdot \left[v_0 \left(\mathbf{Q} + \frac{1}{2}\rho \mathbf{1} \right) + \mu_0 \mathbf{F}\rho - D_0 \nabla \mathbf{p} \right] - D_\mathrm{r} \mathbf{p} \tag{4.3}$$

with nematic tensor $\mathbf{Q} = \int_0^{2\pi} \mathrm{d}\varphi\ \left(\mathbf{e} \otimes \mathbf{e} - \frac{1}{2}\mathbf{1} \right)$. The evolution of $\mathbf{Q}$, obtained by multiplying eq. (4.1) by $\left(\mathbf{e} \otimes \mathbf{e} - \frac{1}{2}\mathbf{1} \right)$ and integrating over φ, is governed by

$$\partial_t \mathbf{Q} = -v_0 \nabla \cdot \left(\mathbf{W} - \frac{1}{2}\mathbf{1} \otimes \mathbf{p} \right) - \mu_0 \nabla \cdot (\mathbf{F} \otimes \mathbf{Q}) + D_0 \nabla^2 \mathbf{Q} - 4 D_\mathrm{r} \mathbf{Q} \tag{4.4}$$

with $W_{ijk} \equiv \int_0^{2\pi} \mathrm{d}\varphi\ e_i e_j e_k \psi$. To close the hierarchy of orientational moments, we drop the derivatives of $\mathbf{Q}$ and neglect the third moment $\int_0^{2\pi} \mathrm{d}\varphi\ \left(e_i e_j e_k - \frac{3}{4}\delta_{ij} e_k \right) \psi = 0$. Up to these approximations, the nematic tensor is

$$\mathbf{Q} \approx -\frac{v_0}{16 D_\mathrm{r}} (\nabla \mathbf{p})^{ST} \tag{4.5}$$

where the symmetric and traceless gradient of the polarization $(\nabla \mathbf{p})_{ij}^{ST} = \partial_i p_j + \partial_j p_i - \partial_k p_k \delta_{ij}$. Plugging this expression in eq. (4.3) and considering steady state, we get

$$\mathbf{p} = \frac{\mu_0}{D_\mathrm{r}} \nabla \cdot \left[\frac{v_0}{2\mu_0} \rho \mathbf{1} + \frac{v_0}{\mu_0} \mathbf{Q} + \mathbf{F} \otimes \mathbf{p} - k_\mathrm{B} T (\nabla \mathbf{p})^{ST} \right] \equiv \frac{\mu_0}{v_0} \nabla \cdot \boldsymbol{\sigma}_A \tag{4.6}$$

with active stress

$$\boldsymbol{\sigma}_A = -\frac{v_0}{D_\mathrm{r}} \left[\frac{v_0}{2\mu_0} \rho \mathbf{1} + \frac{v_0}{\mu_0} \mathbf{Q} + \mathbf{F} \otimes \mathbf{p} - k_\mathrm{B} T (\nabla \mathbf{p})^{ST} \right]. \tag{4.7}$$

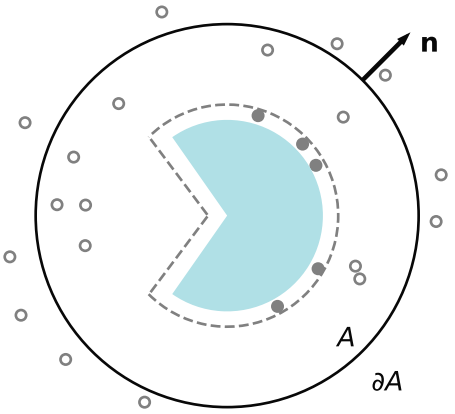

Figure 4.1: Sketch of a passive body surrounded by an ideal active fluid. Particles within the grey dashed boundary (filled circles) exert forces on the immersed object (blue wedge). The region outside the grey dashed boundary in which particles (unfilled circle) behave as isolated ABPs corresponds to the *force-free* region. To apply the divergence theorem, we consider a circular contour ∂A in the force-free region bounding an area A. The outward-pointing normal vector to ∂A is denoted by $\mathbf{n}$.

On rewriting eq. (4.2) in terms of the active stress, we obtain

$$\nabla \cdot \boldsymbol{\sigma} + \mathbf{F}\rho = \mathbf{j}/\mu_0 \tag{4.8}$$

where the total stress $\boldsymbol{\sigma} = \boldsymbol{\sigma}_A - k_\mathrm{B}T\rho\mathbf{1}$ has contributions from the active stress and translational diffusion.

To compute the force $\mathbf{F}_1$ on the immersed object, we invoke Newton's third law according to which

$$\mathbf{F}_1 = -\int \mathrm{d}^2\mathbf{r}\ \mathbf{F}\rho. \tag{4.9}$$

The presence of an inclusion separates the system into two regions: one where active particles experience non-zero forces and another in which forces due to interactions vanish. As shown in fig. 4.1, we now consider a circular contour ∂A in the force-free region and apply the divergence theorem to eq. (4.9) after plugging in eq. (4.8). The force $\mathbf{F}_1$ can be rewritten as

$$\mathbf{F}_1 = \oint_{\partial A} \mathrm{d}l\ \left[\mathbf{n}\cdot\boldsymbol{\sigma} - \frac{1}{\mu_0}(\mathbf{n}\cdot\mathbf{j})\mathbf{r}\right]. \tag{4.10}$$

Here we have used $\nabla \cdot \mathbf{j} = 0$, to write the current as $j_i = \partial_k(j_k x_i)$. The force $\mathbf{F}_1$ it thus determined by the stress tensor $\boldsymbol{\sigma}$ and the particle current $\mathbf{j}$. As long as the contour ∂A envelopes the object completely and is in the force-free region, it is arbitrary. To make analytical progress, we now place the boundary far away from the object.

Force-free, far-field regime

Let us now focus on the force-free region. Plugging $v_0\mathbf{p} = D_0\nabla\rho + \mathbf{j}$ [eq. (4.2)] in eq. (4.6), we get

$$-D_0\left(\nabla^2 - \xi^{-2}\right)\nabla\rho = \left(\nabla^2 - \ell^{-2}\right)\mathbf{j} \tag{4.11}$$

where

$$\ell = \sqrt{\frac{D_0}{D_\mathrm{r}}}\left(1 + \frac{\ell_\mathrm{p}^2 D_\mathrm{r}}{16 D_0}\right)^{1/2} \tag{4.12}$$

and

$$\xi = \ell\left(1 + \frac{\ell_\mathrm{p}^2 D_\mathrm{r}}{2D_0}\right)^{-1/2}. \tag{4.13}$$

Here $\ell_\mathrm{p} \equiv v_0/D_\mathrm{r}$ is the persistence length associated with the directed motion of particles.

For an object that does not generate currents, eq. (4.11) suggests that

$$\left(\nabla^2 - \xi^{-2}\right)\nabla\rho = 0. \tag{4.14}$$

The excess density decays exponentially, *i.e.*, $\rho - \rho_\infty \sim \mathrm{e}^{-r/\xi}$. On taking the divergence on both sides of eq. (4.11), we get

$$\left(\nabla^2 - \xi^{-2}\right)\nabla^2\rho = 0. \tag{4.15}$$

More generally, in the far-field, for $r \gg \xi$, we get

$$\nabla^2\rho^{\mathrm{ff}} = 0, \qquad \mathbf{j}^{\mathrm{ff}} = -D_{\mathrm{eff}}\nabla\rho^{\mathrm{ff}} \tag{4.16}$$

with effective diffusion constant $D_{\mathrm{eff}} \equiv D_0(\ell/\xi)^2$. All quantities in the far-field are indicated by the superscript 'ff'. Assuming that the second derivative of the polarization can be neglected in the far-field, eq. (4.6) and subsequently eq. (4.7) simplify to give

$$\mathbf{p}^{\mathrm{ff}} = -\frac{v_0}{2D_\mathrm{r}}\nabla\rho^{\mathrm{ff}}. \tag{4.17}$$

In terms of these two length scales, the stress tensor can be written as

$$\mu_0\boldsymbol{\sigma} = -D_{\mathrm{eff}}\rho\mathbf{1} + v_0\ell^2(\nabla\mathbf{p})^{ST}, \qquad \mu_0\boldsymbol{\sigma}^{\mathrm{ff}} = -D_{\mathrm{eff}}\rho^{\mathrm{ff}}\mathbf{1} - \frac{v_0^2\ell^2}{2D_\mathrm{r}}(\nabla\nabla\rho^{\mathrm{ff}})^{ST}. \tag{4.18}$$

The structure of eqs. (4.16) is identical to those seen in magnetostatics. To make the connection, note that the particle current $\mathbf{j}^{\text{ff}}$ is analogous to the field and the number density ρ^{ff} is analogous to the scalar potential. Using the two-dimensional cross product, the equivalent of Biot-Savart law becomes

$$\mathbf{j} = \frac{1}{2\pi} \int \mathrm{d}^2\mathbf{r}' \, \frac{\Omega(\mathbf{r}')\mathbf{e}_z \times (\mathbf{r} - \mathbf{r}')}{|\mathbf{r} - \mathbf{r}'|^2} \tag{4.19}$$

where the curl of the current

$$\Omega \equiv \nabla \times \mathbf{j} = \nabla \times (v_0 \mathbf{p} + \mu_0 \mathbf{F}\rho - D_0 \nabla\rho) \tag{4.20}$$

$$= v_0 \omega + \mu_0 \nabla \times (\mathbf{F}\rho). \tag{4.21}$$

Here, we have introduced the curl of the polarization $\omega \equiv \nabla \times \mathbf{p}$. In Cartesian coordinates, the current can be written as

$$j_i = -\frac{1}{2\pi} \varepsilon_{ij} \int \mathrm{d}^2\mathbf{r}' \, \frac{x_j - x_j'}{|\mathbf{r} - \mathbf{r}'|^2} \Omega(\mathbf{r}') \tag{4.22}$$

where ε_{ij} is the two-dimensional Levi-Civita symbol. For small $\mathbf{r}'$, the Taylor expansion about $\mathbf{r}$ is

$$\begin{aligned} \frac{x_j - x_j'}{|\mathbf{r} - \mathbf{r}'|^2} &\approx \frac{x_j}{r^2} + \left(\frac{\partial}{\partial x_k} \frac{x_j - x_j'}{|\mathbf{r} - \mathbf{r}'|^2} \right)_{\mathbf{r}'=0} x_k' \\ &= \frac{x_j}{r^2} - \left(\frac{\partial}{\partial x_k} \frac{x_j}{r^2} \right) x_k'. \end{aligned} \tag{4.23}$$

Substituting the expansion in eq. (4.22), we get

$$j_i^{\text{ff}} = -\frac{1}{2\pi} \varepsilon_{ij} \left(\frac{x_j}{r^2} \right) \tilde{Q} + \frac{1}{2\pi} \varepsilon_{ij} \left(\frac{\partial}{\partial x_k} \frac{x_j}{r^2} \right) \tilde{P}_k = \frac{1}{2\pi} \varepsilon_{ij} \frac{\partial}{\partial x_j} \frac{x_k \tilde{P}_k}{r^2} \tag{4.24}$$

where $\tilde{Q} = \int \mathrm{d}^2\mathbf{r} \; \Omega$ and $\tilde{\mathbf{P}} = \int \mathrm{d}^2\mathbf{r} \; \mathbf{r}\Omega$ are the first two moments of Ω. The absence of angular currents sets $\tilde{Q} = 0$. Since the term in the brackets is symmetric, we have exchanged indices in the last step. Introducing the current dipole moment $\mathbf{m} \equiv \boldsymbol{\varepsilon} \cdot \tilde{\mathbf{P}}$, we have

$$m_i = v_0 \varepsilon_{ij} P_j + \mu_0 \varepsilon_{ij} \int \mathrm{d}^2\mathbf{r} \; x_j \varepsilon_{kl} \frac{\partial}{\partial x_k} (F_l \rho) \tag{4.25}$$

where $\mathbf{P} = \int \mathrm{d}^2\mathbf{r}\ \mathbf{r}\omega$ is the vorticity dipole moment. Performing partial integration and using the divergence theorem keeping the boundary of the integral in the free region, we get

$$m_i = v_0 \varepsilon_{ij} P_j - \mu_0 \varepsilon_{ij}\varepsilon_{jl} \int \mathrm{d}^2\mathbf{r}\ F_l \rho. \tag{4.26}$$

Identifying the integral in the second term as $-\mathbf{F}_1$ and using $\varepsilon_{ij}\varepsilon_{jl} = -\delta_{il}$, we have

$$\mathbf{m} = v_0 \boldsymbol{\varepsilon} \cdot \mathbf{P} - \mu_0 \mathbf{F}_1. \tag{4.27}$$

We find that the force on the object $\mathbf{F}_1$ has two contributions: the current dipole moment $\mathbf{m}$ and the vorticity dipole moment $\mathbf{P}$. In terms of $\mathbf{m}$, the density in the far-field is

$$\rho^{\mathrm{ff}} = \rho_\infty + \frac{1}{D_{\mathrm{eff}}} \frac{\mathbf{m}\cdot\mathbf{r}}{2\pi r^2}. \tag{4.28}$$

Unbound system

We now consider an unbound system. Consider a circular contour ∂A of radius r bounding a region of area A. The vorticity dipole moment is given by

$$P_k = \int \mathrm{d}^2\mathbf{r}\ x_k \varepsilon_{ij} \partial_i p_j = \varepsilon_{ij} \int \mathrm{d}^2\mathbf{r}\ [\partial_i (x_k p_j) - p_j \partial_i x_k]. \tag{4.29}$$

Substituting eq. (4.6) and thereafter applying the divergence theorem, we get

$$\mathbf{P}(A) = \oint_{\partial A} \mathrm{d}l\ \left[(\mathbf{n}\times\mathbf{p})\mathbf{r} - \frac{\mu_0}{v_0} \boldsymbol{\varepsilon} \cdot (\mathbf{n}\cdot\boldsymbol{\sigma}_A) \right] \tag{4.30}$$

where $\mathbf{n}$ is the vector normal to the contour. Placing the boundary far away from the body and inserting the far-field expressions for the polarization and stress tensor [see eq. (4.17)], we get

$$P_k(A) = -\frac{v_0}{2D_{\mathrm{r}}} \oint_{\partial A} \mathrm{d}l\ [x_k (\mathbf{n}\times\nabla\rho^{\mathrm{ff}}) - \varepsilon_{kj} n_j \rho^{\mathrm{ff}}]. \tag{4.31}$$

With $\mathbf{n} = \mathbf{e}_r$, the cross product evaluates to

$$\mathbf{n}\times\nabla\rho^{\mathrm{ff}} = \mathbf{e}_r \times \left[\frac{\partial\rho^{\mathrm{ff}}}{\partial r}\mathbf{e}_r + \frac{1}{r}\frac{\partial\rho^{\mathrm{ff}}}{\partial\theta}\mathbf{e}_\theta \right] = \frac{1}{r}\frac{\partial\rho^{\mathrm{ff}}}{\partial\theta}. \tag{4.32}$$

Here we have written the gradient in polar coordinates. Plugging this in eq. (4.31) and using $\boldsymbol{\varepsilon}\cdot\mathbf{e}_r = -\mathbf{e}_\theta$, we get the vorticity dipole moment in an unbound system to be

$$\mathbf{P}_{\text{unb}} = -\frac{v_0}{2D_{\text{r}}}\oint_{\partial A}\mathrm{d}l\,\left[\frac{\partial\rho^{\text{ff}}}{\partial\theta}\mathbf{e}_r + \rho^{\text{ff}}\mathbf{e}_\theta\right] = 0. \tag{4.33}$$

We thus find that the vorticity dipole moment vanishes in an unbound system. To calculate the force on the object, we need the divergence of the stress in the far-field [eq. (4.17)]. This involves

$$\mathbf{e}_r\cdot(\nabla\nabla\rho^{\text{ff}})^{ST} = \left(2\frac{\partial^2\rho^{\text{ff}}}{\partial r^2} - \nabla^2\rho^{\text{ff}}\right)\mathbf{e}_r + \frac{2}{r}\left(\frac{\partial^2\rho^{\text{ff}}}{\partial r\partial\theta} - \frac{1}{r}\frac{\partial\rho^{\text{ff}}}{\partial\theta}\right)\mathbf{e}_\theta. \tag{4.34}$$

Plugging eq. (4.28) in eq. (4.34), we get

$$\mathbf{e}_r\cdot(\nabla\nabla\rho^{\text{ff}})^{ST} = \frac{m}{D_{\text{eff}}}\frac{2}{\pi r^3}(\cos\theta\mathbf{e}_r + \sin\theta\mathbf{e}_\theta) \tag{4.35}$$

with $\mathbf{m} = m\mathbf{e}_x$. The integral of this term along a circular contour vanishes and the only non-zero contribution from the stress is from the far-field density. The integral over stress

$$\oint_{\partial A}\mathrm{d}l\;\mathbf{n}\cdot\boldsymbol{\sigma} = -\frac{D_{\text{eff}}}{\mu_0}\oint_{\partial A}\mathrm{d}l\;\delta\rho^{\text{ff}}\mathbf{e}_r = -\frac{\mathbf{m}}{2\mu_0}. \tag{4.36}$$

To calculate the contribution of the current to $\mathbf{F}_1$, we insert eq. (4.16) and eq. (4.28) in $-\frac{1}{\mu_0}\oint_{\partial A}\mathrm{d}l\;(\mathbf{n}\cdot\mathbf{j})\mathbf{r}$ to get

$$\frac{D_{\text{eff}}}{\mu_0}\oint_{\partial A}\mathrm{d}l\;(\mathbf{r}\cdot\nabla\rho^{\text{ff}})\mathbf{e}_r = -\frac{1}{2\pi\mu_0}\oint_{\partial A}\mathrm{d}l\;r_k\partial_k\left(\frac{m_i r_i}{r^2}\right)\mathbf{e}_r = -\frac{\mathbf{m}}{2\mu_0}. \tag{4.37}$$

Summing up the contributions from the stress [eq. (4.36)] and current [eq. (4.37)], we find that the net force on the object $\mathbf{F}_1$ [eq. (4.10)] in an unbound system is

$$\mathbf{F}_1 = -\mathbf{m}/\mu_0, \tag{4.38}$$

in agreement with Ref. [91]. In an unbound system, the force is thus completely determined by the current dipole moment.

4.1.1 Boomerang in an ideal active fluid

To put our theory to test, we turn to Brownian dynamics simulations. We consider an $L\times L$ system of $N = \bar{\rho}L^2$ non-interacting ABPs and set the global number density

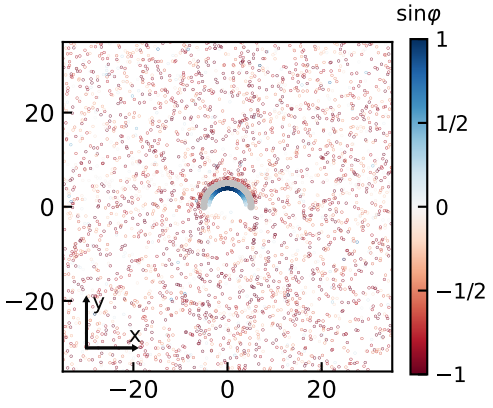

Figure 4.2: Typical snapshot of a system comprising of a boomerang (grey) surrounded by active Brownian particles which interact with it. ABPs are colored according to the sine of the angle their orientation vectors make with the positive x axis. Evidently, particles that accumulate on the inner surface are strongly polarized along the positive y axis while those in the bulk are polarized along the opposite direction.

$\bar{\rho} = 1.2$ unless explicitly mentioned otherwise. We include a boomerang-shaped object constructed from fixed, equidistant points on a semicircle of radius $R = 5$. Figure 4.2 shows a representative snapshot of the system.

The ABPs interact with each of these points through the repulsive WCA potential defined in eq. (2.54). We measure lengths in units of the potential's length scale σ, energy in units of $k_{\mathrm{B}}T$ and time in units of σ^2/D_0. In reduced units, we set the energy scale of the potential $\varepsilon_0 = 100$ and $D_{\mathrm{r}} = 3$. The evolution of the position $\mathbf{r}_i$ and orientation φ_i of the ith particle is governed by eqs. (2.23). We integrate the equations of motion with a time step $\delta t = 10^{-5}$. All results are obtained by averaging over five independent simulation runs.

In fig. 4.3 (a), we plot a two-dimensional histogram of the density and polarization of particles around the boomerang. We see that particles accumulate at the surface of the obstacle, akin to several previous reports of aggregation of ABPs on surfaces [92, 93, 94]. Moreover, as can also be seen in fig. 4.2, particles away from the boomerang are polarized downward. Larger residence time of particles below the boomerang compared to those above prompts the downward orientation of particles despite the absence of explicit aligning interactions. The manifestly antisymmetric vorticity field shown in fig. 4.3(b) indicates a non-zero vorticity dipole moment $\mathbf{P}$ that points along $\mathbf{e}_x$. This is in contradiction to eq. (4.33) that suggests a vanishing vorticity dipole moment $\mathbf{P}_{\mathrm{unb}} = 0$ in an unbound system. The result that the force is determined by the current dipole moment [eq. (4.38)] can thus not be validated. Since we perform

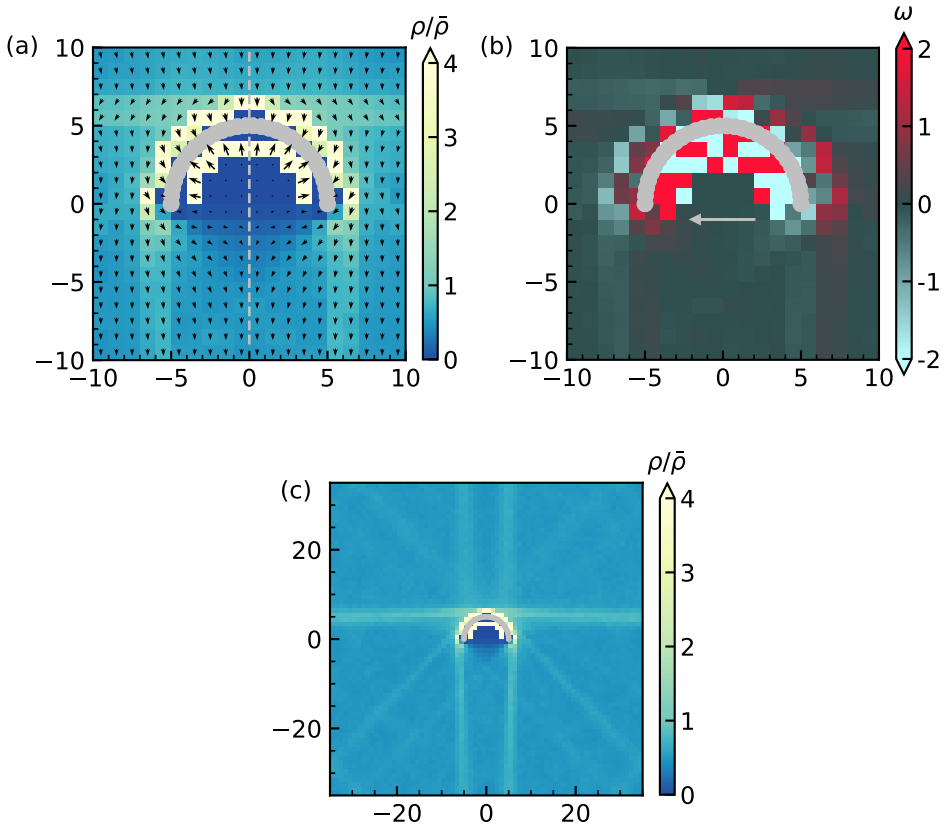

Figure 4.3.: (a) Zoomed-in plot of the normalized density $\rho/\bar{\rho}$ and polarization $\mathbf{p}$ of ABPs with $\bar{\rho} = 1.2$ and $v_0 = 80$. The length of the arrows denoting the magnitude of polarization is plotted on a logarithmic scale. The line of symmetry is denoted by the dashed grey line. (b) Heatmap of vorticity ω around the boomerang. The grey arrow indicates the direction of vorticity dipole moment $\mathbf{P}$. (c) Density map of the whole system for the parameters shown in (a).

simulations with periodic boundary conditions [see section 2.2.3 for details], we now reformulate the theory for this case.

Force in a periodic system

To incorporate periodic boundaries, let us assume a two-dimensional lattice of dipoles. In appendix A.2, we show that this candid assumption does not modify the density, which is still given by eq. (4.28). Figure 4.3 (c) shows a stark deviation from a dipolar field with visible “streaks” in the density field that connect through the periodic boundaries.

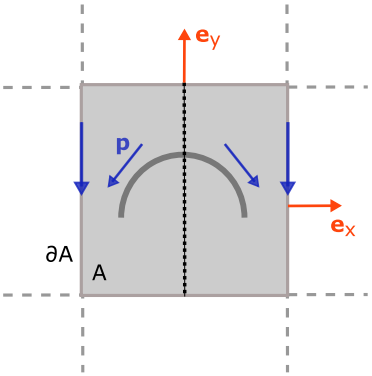

Figure 4.4: Sketch of the system with periodic boundaries. The boomerang is symmetric about the dotted black line running through the center. We focus on a specific square domain of area A bounded by the counter ∂A. The polarization of particles $\mathbf{p}$ is outlined by blue arrows and the vectors normal to ∂A are indicated by red arrows.

We now revisit eq. (4.10) and compute the stress tensor and current for a periodic system. We place the boomerang at the origin. Its line symmetric shape [cf. fig. 4.4] imposes the following symmetries on the density and polarization:

$$\begin{aligned} \rho(-x,y) &= \rho(x,y), \\ p_x(-x,y) &= -p_x(x,y), \\ p_y(-x,y) &= p_y(x,y). \end{aligned} \tag{4.39}$$

To compute the contribution of the stress tensor given in eq. (4.18), we need[1]

$$\mu_0 \mathbf{n}\cdot\boldsymbol{\sigma} = -D_{\text{eff}}\rho\mathbf{n} + v_0\ell^2\left[\nabla(\mathbf{n}\cdot\mathbf{p}) - \boldsymbol{\varepsilon}\cdot\nabla(\mathbf{n}\times\mathbf{p})\right]. \tag{4.40}$$

We integrate piecewise along the contour ∂A pictured in fig. 4.4

$$\begin{aligned} \mu_0 \oint_{\partial A} \mathrm{d}l\ \mathbf{n}\cdot\boldsymbol{\sigma} = \mu_0 \underbrace{\int_{-\frac{L}{2}}^{\frac{L}{2}} \mathrm{d}y\ \mathbf{e}_x\cdot\boldsymbol{\sigma}}_{\text{right}} + \mu_0 \underbrace{\int_{-\frac{L}{2}}^{\frac{L}{2}} \mathrm{d}y\ (-\mathbf{e}_x)\cdot\boldsymbol{\sigma}}_{\text{left}} \\ + \mu_0 \underbrace{\int_{-\frac{L}{2}}^{\frac{L}{2}} \mathrm{d}x\ \mathbf{e}_y\cdot\boldsymbol{\sigma}}_{\text{top}} + \mu_0 \underbrace{\int_{-\frac{L}{2}}^{\frac{L}{2}} \mathrm{d}x\ (-\mathbf{e}_y)\cdot\boldsymbol{\sigma}}_{\text{bottom}}. \end{aligned} \tag{4.41}$$

The term involving the density integrates to zero since the top-bottom and left-right chunks of the integral cancel each other out. The contribution of the polarization [second term in eq. (4.40)] along the top boundary reads

$$S_{\text{top}} = v_0\ell^2 \int_{-\frac{L}{2}}^{\frac{L}{2}} \mathrm{d}x\ [\nabla p_y + \boldsymbol{\varepsilon}\cdot\nabla p_x] = \partial_y \int_{-\frac{L}{2}}^{\frac{L}{2}} \mathrm{d}x\ v_0\ell^2\mathbf{p} = G\mathbf{e}_y. \tag{4.42}$$

[1] $[\mathbf{n}\cdot(\nabla\mathbf{p})^{ST}]_j = n_i\partial_i p_j + n_i\partial_j p_i - n_i\partial_k p_k\delta_{ij} = \delta_j p_i n_i + \varepsilon_{ji}\varepsilon_{kl}n_k\partial_i p_l$

The line symmetry of the boomerang sets the x component to zero. Using $v_0 p_y = D_0 \partial_y \rho + j_y$, we define

$$G \equiv D_0 \int_{-\frac{L}{2}}^{\frac{L}{2}} \mathrm{d}x \;\; \partial_y^2 \rho \Big|_{y=\frac{L}{2}} + \partial_y \int_{-\frac{L}{2}}^{\frac{L}{2}} \mathrm{d}x \; j_y(x,y). \tag{4.43}$$

To estimate the second term, we call upon the vanishing divergence of the current. Symmetry stipulates $j_x\left(\pm\frac{L}{2}, y\right) = 0$ and measurements from simulations shown in fig. 4.5 (a) fluctuates about zero attesting to the vanishing x component. Additionally, with $\nabla \cdot \mathbf{j} = 0$, we have

$$\int_{-\frac{L}{2}}^{\frac{L}{2}} \mathrm{d}x \; \nabla \cdot \mathbf{j} = \int_{-\frac{L}{2}}^{\frac{L}{2}} \mathrm{d}x \; (\partial_x j_x + \partial_y j_y) = \partial_y J_L = 0 \tag{4.44}$$

where the integrated current

$$J_L \equiv \int_{-\frac{L}{2}}^{\frac{L}{2}} \mathrm{d}x \; j_y(x,y). \tag{4.45}$$

This implies that j_y is independent of y and is in agreement with simulations [cf. fig. 4.5 (b)]. The expression in eq. (4.43) thus reduces to

$$G = D_0 \int_{-\frac{L}{2}}^{\frac{L}{2}} \mathrm{d}x \;\; \partial_y^2 \rho \Big|_{y=\frac{L}{2}} . \tag{4.46}$$

The contribution from the lower boundary with normal vector $\mathbf{n} = -\mathbf{e}_y$ yields $-S_{\text{top}}$. Examining the integral over the right boundary with normal vector $\mathbf{n} = \mathbf{e}_x$, with $p_x = \left(\pm\frac{L}{2}, y\right) = 0$ and $\partial_x p_y = 0$, we have

$$v_0 \ell^2 \int_{-\frac{L}{2}}^{\frac{L}{2}} \mathrm{d}y \; [\nabla p_x - \boldsymbol{\varepsilon} \cdot \nabla p_y] = \partial_x \int_{-\frac{L}{2}}^{\frac{L}{2}} \mathrm{d}y \; v_0 \ell^2 \mathbf{p} = 0. \tag{4.47}$$

On gathering all terms we find that the integral over the stress $\oint_{\partial A} \mathrm{d}l \; \mathbf{n} \cdot \boldsymbol{\sigma}$ vanishes therewith implying that, in contrast to an unbound system, the stress tensor does not contribute to the force $\mathbf{F}_1$ on the immersed object in a periodic system. The force in a periodic system is thus sustained by the current J_L through the boundary.

The contribution of the current $\mathbf{j}$ to the force is given by

$$\oint_{\partial A} \mathrm{d}l \; (\mathbf{n} \cdot \mathbf{j})\mathbf{r} = \int_{-\frac{L}{2}}^{\frac{L}{2}} \mathrm{d}x \;\; \left[j_y\left(x, -\frac{L}{2}\right) \frac{L}{2} + j_y\left(x, \frac{L}{2}\right) \frac{L}{2} \right] \mathbf{e}_y = L J_L \mathbf{e}_y. \tag{4.48}$$

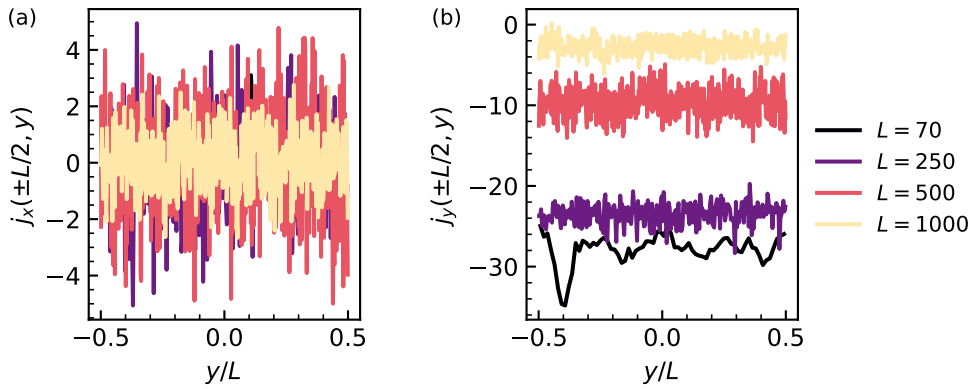

Figure 4.5.: Current through the cross-section at $x = \pm L/2$. The (a) x component and (b) y component of the current is plotted for different box lengths L.

The contributions from the right and left boundaries with normal vectors $\mathbf{e}_x$ and $-\mathbf{e}_x$ again drop out. Moreover, since $j_y(-x) = j_y(x)$, the x component of the force vanishes. Combining eqs. (4.48) and (4.10), we find that the net force on the object $\mathbf{F}_1$ in a periodic system is given by

$$\mathbf{F}_1 = F_L \mathbf{e}_y = -\frac{1}{\mu_0} L J_L \mathbf{e}_y. \tag{4.49}$$

Employing the divergence theorem, the vorticity dipole moment can be written as

$$\mathbf{P} = \int \mathrm{d}^2\mathbf{r}\, (\nabla \times \mathbf{p})\mathbf{r} = \oint_{\partial_A} \mathrm{d}l\, (\mathbf{n} \times \mathbf{p})\mathbf{r}. \tag{4.50}$$

In the last step we have used the fact that the total polarization in the system is zero[2]. Plugging in $v_0\mathbf{p} = D_0\nabla\rho + \mathbf{j}$, we get

$$v_0\mathbf{P} = \oint_{\partial_A} \mathrm{d}l\, (\mathbf{n} \times [D_0\nabla\rho + \mathbf{j}])\mathbf{r}. \tag{4.51}$$

Since the curl of a gradient is zero, the density does not contribute and the calculation of $\mathbf{P}$ reduces to

$$v_0\mathbf{P}_L = \int_{-\frac{L}{2}}^{\frac{L}{2}} \mathrm{d}y\, \left[j_y\left(-\frac{L}{2}, y\right)\frac{L}{2} + j_y\left(\frac{L}{2}, y\right)\frac{L}{2} \right] \mathbf{e}_x = L^2 j_0 \mathbf{e}_x \equiv P_L \mathbf{e}_x. \tag{4.52}$$

Here we have defined the constant current through the left/right boundaries $j_y\left(\pm\frac{L}{2}, y\right) = j_0$. This is related to the integrated current through $Lj_0 = J_L$. Theory

[2] $\int \mathrm{d}^2\mathbf{r}\, \mathbf{p} = 0$.

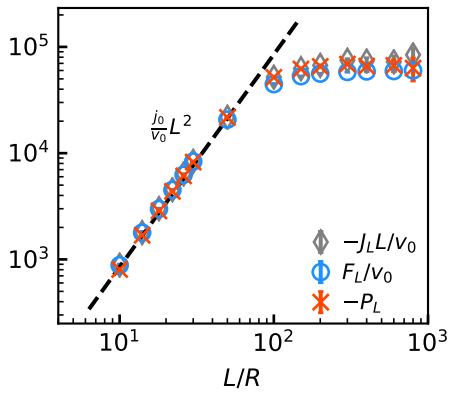

Figure 4.6: Numerically obtained integrated current $-J_L L/v_0$, force F_L/v_0 and vorticity dipole moment $-P_L$ for varying system sizes L. In agreement with theory [eq. (4.53)], all three quantities conform and scale as L^2 for system sizes up to L^*. Beyond $L^* \simeq 50R$, they plateau. The dashed line corresponds to $\frac{j_0}{v_0}L^2$. The propulsion speed set to $v_0 = 160$.

thus suggests that, in a periodic system, the force $\mathbf{F}_1$, vorticity dipole moment $\mathbf{P}$ and the boundary current are dependent on system size L. Comparing eqs. (4.52) and (4.49), we find that these three quantities are related through

$$-P_L = \frac{F_L}{v_0} = -\frac{J_L L}{v_0}. \tag{4.53}$$

To verify this equivalence, we perform simulations for different box lengths L keeping all other parameters fixed. We compute a two-dimensional histogram of the polarization and density. The gradient of the density is calculated using the scheme of central differences[3] and the integrated current J_L is subsequently obtained using the relation $v_0\mathbf{p} = D_0\nabla\rho + \mathbf{j}$ at $x = \pm\frac{L}{2}$ corresponding to the right and left boundaries.

In fig. 4.6, we show that eq. (4.53) indeed holds. We also observe that for small system sizes the force scales as L^2 and beyond a threshold L^*, it saturates to a constant value. The integrated current $J_L = j_0 L$ for $L < L^*$ and decreases as $\sim 1/L$ for larger systems. To qualitatively understand this scaling, we recognize that the current is generated by the difference in densities of ABPs above and below the boomerang evident in fig. 4.3. With dimensionless gradient $\alpha_L > 0$, eq. (4.16) advocates

$$J_L = -D_{\text{eff}}\alpha_L\bar{\rho}. \tag{4.54}$$

The streamlines that connect through the periodic boundaries [see fig. 4.3] become more numerous as L increases leading to a larger integrated current $J_L \propto \alpha \propto L/\ell$.

[3]With mesh spacing h, the derivative of a function is given by $f'(x) = \frac{1}{2h}[f(x+h) - f(x-h)]$.

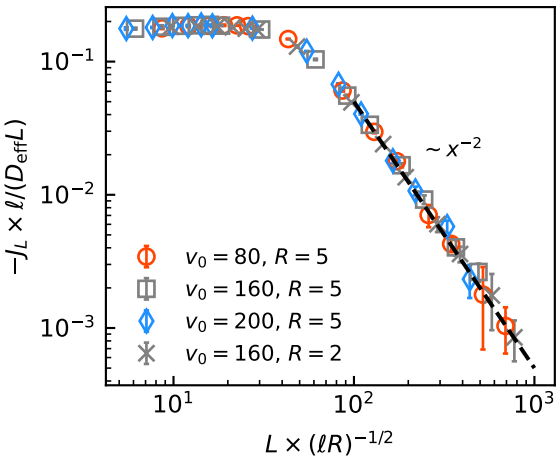

Figure 4.7: Scaled integrated current $-J_L\ell/(D_{\text{eff}}L)$ as a function of scaled system size $L/\sqrt{\ell R}$ for different propulsion speeds $v_0 = \{80, 160, 200\}$ and radii of boomerang $R = \{2, 5\}$. The data collapses on appropriate scaling. The dashed black line corresponds to $f(x) \sim 1/x^2$.

For $L > L^*$, we anticipate the dimensionless gradient $\alpha_L \propto R/L$ to be self-similar lowering the current along the boundary. The integrated current can be written as

$$J_L = -\bar{\rho}D_{\text{eff}}\frac{L}{\ell}f(L/\sqrt{\ell R}) \sim \bar{\rho}D_{\text{eff}}\begin{cases} L/\ell & (L \ll L^*) \\ R/L & (L \gg L^*) \end{cases} \tag{4.55}$$

assuming that α_L only enters through the non-dimensional factor $L/\sqrt{\ell R}$. The scaling function $f(x)$ is constant for small x and drops as $f(x) \sim 1/x^2$ for large x. The collapse of numerical data shown in fig. 4.7 validates this form for the scaling of the current. The crossover at L^* implies the presence of an optimal spacing between inclusions that maximizes forces and currents. Moreover, since the current dipole moment $\mathbf{m} = v_0\boldsymbol{\varepsilon}\cdot\mathbf{P} - \mu_0\mathbf{F}_1 = -(v_0P_L + \mu_0F_L)\mathbf{e}_y = 0$ vanishes, in periodic systems, the idea of treating immersed objects as current dipoles is unfounded.

4.2 Torque on inclusions

In addition to forces, contingent on its shape, an object immersed in an active fluid may also experience a net torque. Using eq. (4.10), the net torque τ_1 on an immersed object is given by

$$\tau_1 = -\int_A \mathrm{d}^2\mathbf{r}\ \mathbf{r}\times\mathbf{F}\rho \tag{4.56}$$

$$= \int_A \mathrm{d}^2\mathbf{r}\ \mathbf{r}\times\left[\nabla\cdot\boldsymbol{\sigma} - \frac{1}{\mu_0}\mathbf{j}\right]. \tag{4.57}$$

The first term simplifies to

$$\mathbf{r} \times (\nabla \cdot \boldsymbol{\sigma}) = \varepsilon_{ij} x_i \partial_k \sigma_{kj} = \varepsilon_{ij} \left[\partial_k (x_i \sigma_{kj}) - \sigma_{ij}\right] = \varepsilon_{ij} \partial_k (x_i \sigma_{kj}). \tag{4.58}$$

Since σ_{ij} is symmetric [see eq. (4.18)], $\varepsilon_{ij}\sigma_{ij} = 0$. Employing the divergence theorem and inserting eq. (4.18) after substituting $v_0(\nabla \mathbf{p})^{ST} = (\nabla \mathbf{j})^{ST} - D_0(\nabla\nabla\rho)^{ST}$, the integral over the stress reduces to

$$\begin{aligned}\oint_{\partial A} \mathrm{d}l\ \varepsilon_{ij} x_i n_k \sigma_{kj} &= \int_0^{2\pi} \mathrm{d}\theta\ r\mathbf{e}_r \times (\mathbf{e}_r \cdot \boldsymbol{\sigma}) \\ &= -D_{\text{eff}} \int_0^{2\pi} \mathrm{d}\theta\ r\mathbf{e}_r \times (\rho \mathbf{e}_r) + k_{\text{B}} T \ell^2 \int_0^{2\pi} \mathrm{d}\theta\ r\mathbf{e}_r \times \mathbf{e}_r \cdot (\nabla\nabla\rho)^{ST} \\ &\quad + \frac{\ell}{\mu_0^2} \int_0^{2\pi} \mathrm{d}\theta\ r\mathbf{r} \times \mathbf{n} \cdot [\nabla \mathbf{j} + (\nabla \mathbf{j})^T - (\nabla \cdot \mathbf{j})\mathbf{1}]. \end{aligned} \tag{4.59}$$

Here we have used a circular boundary ∂A of radius r with normal vector $\mathbf{n} = \mathbf{e}_r$. The first term vanishes because $\mathbf{e}_r \times \mathbf{e}_r = 0$. On plugging in eq. (4.34), we find that the second term involving the integral

$$\int_0^{2\pi} \mathrm{d}\theta\ r \left(\frac{\partial^2 \rho}{\partial r \partial \theta} - \frac{1}{r} \frac{\partial \rho}{\partial \theta} \right) = 0 \tag{4.60}$$

also vanishes since density is periodic in θ. Using $\varepsilon_{ij} x_i n_k \partial_k j_j = n_k \partial_k (\varepsilon_{ij} x_i j_j) - \varepsilon_{ij} n_i j_j$, the torque defined in eq. (4.57) becomes

$$\tau_1 = \frac{\ell^2}{\mu_0} \int_0^{2\pi} \mathrm{d}\theta\ r[\mathbf{n} \cdot \nabla(\mathbf{r} \times \mathbf{j}) + (\mathbf{r} \times \nabla)\mathbf{n} \cdot \mathbf{j} - \mathbf{n} \times \mathbf{j}] - \frac{1}{\mu_0} \int_A \mathrm{d}^2\mathbf{r}\ \mathbf{r} \times \mathbf{j}. \tag{4.61}$$

Performing a multipole expansion of the current $\mathbf{j}$ up to the dipole contribution, in the force-free region,

$$\mathbf{j}(\mathbf{r}) = \frac{v_0}{2\pi} \left[\frac{Q}{r} \mathbf{e}_\theta + \frac{-\mathbf{R} \cdot \mathbf{P} + 2(\mathbf{e}_r \cdot \mathbf{P})\mathbf{e}_\theta}{r^2} \right] \tag{4.62}$$

where the vorticity monopole $Q = \int \mathrm{d}^2\mathbf{r}\ \omega$ and the vorticity dipole moment $\mathbf{P} = \int \mathrm{d}^2\mathbf{r}\ \mathbf{r}\omega$. Taking the cross product, we get

$$\mathbf{r} \times \mathbf{j} = \frac{v_0}{2\pi} \left[Q + \frac{\mathbf{e}_r \cdot \mathbf{P}}{r} \right] \tag{4.63}$$

Inserting the cross product in eq. (4.61), the only remaining integrals are of the form

$$\int_0^{2\pi} \mathrm{d}\theta\ \mathbf{r} \times \mathbf{j} = \int_0^{2\pi} \mathrm{d}\theta\ r j_\theta = v_0 Q. \tag{4.64}$$

Hence, $\tau_1 \propto v_0 Q$. Since $Q = 0$, the torque on the object τ_1 vanishes in an unbound system.

4.2.1 Duck in an ideal active fluid

We now perform simulations of a 'duck', a two-fold rotationally symmetric object, immersed in an ideal active fluid. It is constructed by cutting a circle along an arbitrary diameter and displacing the resulting semicircles along the same diameter. We employ periodic boundary conditions.

Figure 4.8 shows the density and vorticity heatmaps. Due to their finite persistence, there is an increased density of ABPs on the surface of the duck similar to what is also seen on the boomerang [cf. fig. 4.3]. The vorticity heatmap shows the emergence of two vorticity dipoles close to the surface. Due to symmetry, these two dipoles are of the same magnitude but point along opposite directions. The vorticity field, like the shape of the duck, exhibits two-fold rotational symmetry and decays rapidly away from the duck.

As expected, we measure a vanishing vorticity monopole Q in simulations. Despite this, we find that the torque on the duck is non-zero. Because the polarization has to be periodic in the system size, the vorticity monopole $Q = \oint_{\partial A} \mathrm{d}\mathbf{l} \cdot \mathbf{p} = 0$ vanishes even in periodic systems. At first glance, there appears to be a contradiction between theory and what is observed in simulations. An assembly of n vorticity dipoles at $\{\mathbf{r}_1, \ldots, \mathbf{r}_n\}$, however, also produces a torque given by[4]

$$\tau_1 = \sum_n \mathbf{r}_n \times \mathbf{F}_n = \frac{v_0}{\mu_0} \sum_n \mathbf{r}_n \times (\boldsymbol{\varepsilon} \cdot \mathbf{P}_n) = -\frac{v_0}{\mu_0} \sum_n \mathbf{r}_n \cdot \mathbf{P}_n. \tag{4.65}$$

In the last step, we have used $\varepsilon_{ij}\varepsilon_{jk} = -\delta_{ik}$. Since $P_n \sim L^2$ [cf. fig. 4.6], the torque in finite systems with periodic boundaries $\tau_1 \sim v_0 L^2$. We perform simulations for different propulsion speeds and system sizes, and plot the torque we measure in fig. 4.8. The torque indeed increases linearly with v_0. For $L < L^*$, we find the expected quadratic scaling of the torque with system size.

[4] In an unbound system, the force is generated by current dipoles; thereby, the torque in a periodic system τ_1 is expected to arise from n current dipoles. However, along the lines of what we show in appendix A.2, this naive perspective is inaccurate.

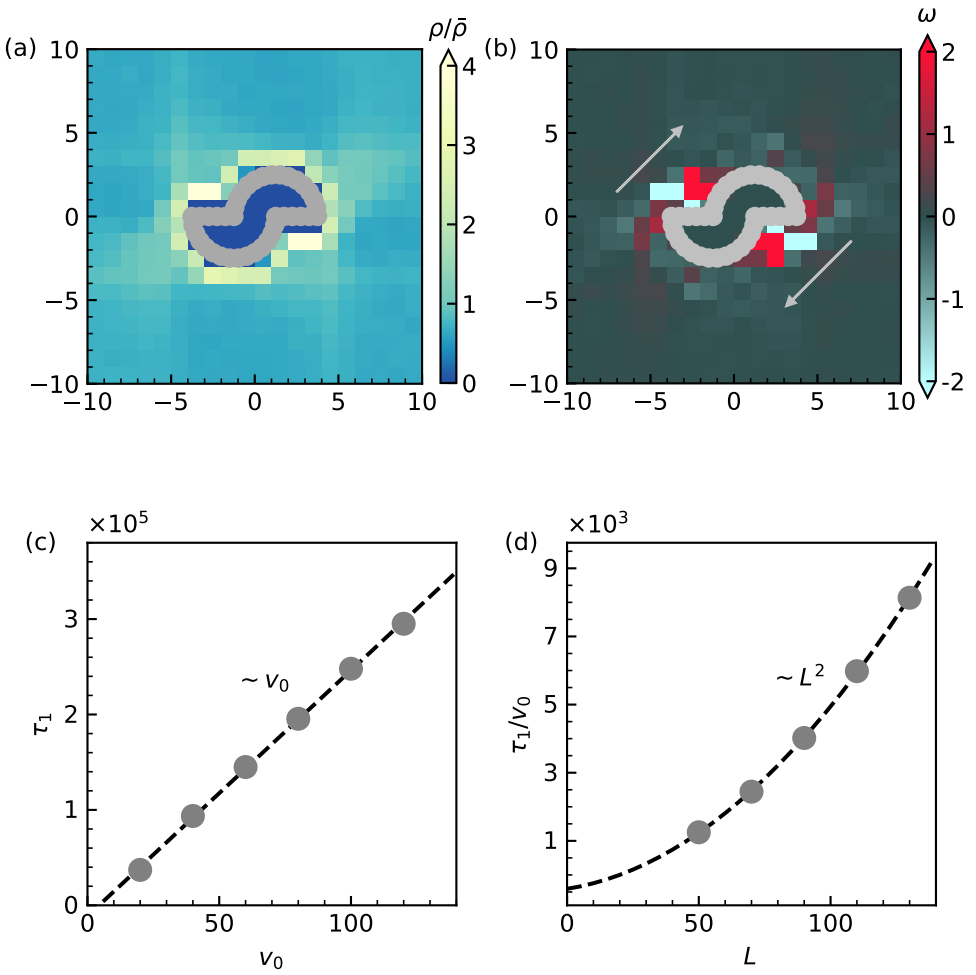

Figure 4.8.: Zoomed-in profiles of (a) normalized density $\rho/\bar{\rho}$ and (b) vorticity ω around the duck. Local dipoles pointing along the directions shown with grey arrows emerge. (c) Scaling of torque as a function of propulsion speed v_0. The dashed line shows a linear fit. (d) Scaling of torque (normalized by speed) as a function of system size L. The dashed line is a quadratic fit to the data.

4.3 Effect of shape on vorticity

To gain a qualitative understanding of how the design of the inclusion affects the resulting vorticity field, we consider three different shapes: (1) 'lune': a moon-shaped object constructed by chopping off a small disc of radius $R_s = 2.5$ from a complete circle, (2) 'bud': constructed by adding a small disc of radius $R_s = 2.5$ to a complete circle and (3) duck (introduced earlier).

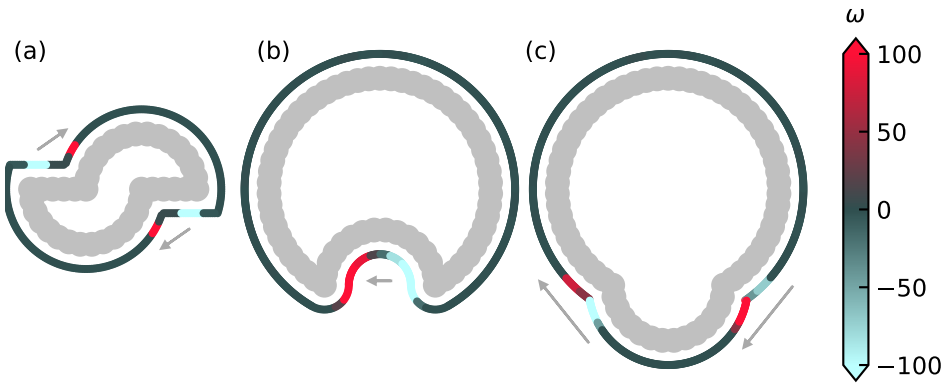

Figure 4.9.: Vorticity around the (a) duck, (b) lune and (c) bud. The grey arrows indicate the direction of emergent vorticity dipoles.

In fig. 4.9 we plot the vorticity along the surface of each shape slightly away from the interaction zone. The vorticity ω is visibly larger close to regions where there is a stark change in curvature. Outside these regions, the vorticity is approximately zero.

5 Force generation in confined active fluids

In the early 1950s, amongst many other experimental reports in traditionally unrelated fields, following are three observations that warranted a phenomenological understanding [95]:

- Red blood cells agglomerate in the presence of different types of macromolecules [96, 97]. This did not appear to specifically rely on the adsorption of macromolecules.
- When added to a soil suspension, polysaccharides promote the formation of water-stable soil 'crumbs' [98].
- Latex particles coagulate in the presence of polymers [99].

Asakura and Oosawa, in their seminal article[1], developed a theory of what is now commonly called *depletion interactions* [100]. Within this paradigm, they solved the contemporary puzzle of several 'species' flocculating by identifying a non-uniform osmotic pressure around them in the presence of (non-)adsorbing macromolecules [101]. Ever since, the mutually attractive force between large solvated particles in a solution with much smaller cosolutes ("depletants") has been extensively studied both theoretically [102, 103, 104] and experimentally [105, 106]. As outlined in fig. 5.1, steric hinderance prevents depletants from occupying the space between the larger colloids making it entropically favorable for these colloids to be closer to each other. This effect also renders itself as an attractive interaction between a colloid and a wall. The concentration of polymers determine the strength of attraction while the range depends on their radius of gyration. Depletion interactions have been exploited for applications like thickening of dairy products [107, 108], the principle reason for which is suggested to be the self-assembly of casein micelles induced by dispersed polysaccharides.

[1] The paper is a one-pager!

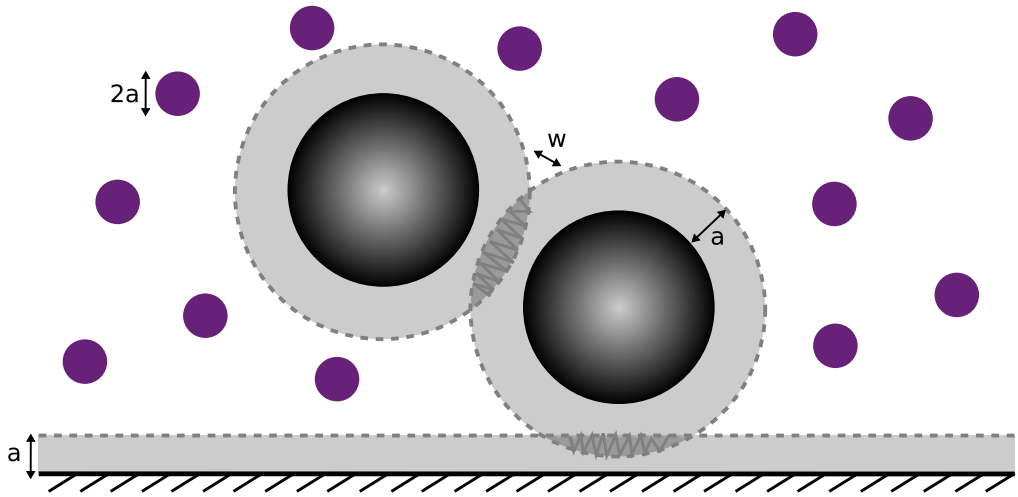

Figure 5.1.: Sketch demonstrating the origin of depletion forces between two large colloids (black circles) and between a colloid and a planar wall (solid black line). Smaller cosolutes (purple circles) of diameter $2a$ exclude the volume of a spherical shell of width a (indicated by the light grey region) around the larger colloids and the volume of a slab of width a above the wall. If the overlap volume (shaded and dashed dark grey regions) has a non-zero width w, no small particle can fit in between the two colloids or between the colloid and the wall.

More recently, there has been significant interest in the characterization of depletion forces in non-equilibrium systems [109, 110, 111, 112, 113]. In general, out of equilibrium, these forces exhibit qualitatively different behavior compared to their equilibrium counterpart. For example, depletion forces on two colloids in a bath of flowing Brownian particles are unequal and can be attractive or repulsive [110, 114]. Within the context of active matter, the tendency of particles to aggregate in layers at surfaces [94] leads to long-ranged oscillatory repulsive forces between immersed passive objects [115, 116, 117].

In this chapter, we will employ the idea of the active stress introduced in chapter 4 to study the force on a probe immersed in a bath of active particles under circular confinement. Furthermore, we will compare our results with experiments of an optically trapped probe surrounded by Janus particles confined in a ring. The experiments were carried out in the group of Prof. Clemens Bechinger at Fachbereich Physik, Universität Konstanz.

5.1 Experimental realization

In experiments, the probe, shown in fig. 5.2, is composed of a disc of thickness $3.5\,\mu\mathrm{m}$ and radius $r_\mathrm{p} = 7.5\,\mu\mathrm{m}$ onto which a hemisphere of diameter $11\,\mu\mathrm{m}$ is fabricated. The translational diffusion constant of the probe $D = 0.003\,\mu\mathrm{m}^2/\mathrm{s}$. It is held in an optical trap using an infrared laser of wavelength $1064\,\mathrm{nm}$. To estimate trap stiffness k, the probe is placed at the center of the confinement and the bath is rendered passive by turning off illumination. By measuring the displacement of the probe $\Delta x = x_\mathrm{p} - x_\mathrm{tr}$ with respect to the trap center, using the equipartition theorem, k is estimated to be $k = k_\mathrm{B}T/\Delta x^2 = 0.50 \pm 0.02\,\mathrm{pN}/\mu\mathrm{m}$ where the temperature of the system $T = 291\,\mathrm{K}$. The narrow beam width ($2\,\mu\mathrm{m}$) ensures that the trapping laser does not undesirably heat up the surrounding medium. Active particles are spheres of radius $r_\mathrm{a} \approx 1\,\mu\mathrm{m}$ made of silica semi-coated with a $20\,\mathrm{nm}$ carbon film. The entire setup is suspended in a sample cell of height $15\,\mu\mathrm{m}$ containing a mixture of water and propylene glycol *n*-propyl ether (PnP). When uniformly illuminated with a laser of wavelength $532\,\mathrm{nm}$ and intensity $7\,\mu\mathrm{W}/\mu\mathrm{m}^2$, because of the higher absorption of light by the carbon cap compared to silica, the temperature at the active particles' surface becomes anisotropic. If the temperature of the carbon side exceeds the critical temperature, local demixing of the binary fluid ensues which in turn triggers self-propulsion of particles [118]. A circular confinement of diameter $100\,\mu\mathrm{m}$ is fabricated on the glass slide using photolithography.

The rotational diffusion constant $D_\mathrm{r} \approx 0.04\,\mathrm{s}^{-1}$ and the propulsion speed $v_0 = 0.40 \pm 0.08\,\mu\mathrm{m}/\mathrm{s}$ were obtained by fitting the mean-squared displacement $\langle \Delta r^2(\Delta t)\rangle$ of active particles in a dilute suspension with [120]

$$\langle \Delta r^2(\Delta t)\rangle = 4D_0\Delta t + \frac{v_0^2}{2D_\mathrm{r}^2}\left[2D_\mathrm{r}\Delta t + \mathrm{e}^{-2D_\mathrm{r}\Delta t} - 1\right]. \tag{5.1}$$

The persistence length of directed motion is thus $\ell_\mathrm{p} \equiv v_0/D_\mathrm{r} \approx 9.5\,\mu\mathrm{m}$. The experiments were performed at a fixed packing fraction of 0.31 ± 0.02. After turning the illuminating laser off, the translational diffusion constant was independently estimated from the long-time limit of the mean-square displacement of passive particles to be $D_0 \approx 0.053\,\mu\mathrm{m}^2/\mathrm{s}$.

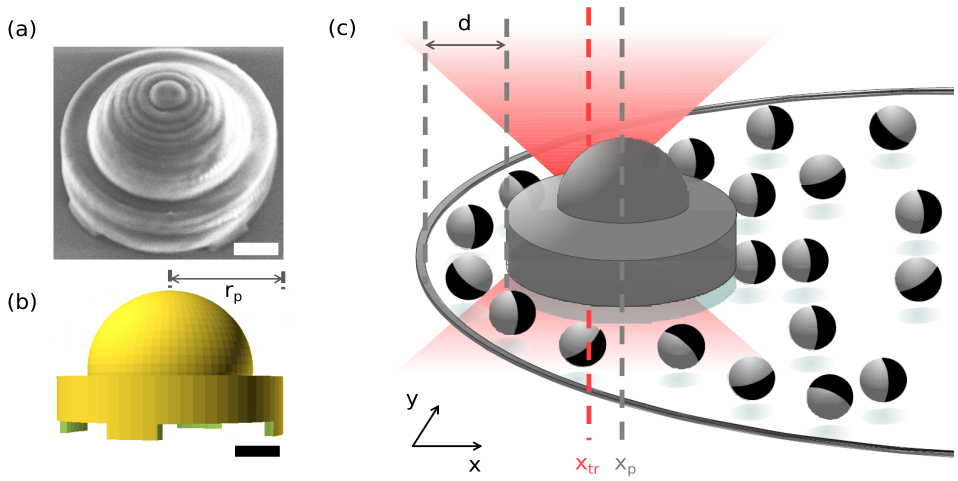

Figure 5.2.: Experimental system. (a) Scanning electron microscope image of the probe and (b) a sketch of the geometry of the probe of radius r_p. The four legs at the bottom helps reduce friction with the underlying substrate. The scale bars correspond to $3\,\mu m$. (c) Schematic diagram of the setup. The surface-to-surface distance between the confinement (grey solid line) and the probe at x_p is d. The minimum of the trapping potential is at x_{tr} and the displacement of the probe with respect to the trap center is $\Delta x = x_p - x_{tr}$. Along the y axis, the probe is symmetrically placed in the circular confinement. The bicolored spheres correspond to active particles whose surface is composed of two different materials (silica and carbon). Reproduced from [119].

5.2 Simulation setup

We perform Brownian dynamics simulations of $N = 780$ particles to complement experiments. The dynamics of the position $\mathbf{r}_i$ and orientation of the ith particle is governed by eq. (2.23). We derive the parameters of our model from experimentally obtained values. For these set of parameters, an equivalent system of active particles without the probe and confinement does not undergo phase separation. The translational mobility of the active particles $\mu_0 = D_0/(k_\mathrm{B}T)$. The position of the probe $\mathbf{r}_\mathrm{p}$ evolves in accordance with

$$\dot{\mathbf{r}}_\mathrm{p} = -\mu\nabla U - \mu k(\mathbf{r}_\mathrm{p} - \mathbf{r}_\mathrm{tr}) + \sqrt{2D}\boldsymbol{\xi}, \tag{5.2}$$

where $\mu = D/(k_\mathrm{B}T)$ is the translational mobility of the probe and $\mathbf{r}_\mathrm{tr}$ is the position of the trap center. The components of $\boldsymbol{\xi}$ are drawn from a uniform distribution over $\left[-\sqrt{3}, \sqrt{3}\right]$. The total potential energy due to excluded-volume interactions between various components of the system $U = \sum_{k<l} u_\mathrm{aa}(|\mathbf{r}_k - \mathbf{r}_l|) + \sum_k u_\mathrm{ap}(|\mathbf{r}_k - \mathbf{r}_\mathrm{p}|) + \sum_k u_\mathrm{ac}(r_\mathrm{con} - |\mathbf{r}_k|) + u_\mathrm{pc}(r_\mathrm{con} - |\mathbf{r}_\mathrm{p}|)$ where r_con is the radius of the circular confinement. All interactions are modelled using the WCA potential [eq. (2.54)] with the following parameters:

Component pair	**WCA potential**	**Length scale of potential**
active particle-active particle	u_aa	$\sigma_\mathrm{aa} = 2^{5/6} r_\mathrm{a}$
active particle-probe	u_ap	$\sigma_\mathrm{ap} = 2^{-1/6}(r_\mathrm{a} + r_\mathrm{p})$
active particle-confinement	u_ac	$\sigma_\mathrm{ac} = 2^{-1/6} r_\mathrm{a}$
probe-confinement	u_pc	$\sigma_\mathrm{pc} = 2^{-1/6} r_\mathrm{p}$

The energy scale of the potential $\varepsilon = 100 k_\mathrm{B}T$. The equations of motion are evolved with an integration time step $\delta t \leq 1\,\mathrm{ms}$.

5.3 Force on the probe

Effect of confinement

We study the variation of force on the probe $\mathbf{F} = (F_x, F_y)^T = k(\Delta x, \Delta y)^T$ as a function of normalized surface-to-surface distance $d' = d/(2r_a)$ between the probe

and the confinement. The force F_x varies non-monotonically with d' as plotted in fig. 5.3 (e,f). Representative snapshots in fig. 5.3 (b-d) show layering of APs in the space between the confinement and the probe. On increasing d' more layers can fit in the gap. These layers form a dynamical bridge between the two surfaces. When the probe is sufficiently far from the confinement, the decay of particle density away from the boundary (probe) is unperturbed by the presence of the probe (boundary) thereby precluding the formation of the bridge [cf. fig. 5.3 (a)].

To gain further insight into the effect of confinement on the motion of the probe, we plot the probability distribution of the probe's displacement about the trap center in fig. 5.4 for different surface-to-surface distances d'. The distribution of displacements along the y axis (along which the system is symmetric) follows a Gaussian distribution with zero mean. For $d' = 0.77$, the distribution of displacements along the x axis, $P(\Delta x)$, is asymmetric and peaks at $\Delta x \approx 0.5$ indicating that the probe is being displaced away from the confinement due to forces exerted by APs. On increasing d', the probe needs to be displaced by a shorter distance to make space for APs. This reflects in the decrease in F_x. At $d' \approx 1$, there is enough room for APs to form a monolayer at the confinement without displacing the probe. Therefore, the force on the probe is miniscule but non-zero. A combination of (isotropic) thermal fluctuations and steric interactions with the monolayer favours the motion of the probe away from the monolayer. The influence of translational noise is, however, small. Correspondingly, $P(\Delta x)$ is slightly asymmetric with a peaked probability toward small and positive Δx. Upon increasing d' further, APs force the probe away from the monolayer leading to an increase in F_x. The distribution at $d' = 1.6$ is asymmetric with a peak at $\Delta x \approx 0.3$. A second minimum in F_x seen at $d' \approx 2$ is implied by the formation of a bilayer at the confinement. For large d', since particles interact isotropically with the probe, $P(\Delta x)$ becomes a Gaussian distribution centered at zero as a result of which $F_x \approx 0$.

Effect of propulsion speed

On increasing propulsion speed v_0, due to a corresponding increase the persistence length ($\ell_\mathrm{p} \propto v_0$), the tendency of APs to aggregate at surfaces [94] increases. The surface pressure exerted by them is thereby larger [121]. APs with larger v_0 are thus capable of *squeezing* through a narrower gap. As plotted in fig. 5.5 (c), this results in a considerably larger force even at small distances. As apparent in representative

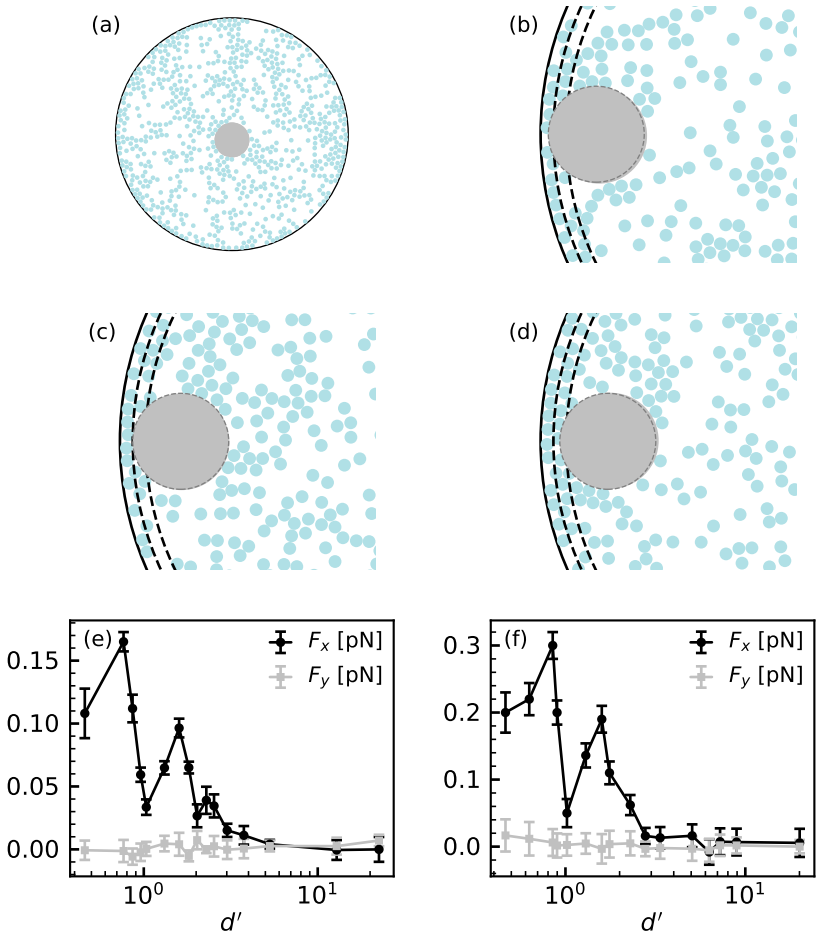

Figure 5.3.: (a) Snapshot of the full system with the trapped probe near the center of the confinement. (b-d) Zoomed snapshots with the probe at $d' = \{0.76, 1.03, 1.60\}$. The active particles are plotted as blue circles. The confinement is the solid black line. The dashed lines are separated by $2r_a$. The filled, grey circle represents the probe and the dashed circle is where the probe would be if its center coincided with the trap center. Components of the force as a function of d' as measured in (e) simulations and (f) experiments.

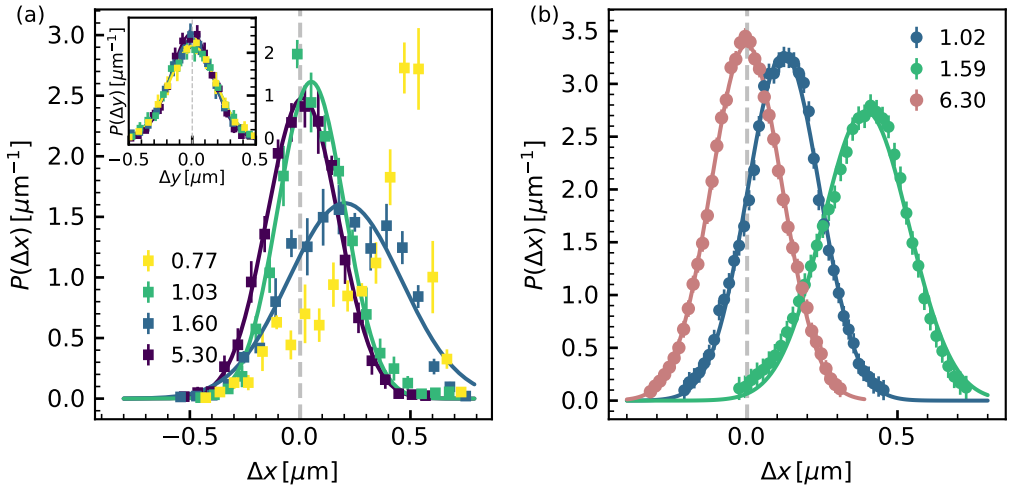

Figure 5.4.: Probability distribution of the probe's displacement along the x axis $\Delta x = x_\mathrm{p} - x_\mathrm{tr}$ in (a) simulations and (b) experiments for different surface-to-surface distances d'. The solid lines are fits to a Gaussian distribution. The inset in (a) corresponds to the probability distribution of the probe's displacement along the y axis.

snapshots shown in fig. 5.5 (a,b), large v_0 also promotes formation of layers leading to a slower decay of the density away from the confinement and an enlarged span of the dynamical bridge of APs between the probe and the confinement. As a result, F_x decays to zero further away from the confinement.

To understand the effect of v_0 on the dynamics of the probe in bulk, we now place the probe near the center of the confinement. The probability distribution $P(\Delta x)$ for different speeds in plotted in fig. 5.5 (d,e). The symmetry of $P(\Delta x)$ about zero implies that the net force on the probe is zero. For passive particles ($v_0 = 0$), the distribution is Gaussian. As v_0 increases, the width of the distribution increases and non-Gaussian tails develop due to correlations induced by finite persistence of APs. Such non-equilibrium signatures in the distribution have also been observed in bacterial baths [122].

In order to obtain a quantitative relationship between the distribution of APs and the force on the probe, we now use the framework of the active stress introduced in chapter 4.

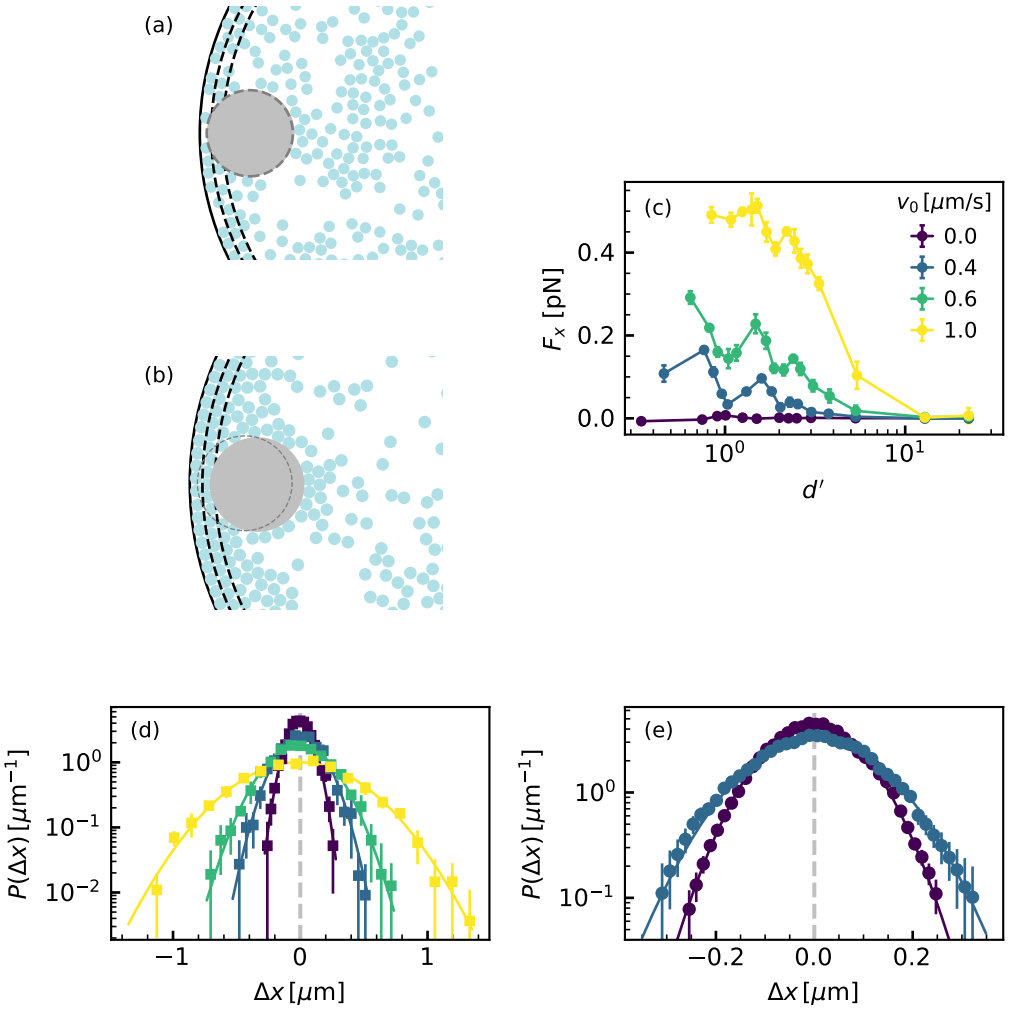

Figure 5.5.: Zoomed-in snapshots of the system with (a) $v_0 = 0.3\,\mu\mathrm{m/s}$ and (b) $v_0 = 1\,\mu\mathrm{m/s}$. The probe is represented as a grey circle and the dashed circle is where the probe would be if its center coincided with the trap center. The solid line represents the confinement. The dashed lines are separated by $2r_a$. The blue circles correspond to APs. (c) Force on the probe F_x as a function of surface-to-surface distance d' for different propulsion speeds v_0. (d) Probability density of displacements $P(\Delta x)$ with the probe placed near the center of the confinement. Markers are data points from simulations and solid lines correspond to fits to a Gaussian distribution. (e) $P(\Delta x)$ measured in experiments (markers) and Gaussian fits (solid lines). The legend in (c) is carried forward to panels (d) and (e).

5.3.1 Active stress

Neglecting the nematic tensor, the total stress tensor [eq. (4.7)] in the force-free region away from the probe and the wall reduces to [123]

$$\boldsymbol{\sigma} = -\rho k_{\mathrm{B}} T \mathbf{1} - \frac{v_0}{D_{\mathrm{r}}} \left[\frac{\hat{v}}{2\mu_0} \rho \mathbf{1} - k_{\mathrm{B}} T (\nabla \mathbf{p})^{ST} \right], \tag{5.3}$$

where $\hat{v}(\mathbf{r}) = \hat{v}(\rho(\mathbf{r}))$ is the density-dependent effective speed that considers excluded-volume interactions between particles. In the absence of currents, the force on the probe $\mathbf{F}$ given by eq. (4.10) simplifies to

$$\mathbf{F} = \oint_{\partial A} \mathrm{d}l \; \mathbf{n} \cdot \boldsymbol{\sigma} \tag{5.4}$$

where ∂A is the contour over which we perform the integral. We choose a circular contour of radius $r_b > (r_{\mathrm{a}} + r_{\mathrm{p}})$ whose center coincides with the probe's position. The boundary is thus outside the range of the pair potential between the probe and active particles. Using $\mathbf{n} = \mathbf{e}_r$, the integral over the second term in eq. (5.3) involves

$$\int_0^{2\pi} \mathrm{d}\varphi \; \hat{v}(r,\varphi) \mathbf{e}_r \rho(r,\varphi) = v_{\mathrm{eff}} \int_0^{2\pi} \mathrm{d}\varphi \; \mathbf{e}_r \rho(r,\varphi) \tag{5.5}$$

where v_{eff} is an effective propulsion speed which we assume to be independent of φ. To calculate the contribution of the polarization, we need

$$\begin{aligned} \mathbf{e}_r \cdot (\nabla \mathbf{p})^{ST} = 2 \frac{\partial p_r}{\partial r} \mathbf{e}_r + \frac{\partial p_\varphi}{\partial r} \mathbf{e}_\varphi + \frac{1}{r} \left(\frac{\partial p_r}{\partial \varphi} - p_\varphi \right) \mathbf{e}_\varphi \\ - \left(\frac{\partial p_r}{\partial r} + \frac{p_r}{r} + \frac{1}{r} \frac{\partial p_\varphi}{\partial \varphi} \right) \mathbf{e}_r. \end{aligned} \tag{5.6}$$

On integrating this dot product over φ, using $\partial_\varphi \mathbf{e}_r = \mathbf{e}_\varphi$ and $\partial_\varphi \mathbf{e}_\varphi = -\mathbf{e}_r$, many terms vanish because $\int_0^{2\pi} \mathrm{d}\varphi \; \sin\varphi = \int_0^{2\pi} \mathrm{d}\varphi \; \cos\varphi = 0$ and we are left with

$$\int_0^{2\pi} \mathrm{d}\varphi \; \mathbf{e}_r \cdot (\nabla \mathbf{p})^{ST} = \frac{\partial}{\partial r} \int_0^{2\pi} \mathrm{d}\varphi \; \mathbf{p}(r,\varphi). \tag{5.7}$$

On gathering terms, eq. (5.4) becomes

$$\begin{aligned} \mathbf{F} = -k_{\mathrm{B}} T \left(1 + \frac{v_0 v_{\mathrm{eff}}}{2 D_0 D_{\mathrm{r}}} \right) \int_0^{2\pi} \mathrm{d}\varphi \; r_b \mathbf{e}_r \rho(r_b,\varphi) \\ + \frac{k_{\mathrm{B}} T v_0 r_b}{D_{\mathrm{r}}} \left[\frac{\partial}{\partial r} \int_0^{2\pi} \mathrm{d}\varphi \; \mathbf{p}(r,\varphi) \right]_{r=r_b}. \end{aligned} \tag{5.8}$$

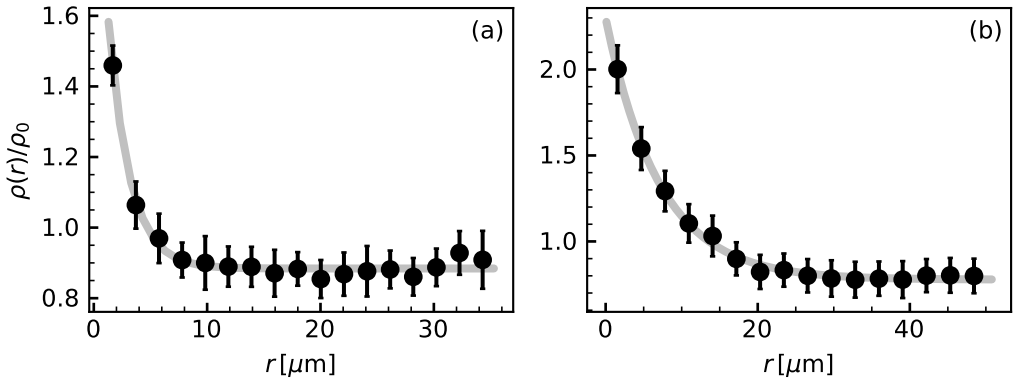

Figure 5.6.: Decay of density (normalized by global number density $\rho_0 \approx 0.099$) away from the probe in (a) simulations and (b) experiments. Error bars denote the standard deviations obtained from five independent measurements. The black markers correspond to measurements and the grey line is a fit to the function $\rho(r)/\rho_0 = a + b\mathrm{e}^{-r/\xi}$.

Writing the polarization in terms of the density using[2] $\mathbf{j} = \hat{v}\mathbf{p} - D_0\nabla\rho = 0$ and approximating $\hat{v} = v_{\text{eff}}$, the integral over the polarization becomes

$$\int_0^{2\pi} \mathrm{d}\varphi\ \mathbf{p}(r,\varphi) = \frac{D_0}{v_{\text{eff}}} \int_0^{2\pi} \mathrm{d}\varphi\ \left(\frac{\partial\rho}{\partial r}\mathbf{e}_r + \frac{1}{r}\frac{\partial\rho}{\partial\varphi}\mathbf{e}_\varphi\right) = -\frac{D_0}{v_{\text{eff}}}\left(\mathbf{c}'(r) + \frac{\mathbf{c}(r)}{r}\right) \quad (5.9)$$

with

$$\mathbf{c}(r) = -\int_0^{2\pi} \mathrm{d}\varphi\ \mathbf{e}_r\rho(r,\varphi). \quad (5.10)$$

To evaluate the integral, we need information on how the density decays. For an object that does not generate currents, we know from chapter 4 that the density satisfies eq. (4.14). As also confirmed by simulations and experiments [cf. fig. 5.6], the density decays exponentially with decay length ξ. Substituting $\rho(r,\varphi) \approx \rho(r_b,\varphi)\mathrm{e}^{-(r-r_b)/\xi}$ in eq. (5.9), the contribution of polarization to the force becomes

$$\frac{k_\mathrm{B}Tv_0r_b}{D_\mathrm{r}}\left[\frac{\partial}{\partial r}\int_0^{2\pi}\mathrm{d}\varphi\ \mathbf{p}(r,\varphi)\right]_{r=r_b} = k_\mathrm{B}T\frac{D_0}{\xi^2 D_\mathrm{r}}\frac{v_0}{v_{\text{eff}}}\left[\frac{\xi^2}{r_b^2} + \frac{\xi}{r_b} - 1\right] r_b\mathbf{c}(r_b). \quad (5.11)$$

Gathering terms, we get the total force on the object

$$\mathbf{F} = -k_\mathrm{B}T_{\text{eff}}\mathbf{C}; \qquad \mathbf{C} = r_b\mathbf{c}(r_b). \quad (5.12)$$

[2] A symmetric probe does not generate currents.

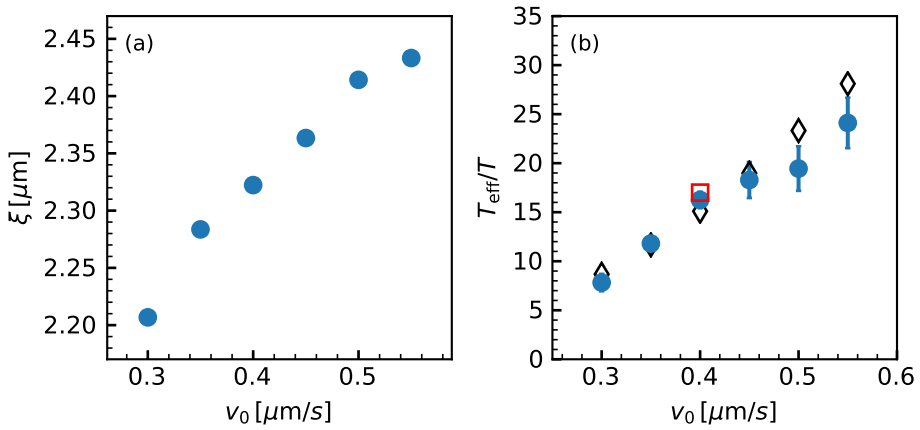

Figure 5.7.: (a) Decay length ξ as a function of propulsion speed v_0 obtained from simulations. (b) Effective temperature T_{eff} (normalized by bath temperature T). Simulation data (closed symbols) is plotted along with the prediction from eq. (5.13) (open symbols). The red square corresponds to the experimental value.

The factor

$$k_{\text{B}}T_{\text{eff}} = k_{\text{B}}T\left[1 + \frac{v_0 v_{\text{eff}}}{2D_0 D_{\text{r}}} + \frac{D_0}{\xi^2 D_{\text{r}}}\frac{v_0}{v_{\text{eff}}}\left(\frac{\xi^2}{r_b^2} + \frac{\xi}{r_b} - 1\right)\right] \tag{5.13}$$

can be interpreted as an effective temperature that enables an activity-induced increase in the effective diffusion constant. In the equilibrium limit ($v_0 = 0$), as expected, T_{eff} is identical to the bath temperature T. The distribution of particles around the probe also contributes to T_{eff} through the decay length ξ. We obtain the decay length ξ by fitting the density profile $\rho(r) = \int_0^{2\pi} \mathrm{d}\varphi\ \rho(r,\varphi)$ to an exponential function and plot it in fig. 5.7 for several propulsion speeds v_0. We find that the corresponding (normalized) effective temperature T_{eff}/T agrees well with eq. (5.13).

To calculate the x component of the contour integral C_x which determines the force F_x, we need the angle-resolved density $\rho(r_b, \varphi)$ evaluated at a distance r_b from the center of the probe. Due to symmetry, the y component of the integral $C_y = 0$. We fix $r_b = r_{\text{p}} + 2.2r_{\text{a}}$, though, as discussed in appendix A.3, the contour integral is independent of this specific choice. In fig. 5.8, we plot the time-averaged density $\rho(r_b, \varphi)$ for several normalized surface-to-surface distances d'. The non-monotonicity in the resulting force is reflected in changes in the density profile for different d'. At $d' \approx 1.3$, in both experiments and simulations, $\rho(r_b, \varphi)$ develops two off-center peaks indicating that APs accumulate at corners in wedges between the confinement and

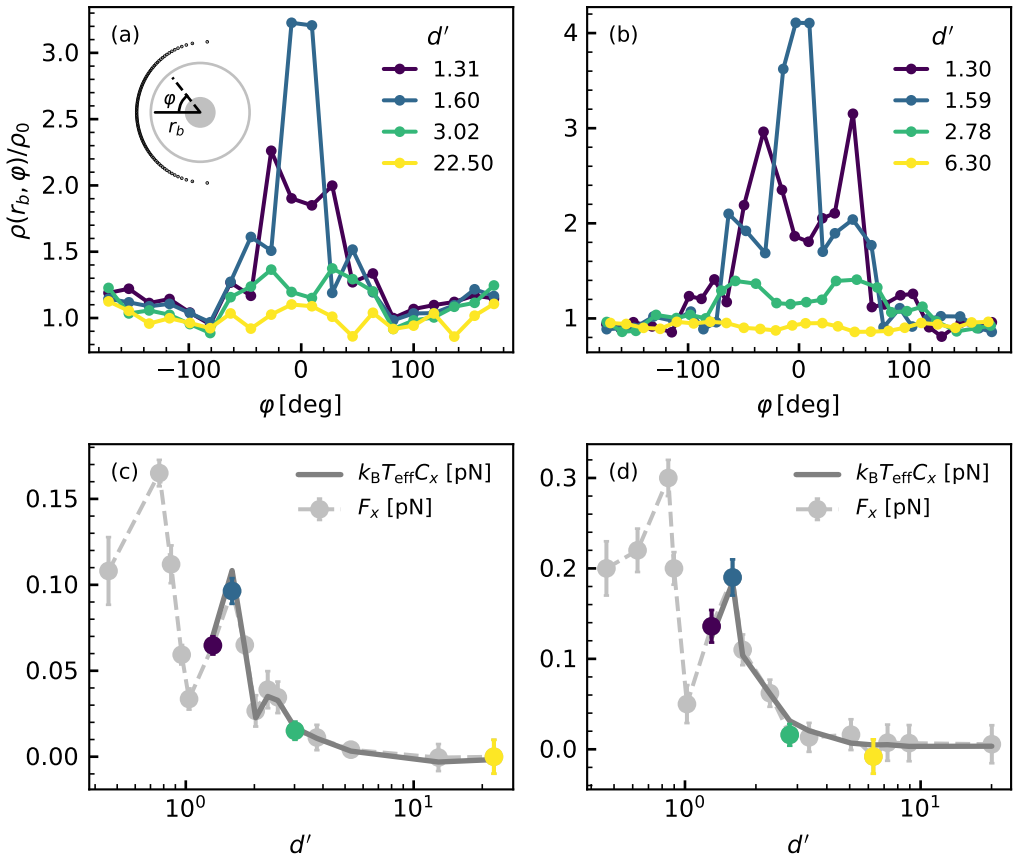

Figure 5.8.: Angle-resolved density profile $\rho(r_b, \varphi)/\rho_0$ for different surface-to-surface distances d' measured in (a) simulations and (b) experiments. We choose the radius of the boundary $r_b = r_p + 2.2r_a$. The inset in (a) depicts a sketch of the contour along which we calculate the density. Also shown is the force on the probe F_x and the prediction from eq. (5.12) evaluated in (c) simulations and (d) experiments. The colored markers in (c) and (d) correspond to distances for which the density has been plotted in (a) and (b).

probe. Increasing d' allows APs to jostle through the gap between the confinement and probe. At $d' \approx 1.6$, this results in a peak at $\varphi \approx 0$. For large d' where the enhanced density at the confinement due to accumulation of APs has sufficiently decayed, the angle-resolved density profile is flat and fluctuates about the global number density ρ_0. This implies that $\rho(r_b, \varphi) = \rho(r_b)$ is independent of φ.

From the angle-resolved density, we obtain $\mathbf{C}$ using eq. (5.12) through numerical integration. Fitting for the effective temperature T_{eff}, we find that the experimental value of $T_{\text{eff}} \approx 17T$ and the value of $T_{\text{eff}} \simeq 16.25T$ obtained from simulations closely agree. Note that T_{eff} is independent of d'. The force F_x is plotted along with $k_B T_{\text{eff}} C_x$ in fig. 5.8.

5.3.2 Effect of attractive interactions

As evident from fig. 5.3, though simulations capture the non-monotonic behavior of the experimentally measured force qualitatively, there is a quantitative discrepancy. To apprehend the cause of this disagreement, we plot the distribution of contact times of APs with the probe and confinement in fig. 5.9. The experiments performed to determine τ_c have been performed in a smaller confinement of radius $r_{\text{con}} = 15\,\mu\text{m}$. From fig. 5.9 (a), we infer that the distribution of contact times of APs with the confinement for purely repulsive particles [$\varepsilon_{\text{att}} = 0k_{\text{B}}T$ in the figure] employed in the simulations hitherto is significantly narrower and decays much more rapidly than that measured in experiments. APs therefore spend a longer time near the wall in experiments. From previous works we know that the decrease in rotational diffusion as APs approach the confinement is marginal [124, 50]. The distribution of contact times with the probe measured from simulations and experiments, in contrast, agree reasonably well.

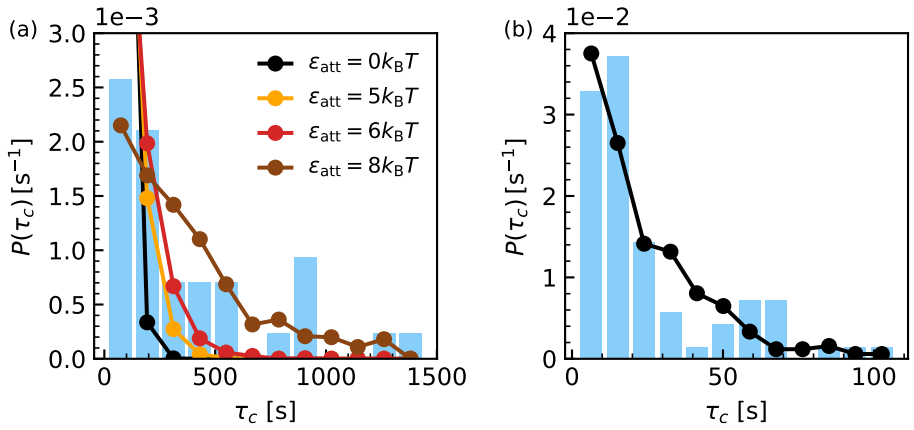

Figure 5.9.: Probability distribution $P(\tau_c)$ of contact times τ_c of APs with (a) the confinement and (b) the probe. Experimental results are represented as bars. Simulation results for different attraction strengths ε_{att} is plotted as lines.

To study the consequence of larger contact times, we now introduce an attractive part to the interaction potential. We construct this potential u by gluing the WCA potential with the attractive part of the potential introduced by Wang *et al.* [125] at their minima

$$u(r) = \begin{cases} u_{\text{WCA}} - \varepsilon_{\text{att}} & \text{if } r \leq r_{\text{min}} \\ u_{\text{att}} & \text{if } r_{\text{min}} < r \leq r_{\text{cut}} \\ 0 & \text{otherwise.} \end{cases} \tag{5.14}$$

The attractive potential is given by

$$u_{\text{att}}(r) = \gamma\varepsilon_{\text{att}}\left[\left(\frac{\sigma}{r}\right)^2 - 1\right]\left[\left(\frac{r_{\text{cut}}}{r}\right)^2 - 1\right]^2 \tag{5.15}$$

with

$$\gamma = 2\left(\frac{r_{\text{cut}}}{\sigma}\right)^2\left(\frac{3}{2\left(r_{\text{cut}}^2/\sigma^2 - 1\right)}\right)^3 \tag{5.16}$$

where ε_{att} is the strength of attraction. The minimum of u_{att} is at a distance

$$r_{\text{min}} = r_{\text{cut}}\left(\frac{3}{1 + 2r_{\text{cut}}^2/\sigma^2}\right)^{\frac{1}{2}}. \tag{5.17}$$

The glued potential $u(r)$ reduces to the WCA potential for $\varepsilon_{\text{att}} = 0$. In our extended model with attraction, we set $r_{\text{min}} = r_{\text{a}}$ and $r_{\text{cut}} = 1.05r_{\text{a}}$ to calculate u_{att} between the probe and confinement. To calculate the potential between APs and the probe, we set $r_{\text{min}} = r_{\text{a}} + r_{\text{p}}$ and $r_{\text{cut}} = 1.05 \times (r_{\text{a}} + r_{\text{p}})$. No attraction is introduced between APs; so $\varepsilon_{\text{att}} = 0$.

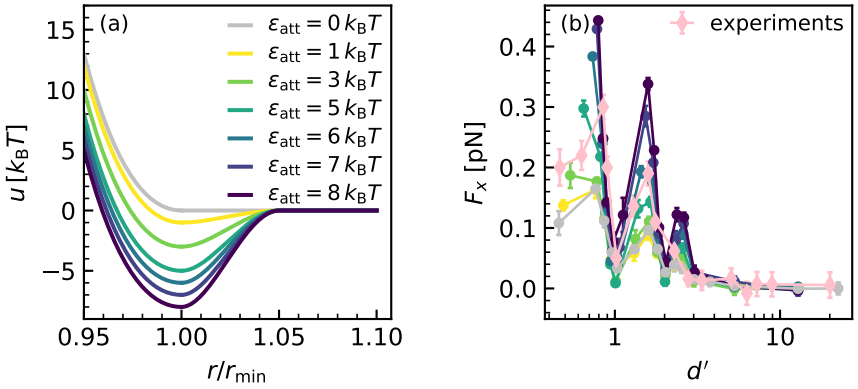

Figure 5.10.: (a) Glued pair potential u [eq. (5.14)] for different attraction strengths ε_{att}. (b) Force on the probe F_x as a function of surface-to-surface distance d' for different ε_{att}. Error bars are standard deviations calculated from five independent simulations.

On introducing attraction, as shown in fig. 5.9, APs spend more time near the confinement resulting in a broader distribution of contact times which approaches the experimental distribution. A plausible cause for an effective attraction at the confinement in experiments could be surface roughness or hydrodynamic interactions, both of which we have neglected throughout in simulations. Figure 5.10 shows that the force systematically increases on increasing ε_{att} for all distances d'. An attractive

strength of $\varepsilon_{\text{att}} \simeq 5 - 6k_{\text{B}}T$ yields good agreement with experiments. A third peak that is consistently observed in simulations due to the formation of a bilayer at the confinement is unseen in experiments.

5.3.3 Effect of confinement shape

To investigate the possible effect of the shape of confinement on the force exerted on the probe, we consider a lunar confinement depicted in fig. 5.11 (a). We fix the diameter of the larger arc at $100\,\mu\text{m}$. From fig. 5.11 (b), we conclude that the force on the probe is independent of the diameter of the smaller arc d_{s} for all distances. Therefore, the magnitude and sign of the confinement's curvature does not measurably affect the force. Whether making d_{s} comparable to the diameter of the probe $2r_{\text{p}}$ has an effect on the force remains to be tested.

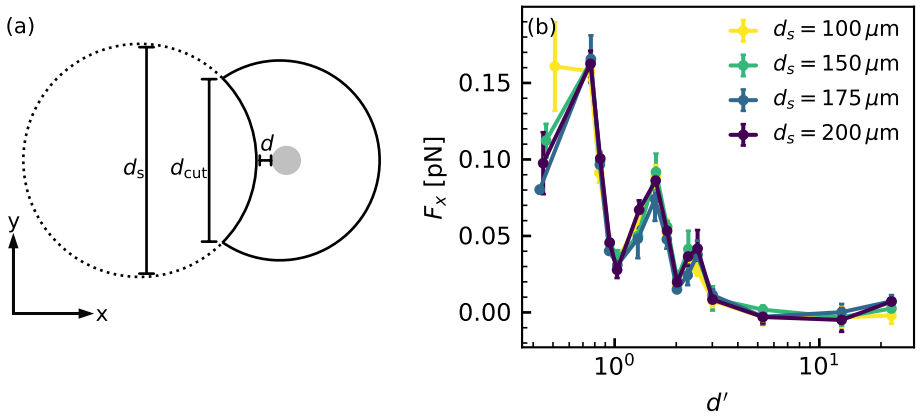

Figure 5.11.: (a) Sketch of the system under lunar confinement. A circle of diameter d_{s} is cut out. We set $d_{\text{cut}} = 60\,\mu\text{m}$. The surface of the trapped probe (circle) is at a distance of $d\,\mu\text{m}$ from the confinement. (b) Force on the probe F_x as a function of surface-to-surface distance d' for diameters of the cut-out circle d_{s}. Error bars are standard deviations calculated from five independent simulations.

6 Summary and outlook

Collective forces and torques that emerge from interactions at the active particle scale govern a multitude of macroscopic phenomena unreachable in equilibrium. For example, they generate non-vanishing currents capable of driving microscopic engines and prompt phase separation into dense and dilute regions in the absence of attractive interactions. In this thesis, we investigated different ways in which such collective forces and torques manifest themselves in active matter. First, we studied how they control the emerging phase behavior of elongated self-propelled particles. Secondly, we determined how active particles transmit forces onto immersed passive objects. On a related note, thirdly, we rationalized the experimentally measured force on an optically trapped probe in a confined active fluid.

Connecting scalar and polar active matter, in chapter 3, we modelled anisotropic interactions between active particles through the repulsive variant of the Gay-Berne potential [65]. By varying a single parameter of the potential, the aspect ratio, we smoothly interpolated between isotropic, discoidal particles and elongated polar ellipses. In order to restrict our focus to inter-particle interactions, we set the Peclét number to infinity. This means that an isolated particle will move along a straight line. At the packing fraction we considered, discoids exhibit motility-induced phase separation (MIPS). On increasing the aspect ratio, MIPS breaks down and particles dynamically group into mobile polar domains. Eventually, for large aspect ratios, the system again phase separates into dense and dilute regions. In contrast to MIPS, in this case, the dense phase is highly polarized. We explained the formation of these qualitatively different phases observed in simulations by extracting two effective parameters, *viz.*, the coupling to the local polarization and the force-imbalance coefficient, that enter the mean-field narrative. More generally, in addition to these phases, noise-driven transitions can be observed on reducing the Peclét number [126]. Conspicuously, we did not observe vortices or visual signatures of active turbulence in our system. These have been reported in larger simulations of self-propelled rods interacting through the Yukawa potential [78]. To obtain chaotic behavior in the mean-field equations, in Ref. [127], an explicit coupling

to the flow of the surrounding fluid had to be considered. Moreover, in general, anisotropy in shape leads to an anisotropic mobility tensor [128]. The effect of non-degenerate parallel and perpendicular mobilities will be addressed in future work. The collective behavior of anisotropic, chiral active matter in which there is an interplay of alignment and persistent rotation is another area that has received great attention in recent times [129].

In chapter 4, we studied how active particles interact with fixed passive objects. When immersed in an active bath, passive inclusions have the conditional ability to generate currents depending on their shape. The currents they generate act back on them in the form of a net force or torque. By employing the divergence theorem, we expressed the force on the object in terms of the total stress tensor and the particle current. Though the force is completely determined by the current dipole moment in an unbound system, the idea of viewing inclusions as current dipoles is not universally applicable. Particularly, in a finite system with periodic boundary conditions, the contribution from the current dipole vanishes and the force on the inclusion is sustained by the vorticity (curl of polarization) of particles in its vicinity. The force can also be independently expressed in terms of the integrated boundary current. Interestingly, the system size L has an enormous influence on the magnitude of force which grows as L^2 before plateauing to a constant value. This indicates the presence of a minimal separation between inclusions that maximizes the force. By choosing inclusions shaped like a boomerang and a duck, we corroborated our theoretical results with numerical simulations of active Brownian particles. These results have practical implications in the design of objects that are optimized for a specific behavior.

To test the concept of the active stress, in chapter 5, we applied it to an experimental system of an optically trapped, disc-shaped probe in a circularly confined suspension of light-activated self-diffusiophoretic particles. We modelled the system using active Brownian particles that interact repulsively with a larger particle (probe) in a harmonic potential. On increasing the separation between the probe and the confinement, the force on the probe varies non-monotonically before decaying to zero for large distances. We rationalized this qualitatively using the fact that active particles accumulate in layers at the confinement due to their persistent motion. Since we measured a lower contact time between the active particles and the probe, we introduced attractive interactions between them. Doing so yielded a better quantitative agreement of the forces measured in simulations and experiments. We

showed that the density field of active particles around the probe determines the force, therewith establishing a direct relationship between force generated by the active fluid and their microstructure. The indifference of our approach toward system-specific interactions renders it readily applicable to the broader class of synthetic and living active matter.

Our current knowledge of collective forces and torques, to which this thesis aimed to contribute, provides a bottom-up understanding of several well-established features of active matter including clustering, aggregation at surfaces and persistent steady-state currents. In nature, active matter often finds itself in spatially heterogeneous environments like a habitat with randomly placed obstacles (trees in a jungle, for example) or porous media. Such surroundings significantly alter their collective behavior [130, 131, 132]. A comprehensive theoretical study of the interplay of geometry and aggregation of (generically) anisotropic active matter could prove useful in improving budding technologies that exploit microbial metabolism for, *inter alia*, healing fissures in concrete [133] and oil recovery [134, 135]. The other aspect of active matter producing non-vanishing currents has already been used to conceive bacteria-driven micromotors [37]. The question of how to optimize the shape of such a motor remains to be investigated. Akin to the passive assembly of lock-and-key colloids that fit together like a ball and socket [136], activity-mediated self-assembly of differently-shaped passive objects is another fascinating avenue for further research.

Appendix A

A.1 Gay-Berne potential

The Gay-Berne pair potential, an extension of the 6-12 Lennard-Jones potential, is used to emulate anisotropic particles. It is extensively used in the study of liquid crystals and shows an isotropic-nematic equilibrium phase transition [137, 138]. The potential reads

$$u_{\mathrm{GB}}(\mathbf{r}_{ij}, \mathbf{e}_i, \mathbf{e}_j) = 4\varepsilon\hat{\varepsilon}\left(\iota^{-12} - \iota^{-6}\right) \tag{A.1}$$

where $\iota \equiv r_{ij}/\sigma - \hat{\sigma} + 1$. With $\hat{\mathbf{r}} = \mathbf{r}/r$, the orientation-dependent well depth is

$$\hat{\varepsilon}(\hat{\mathbf{r}}, \mathbf{e}_i, \mathbf{e}_j) = \varepsilon_1^{\nu}(\mathbf{e}_i, \mathbf{e}_j)\varepsilon_2^{\mu}(\hat{\mathbf{r}}, \mathbf{e}_i, \mathbf{e}_j) \tag{A.2}$$

with

$$\varepsilon_1 = [1 - (\alpha \mathbf{e}_i \cdot \mathbf{e}_j)^2]^{-1/2} \tag{A.3}$$

$$\varepsilon_2 = 1 - \frac{\alpha'}{2}\left\{\frac{(\hat{\mathbf{r}} \cdot \mathbf{e}_i + \hat{\mathbf{r}} \cdot \mathbf{e}_j)^2}{1 + \alpha' \mathbf{e}_i \cdot \mathbf{e}_j} + \frac{(\hat{\mathbf{r}} \cdot \mathbf{e}_j - \hat{\mathbf{r}} \cdot \mathbf{e}_i)^2}{1 - \alpha' \mathbf{e}_i \cdot \mathbf{e}_j}\right\}. \tag{A.4}$$

The anisotropy in shape is measured through

$$\alpha = \frac{\kappa^2 + 1}{\kappa^2 - 1} \tag{A.5}$$

where κ is the aspect ratio of the particle. The anisotropy in energy is quantified by

$$\alpha' = \frac{\kappa'^{1/\mu} - 1}{\kappa'^{1/\mu} + 1} \tag{A.6}$$

where κ' is the ratio of the energy depth of side-by-side and end-to-end configurations of the particle pair. Throughout, we fix $\kappa' = 5, \mu = 2$ and $\nu = 1$.

A.2 Density due to a lattice of current dipoles

Let us consider a square lattice of n identical objects generating current, each with dipole moment $\mathbf{m}$. The density at $\mathbf{r}$ is

$$\delta\rho_L^{\text{ff}}(\mathbf{r}) = \sum_n \delta\rho^{\text{ff}}(\mathbf{r} - \mathbf{R}_n) = \frac{1}{D_{\text{eff}}} \sum_n \frac{\mathbf{m} \cdot (\mathbf{r} - \mathbf{R}_n)}{2\pi |\mathbf{r} - \mathbf{R}_n|^2} \tag{A.7}$$

where L is the lattice constant and $\mathbf{R}_n$ is vector pointing to object n from object $n = 0$ with origin at $\mathbf{R}_0 = 0$. Taylor expanding for small $|\mathbf{r}| \ll |\mathbf{R}_n|$, we get

$$\frac{x_i - X_i}{|\mathbf{r} - \mathbf{R}_n|^2} \approx -\frac{X_i}{\mathbf{R}_n^2} + \left(\frac{\partial}{\partial X_{n,j}} \frac{X_{n,i}}{\mathbf{R}_n^2} \right) x_j. \tag{A.8}$$

Plugging this in eq. (A.7), we get

$$\delta\rho_L^{\text{ff}}(\mathbf{r}) = \delta\rho^{\text{ff}}(\mathbf{r}) + \frac{1}{2\pi D_{\text{eff}}} \sum_{n \neq 0} \left[\frac{\mathbf{m} \cdot (\mathbf{r} - \mathbf{R}_n)}{\mathbf{R}_n^2} - \mathbf{m} \cdot \frac{2\mathbf{R}_n \mathbf{R}_n}{\mathbf{R}_n^4} \cdot \mathbf{r} \right]. \tag{A.9}$$

To compute the term in brackets we need

$$\sum_{n \neq 0} \frac{1}{\mathbf{R}_n^2} = \frac{4}{L^2} \sum_{k=1}^{\infty} \frac{1}{k^2} = \frac{2\pi^2}{3L^2}, \tag{A.10}$$

$$\sum_{n \neq 0} \frac{\mathbf{R}_n}{\mathbf{R}_n^2} = 0, \tag{A.11}$$

$$\sum_{n \neq 0} \frac{\mathbf{R}_n \mathbf{R}_n}{\mathbf{R}_n^4} = \frac{2}{L^2} \mathbf{1} \sum_{k=1}^{\infty} \frac{1}{k^2} = \frac{\pi^2}{3L^2} \mathbf{1} \tag{A.12}$$

where the length of the lattice vector $|\mathbf{R}_n| = kL$. Inserting the above expressions in eq. (A.9), we deduce that the correction to the far-field density vanishes. Hence, considering a lattice of current dipoles leaves the far-field density unchanged and does not resolve the contradictory picture painted by simulations performed in periodic boundaries.

A.3 Contour integral of density

As derived in Chapter 5, the force on the probe $\mathbf{F} = k_{\mathrm{B}}T_{\mathrm{eff}}\mathbf{C}$ where

$$\mathbf{C} \equiv (C_x, C_y)^T = r_b \int_0^{2\pi} \mathrm{d}\varphi \; \rho(r_b, \varphi)(\cos\varphi, \sin\varphi)^T. \tag{A.13}$$

The line integral is measured along a circular contour of radius r_b centered at the probe. The radius r_b should be large enough to be outside the range of the pair potential between active particles and probe but small enough to avoid the influence of the confinement. This prohibits the estimation of the integral at small distances. In fig. A.1, we plot C_x as a function of distance d' for different radii r_b. The integral is robust to changes in r_b.

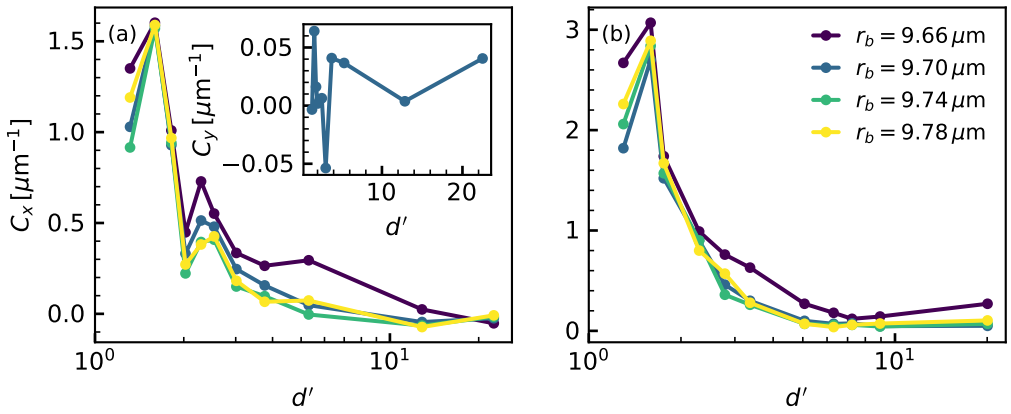

Figure A.1.: Contour integral $C_x = \int_0^{2\pi} \mathrm{d}\varphi \; \rho(r_b, \varphi)\cos\varphi$ as a function of (normalized) surface-to-surface distance between the probe and the confinement d' for different radii of contour r_b measured in (a) simulations and (b) experiments. The inset in (a) shows $C_y = \int_0^{2\pi} \mathrm{d}\varphi \; \rho(r_b, \varphi)\sin\varphi$ as a funciton of d' evaluated at $r_b = 9.7\,\mu\mathrm{m}$.

Moreover, the y component of the contour integral vanishes due to symmetry. In simulations, as shown in the inset of fig. A.1 (a), we find that C_y is indeed small and fluctuates about zero.

Bibliography

[1] C. Battle, C. P. Broedersz, N. Fakhri, et al. “Broken Detailed Balance at Mesoscopic Scales in Active Biological Systems”. In: *Science* 352.6285 (2016), pp. 604–607. DOI: 10.1126/science.aac8167.

[2] J. Henry. *Religion, Magic, and the Origins of Science in Early Modern England*. Variorum Collected Studies Series CS999. Farnham, Surrey, England ; Burlington, VT: Ashgate Pub, 2012.

[3] E. Schrödinger and R. Penrose. *What Is Life?: With Mind and Matter and Autobiographical Sketches*. First. Cambridge University Press, 1992. DOI: 10.1017/CBO9781139644129.

[4] X. Fang, K. Kruse, T. Lu, and J. Wang. “Nonequilibrium Physics in Biology”. In: *Rev. Mod. Phys.* 91.4 (2019), p. 045004. DOI: 10.1103/RevModPhys.91.045004.

[5] A. P. Petroff, X.-L. Wu, and A. Libchaber. “Fast-Moving Bacteria Self-Organize into Active Two-Dimensional Crystals of Rotating Cells”. In: *Phys. Rev. Lett.* 114.15 (2015), p. 158102. DOI: 10.1103/PhysRevLett.114.158102.

[6] N. J. Mlot, C. A. Tovey, and D. L. Hu. “Fire Ants Self-Assemble into Waterproof Rafts to Survive Floods”. In: *Proc. Natl. Acad. Sci. U.S.A.* 108.19 (2011), pp. 7669–7673. DOI: 10.1073/pnas.1016658108.

[7] V. Sourjik and H. C. Berg. “Functional Interactions between Receptors in Bacterial Chemotaxis”. In: *Nature* 428.6981 (2004), pp. 437–441. DOI: 10.1038/nature02406.

[8] R. Mesibov and J. Adler. “Chemotaxis Toward Amino Acids in *Escherichia Coli*”. In: *J. Bacteriol.* 112.1 (1972), pp. 315–326. DOI: 10.1128/jb.112.1.315-326.1972.

[9] S. T. Emlen. “MIGRATION: ORIENTATION AND NAVIGATION”. In: *Avian Biology*. Elsevier, 1975, pp. 129–219. DOI: 10.1016/B978-0-12-249405-5.50011-2.

[10] V. Narayan, S. Ramaswamy, and N. Menon. “Long-Lived Giant Number Fluctuations in a Swarming Granular Nematic”. In: *Science* 317.5834 (2007), pp. 105–108. DOI: 10.1126/science.1140414.

[11] J. Toner. “Giant Number Fluctuations in Dry Active Polar Fluids: A Shocking Analogy with Lightning Rods”. In: *J. Chem. Phys.* 150.15 (2019), p. 154120. DOI: 10.1063/1.5081742.

[12] J. Toner and Y. Tu. “Long-Range Order in a Two-Dimensional Dynamical XY Model: How Birds Fly Together”. In: *Phys. Rev. Lett.* 75.23 (1995), pp. 4326–4329. DOI: 10.1103/PhysRevLett.75.4326.

[13]J. Toner and Y. Tu. “Flocks, Herds, and Schools: A Quantitative Theory of Flocking”. In: *Phys. Rev. E* 58.4 (1998), pp. 4828–4858. DOI: 10.1103/PhysRevE.58.4828.

[14]T. Vicsek, A. Czirók, E. Ben-Jacob, I. Cohen, and O. Shochet. “Novel Type of Phase Transition in a System of Self-Driven Particles”. In: *Phys. Rev. Lett.* 75.6 (1995), pp. 1226–1229. DOI: 10.1103/PhysRevLett.75.1226.

[15]L. K. E. A. Abdelmohsen, F. Peng, Y. Tu, and D. A. Wilson. “Micro- and Nano-Motors for Biomedical Applications”. In: *J. Mater. Chem. B* 2.17 (2014), pp. 2395–2408. DOI: 10.1039/C3TB21451F.

[16]W. Gao and J. Wang. “The Environmental Impact of Micro/Nanomachines: A Review”. In: *ACS Nano* 8.4 (2014), pp. 3170–3180. DOI: 10.1021/nn500077a.

[17]W. F. Paxton, K. C. Kistler, C. C. Olmeda, et al. “Catalytic Nanomotors: Autonomous Movement of Striped Nanorods”. In: *J. Am. Chem. Soc.* 126.41 (2004), pp. 13424–13431. DOI: 10.1021/ja047697z.

[18]M. Vigelius, B. Meyer, and G. Pascoe. “Multiscale Modelling and Analysis of Collective Decision Making in Swarm Robotics”. In: *PLoS ONE* 9.11 (2014). Ed. by S. C. Pratt, e111542. DOI: 10.1371/journal.pone.0111542.

[19]L. M. Nash, D. Kleckner, A. Read, et al. “Topological Mechanics of Gyroscopic Metamaterials”. In: *Proc. Natl. Acad. Sci. U.S.A.* 112.47 (2015), pp. 14495–14500. DOI: 10.1073/pnas.1507413112.

[20]R. Dreyfus, J. Baudry, M. L. Roper, et al. “Microscopic Artificial Swimmers”. In: *Nature* 437.7060 (2005), pp. 862–865. DOI: 10.1038/nature04090.

[21]D. A. Wilson, R. J. M. Nolte, and J. C. M. van Hest. “Autonomous Movement of Platinum-Loaded Stomatocytes”. In: *Nat. Chem.* 4.4 (2012), pp. 268–274. DOI: 10.1038/nchem.1281.

[22]H.-R. Jiang, N. Yoshinaga, and M. Sano. “Active Motion of a Janus Particle by Self-Thermophoresis in a Defocused Laser Beam”. In: *Phys. Rev. Lett.* 105.26 (2010), p. 268302. DOI: 10.1103/PhysRevLett.105.268302.

[23]J. Yan, M. Han, J. Zhang, et al. “Reconfiguring Active Particles by Electrostatic Imbalance”. In: *Nat. Mater.* 15.10 (2016), pp. 1095–1099. DOI: 10.1038/nmat4696.

[24]A. Bricard, J.-B. Caussin, N. Desreumaux, O. Dauchot, and D. Bartolo. “Emergence of Macroscopic Directed Motion in Populations of Motile Colloids”. In: *Nature* 503.7474 (2013), pp. 95–98. DOI: 10.1038/nature12673.

[25]B. ten Hagen, S. van Teeffelen, and H. Löwen. “Brownian Motion of a Self-Propelled Particle”. In: *J. Phys.: Condens. Matter* 23.19 (2011), p. 194119. DOI: 10.1088/0953-8984/23/19/194119.

[26]P. Romanczuk, M. Bär, W. Ebeling, B. Lindner, and L. Schimansky-Geier. “Active Brownian Particles: From Individual to Collective Stochastic Dynamics”. In: *Eur. Phys. J. Spec. Top.* 202.1 (2012), pp. 1–162. DOI: 10.1140/epjst/e2012-01529-y.

[27]M. J. Schnitzer. “Theory of Continuum Random Walks and Application to Chemotaxis”. In: *Phys. Rev. E* 48.4 (1993), pp. 2553–2568. DOI: 10.1103/PhysRevE.48.2553.

[28]É. Fodor, C. Nardini, M. E. Cates, et al. “How Far from Equilibrium Is Active Matter?” In: *Phys. Rev. Lett.* 117.3 (2016), p. 038103. DOI: 10.1103/PhysRevLett.117.038103.

[29]J. U. Klamser, O. Dauchot, and J. Tailleur. “Kinetic Monte Carlo Algorithms for Active Matter Systems”. In: *Phys. Rev. Lett.* 127.15 (2021), p. 150602. DOI: 10.1103/PhysRevLett.127.150602.

[30]J. de Graaf, A. J. T. M. Mathijssen, M. Fabritius, et al. “Understanding the Onset of Oscillatory Swimming in Microchannels”. In: *Soft Matter* 12.21 (2016), pp. 4704–4708. DOI: 10.1039/C6SM00939E.

[31]M. J. Lighthill. “On the Squirming Motion of Nearly Spherical Deformable Bodies through Liquids at Very Small Reynolds Numbers”. In: *Comm. Pure Appl. Math.* 5.2 (1952), pp. 109–118. DOI: 10.1002/cpa.3160050201.

[32]J. R. Blake. “A Spherical Envelope Approach to Ciliary Propulsion”. In: *J. Fluid Mech.* 46.1 (1971), pp. 199–208. DOI: 10.1017/S002211207100048X.

[33]M. Kuron, P. Stärk, C. Burkard, J. de Graaf, and C. Holm. “A Lattice Boltzmann Model for Squirmers”. In: *J. Chem. Phys.* 150.14 (2019), p. 144110. DOI: 10.1063/1.5085765.

[34]A. Zöttl and H. Stark. “Simulating Squirmers with Multiparticle Collision Dynamics”. In: *Eur. Phys. J. E* 41.5 (2018), p. 61. DOI: 10.1140/epje/i2018-11670-3.

[35]J. Bialké, H. Löwen, and T. Speck. “Microscopic Theory for the Phase Separation of Self-Propelled Repulsive Disks”. In: *EPL* 103.3 (2013), p. 30008. DOI: 10.1209/0295-5075/103/30008.

[36]M. E. Cates. “Active Field Theories”. In: (2019). DOI: 10.48550/ARXIV.1904.01330.

[37]R. Di Leonardo, L. Angelani, D. Dell’Arciprete, et al. “Bacterial Ratchet Motors”. In: *Proc. Natl. Acad. Sci. U.S.A.* 107.21 (2010), pp. 9541–9545. DOI: 10.1073/pnas.0910426107.

[38]R. Brown. “XXVII. A Brief Account of Microscopical Observations Made in the Months of June, July and August 1827, on the Particles Contained in the Pollen of Plants; and on the General Existence of Active Molecules in Organic and Inorganic Bodies”. In: *Philos. Mag.* 4.21 (1828), pp. 161–173. DOI: 10.1080/14786442808674769.

[39]A. Einstein, R. Fürth, and A. Cowper. *Investigations on the Theory of the Brownian Movement*. Dover Publications, 1956.

[40]R. Kubo. “The Fluctuation-Dissipation Theorem”. In: *Rep. Prog. Phys.* 29.1 (1966), pp. 255–284. DOI: 10.1088/0034-4885/29/1/306.

[41]H. Risken. *The Fokker-Planck Equation: Methods of Solution and Applications*. Berlin, Heidelberg: Springer Berlin Heidelberg, 1984.

[42]L. Ornstein. “On the Brownian Motion”. In: *KNAW Proceedings* 21 (1919), pp. 96–108.

[43]T. Li, S. Kheifets, D. Medellin, and M. G. Raizen. “Measurement of the Instantaneous Velocity of a Brownian Particle”. In: *Science* 328.5986 (2010). DOI: 10.1126/science.1189403.

[44]R. Huang, I. Chavez, K. M. Taute, et al. “Direct Observation of the Full Transition from Ballistic to Diffusive Brownian Motion in a Liquid”. In: *Nat. Phys.* 7.7 (2011). DOI: 10.1038/nphys1953.

[45]R. Niu, T. Palberg, and T. Speck. “Self-Assembly of Colloidal Molecules Due to Self-Generated Flow”. In: *Phys. Rev. Lett.* 119.2 (2017), p. 028001. DOI: 10.1103/PhysRevLett.119.028001.

[46]J. Elgeti, R. G. Winkler, and G. Gompper. “Physics of Microswimmers—Single Particle Motion and Collective Behavior: A Review”. In: *Rep. Prog. Phys.* 78.5 (2015), p. 056601. DOI: 10.1088/0034-4885/78/5/056601.

[47]I. Theurkauff, C. Cottin-Bizonne, J. Palacci, C. Ybert, and L. Bocquet. “Dynamic Clustering in Active Colloidal Suspensions with Chemical Signaling”. In: *Phys. Rev. Lett.* 108.26 (2012), p. 268303. DOI: 10.1103/PhysRevLett.108.268303.

[48]A. T. Brown, W. C. K. Poon, C. Holm, and J. de Graaf. “Ionic Screening and Dissociation Are Crucial for Understanding Chemical Self-Propulsion in Polar Solvents”. In: *Soft Matter* 13.6 (2017), pp. 1200–1222. DOI: 10.1039/C6SM01867J.

[49]B. Liebchen and H. Löwen. “Which Interactions Dominate in Active Colloids?” In: *J. Chem. Phys.* 150.6 (2019), p. 061102. DOI: 10.1063/1.5082284.

[50]I. Buttinoni, J. Bialké, F. Kümmel, et al. “Dynamical Clustering and Phase Separation in Suspensions of Self-Propelled Colloidal Particles”. In: *Phys. Rev. Lett.* 110.23 (2013), p. 238301. DOI: 10.1103/PhysRevLett.110.238301.

[51]L. Giomi, N. Hawley-Weld, and L. Mahadevan. “Swarming, Swirling and Stasis in Sequestered Bristle-Bots”. In: *Proc. R. Soc. A.* 469.2151 (2013), p. 20120637. DOI: 10.1098/rspa.2012.0637.

[52]F. Kümmel, B. ten Hagen, R. Wittkowski, et al. “Circular Motion of Asymmetric Self-Propelling Particles”. In: *Phys. Rev. Lett.* 110.19 (2013), p. 198302. DOI: 10.1103/PhysRevLett.110.198302.

[53]B. Liebchen and D. Levis. “Collective Behavior of Chiral Active Matter: Pattern Formation and Enhanced Flocking”. In: *Phys. Rev. Lett.* 119.5 (2017), p. 058002. DOI: 10.1103/PhysRevLett.119.058002.

[54]J. T. Siebert, F. Dittrich, F. Schmid, et al. “Critical Behavior of Active Brownian Particles”. In: *Phys. Rev. E* 98.3 (2018), p. 030601. DOI: 10.1103/PhysRevE.98.030601.

[55]A. Peshkov, E. Bertin, F. Ginelli, and H. Chaté. “Boltzmann-Ginzburg-Landau Approach for Continuous Descriptions of Generic Vicsek-like Models”. In: *Eur. Phys. J.: Spec. Top.* 223 (2014). DOI: 10.1140/epjst/e2014-02193-y.

[56]N. N. Bogoliubov. “Kinetic Equations”. In: *Journal of Physics USSR* 10.3 (1945), pp. 265–274.

[57]T. Speck, A. M. Menzel, J. Bialké, and H. Löwen. “Dynamical Mean-Field Theory and Weakly Non-Linear Analysis for the Phase Separation of Active Brownian Particles”. In: *J. Chem. Phys.* 142.22 (2015), p. 224109. DOI: 10.1063/1.4922324.

[58]A. Fischer, A. Chatterjee, and T. Speck. “Aggregation and Sedimentation of Active Brownian Particles at Constant Affinity”. In: *J. Chem. Phys.* 150 (2019), p. 064910. DOI: 10.1063/1.5081115.

[59]P. Kloeden and E. Platen. *Numerical Solution of Stochastic Differential Equations*. Stochastic Modelling and Applied Probability. Springer Berlin Heidelberg, 2011.

[60]B. Dünweg and W. Paul. “BROWNIAN DYNAMICS SIMULATIONS WITHOUT GAUSSIAN RANDOM NUMBERS”. In: *Int. J. Mod. Phys. C* 02.03 (1991), pp. 817–827. DOI: 10.1142/S0129183191001037.

[61]J. D. Weeks, D. Chandler, and H. C. Andersen. “Role of Repulsive Forces in Determining the Equilibrium Structure of Simple Liquids”. In: *J. Chem. Phys.* 54 (1971), p. 5237. DOI: 10.1063/1.1674820.

[62]D. Frenkel and B. Smit. *Understanding Molecular Simulation: From Algorithms to Applications*. 2nd ed. Computational Science Series 1. San Diego: Academic Press, 2002.

[63]R. D. Mountain and A. C. Brown. “Molecular Dynamics Study of the Liquid and Plastic Phases of Neopentane”. In: *J. Chem. Phys.* 82.9 (1985), pp. 4236–4242. DOI: 10.1063/1.448812.

[64]S. M. Thompson and K. E. Gubbins. “Structure of the Liquid–Vapor Interface of Molecular Fluids: Homonuclear Diatomic Molecules”. In: *J. Chem. Phys.* 74.11 (1981), pp. 6467–6479. DOI: 10.1063/1.440985.

[65]J. G. Gay and B. J. Berne. “Modification of the Overlap Potential to Mimic a Linear Site–Site Potential”. In: *J. Chem. Phys.* 74.6 (1981), pp. 3316–3319. DOI: 10.1063/1.441483.

[66]M. Allen, M. Allen, D. Tildesley, D. Tildesley, and T. ALLEN. *Computer Simulation of Liquids*. Oxford Science Publ. Clarendon Press, 1989.

[67]J. O’Byrne, Y. Kafri, J. Tailleur, and F. van Wijland. “Time Irreversibility in Active Matter, from Micro to Macro”. In: *Nat. Rev. Phys.* 4.3 (2022), pp. 167–183. DOI: 10.1038/s42254-021-00406-2.

[68]I. S. Aranson. “Bacterial Active Matter”. In: *Rep. Prog. Phys.* 85.7 (2022), p. 076601. DOI: 10.1088/1361-6633/ac723d.

[69]R. Rusconi, J. S. Guasto, and R. Stocker. “Bacterial Transport Suppressed by Fluid Shear”. In: *Nature Phys* 10.3 (2014), pp. 212–217. DOI: 10.1038/nphys2883.

[70]A. Sokolov and I. S. Aranson. “Rapid Expulsion of Microswimmers by a Vortical Flow”. In: *Nat Commun* 7.1 (2016), p. 11114. DOI: 10.1038/ncomms11114.

[71]K. Tunstrøm, Y. Katz, C. C. Ioannou, et al. “Collective States, Multistability and Transitional Behavior in Schooling Fish”. In: *PLoS Comput Biol* 9.2 (2013). Ed. by E. Ben-Jacob, e1002915. DOI: 10.1371/journal.pcbi.1002915.

[72]A. Cavagna, I. Giardina, A. Orlandi, et al. “The STARFLAG Handbook on Collective Animal Behaviour: 1. Empirical Methods”. In: *Anim. Behav.* 76.1 (2008), pp. 217–236. DOI: 10.1016/j.anbehav.2008.02.002.

[73]A. Brown and W. Poon. “Ionic Effects in Self-Propelled Pt-coated Janus Swimmers”. In: *Soft Matter* 10.22 (2014), pp. 4016–4027. DOI: 10.1039/C4SM00340C.

[74]J. R. Gomez-Solano, S. Samin, C. Lozano, et al. “Tuning the Motility and Directionality of Self-Propelled Colloids”. In: *Sci Rep* 7.1 (2017), p. 14891. DOI: 10.1038/s41598-017-14126-0.

[75]S. Thutupalli, R. Seemann, and S. Herminghaus. “Swarming Behavior of Simple Model Squirmers”. In: *New J. Phys.* 13.7 (2011), p. 073021. DOI: 10.1088/1367-2630/13/7/073021.

[76]H. P. Zhang, A. Be’er, E.-L. Florin, and H. L. Swinney. “Collective Motion and Density Fluctuations in Bacterial Colonies”. In: *Proc. Natl. Acad. Sci. U.S.A.* 107.31 (2010), pp. 13626–13630. DOI: 10.1073/pnas.1001651107.

[77]U. Börner, A. Deutsch, H. Reichenbach, and M. Bär. “Rippling Patterns in Aggregates of Myxobacteria Arise from Cell-Cell Collisions”. In: *Phys. Rev. Lett.* 89.7 (2002), p. 078101. DOI: 10.1103/PhysRevLett.89.078101.

[78]H. H. Wensink, J. Dunkel, S. Heidenreich, et al. “Meso-Scale Turbulence in Living Fluids”. In: *Proc. Natl. Acad. Sci. U.S.A.* 109.36 (2012), pp. 14308–14313. DOI: 10.1073/pnas.1202032109.

[79]S. Prestipino, C. Caccamo, D. Costa, G. Malescio, and G. Munaò. “Shapes of a Liquid Droplet in a Periodic Box”. In: *Phys. Rev. E* 92.2 (2015), p. 022141. DOI: 10.1103/PhysRevE.92.022141.

[80]Y. Fily and M. C. Marchetti. “Athermal Phase Separation of Self-Propelled Particles with No Alignment”. In: *Phys. Rev. Lett.* 108.23 (2012), p. 235702. DOI: 10.1103/PhysRevLett.108.235702.

[81]A. Jayaram, A. Fischer, and T. Speck. “From Scalar to Polar Active Matter: Connecting Simulations with Mean-Field Theory”. In: *Phys. Rev. E* 101.2 (2020), p. 022602. DOI: 10.1103/PhysRevE.101.022602.

[82]R. Großmann, I. S. Aranson, and F. Peruani. “A Particle-Field Approach Bridges Phase Separation and Collective Motion in Active Matter”. In: *Nat. Commun.* 11.1 (2020), p. 5365. DOI: 10.1038/s41467-020-18978-5.

[83]F. D. C. Farrell, M. C. Marchetti, D. Marenduzzo, and J. Tailleur. “Pattern Formation in Self-Propelled Particles with Density-Dependent Motility”. In: *Phys. Rev. Lett.* 108.24 (2012), p. 248101. DOI: 10.1103/PhysRevLett.108.248101.

[84]S. Wiggins. *Introduction to Dynamical Systems.* Secaucus: Springer, 2003.

[85]R. P. Feynman. *The Feynman Lectures on Physics. Volume 1: Mainly Mechanics, Radiation, and Heat*. The new millennium edition, paperback first published. New York: Basic Books, 2011.

[86]P. Galajda, J. Keymer, P. Chaikin, and R. Austin. "A Wall of Funnels Concentrates Swimming Bacteria". In: *J. Bacteriol.* 189.23 (2007), pp. 8704–8707. DOI: 10.1128/JB.01033-07.

[87]M. B. Wan, C. J. Olson Reichhardt, Z. Nussinov, and C. Reichhardt. "Rectification of Swimming Bacteria and Self-Driven Particle Systems by Arrays of Asymmetric Barriers". In: *Phys. Rev. Lett.* 101.1 (2008), p. 018102. DOI: 10.1103/PhysRevLett.101.018102.

[88]G. Vizsnyiczai, G. Frangipane, C. Maggi, et al. "Light Controlled 3D Micromotors Powered by Bacteria". In: *Nat. Commun.* 8.1 (2017), p. 15974. DOI: 10.1038/ncomms15974.

[89]A. Sokolov, M. M. Apodaca, B. A. Grzybowski, and I. S. Aranson. "Swimming Bacteria Power Microscopic Gears". In: *Proc. Natl. Acad. Sci. U.S.A.* 107.3 (2010), pp. 969–974. DOI: 10.1073/pnas.0913015107.

[90]S. Krishnamurthy, S. Ghosh, D. Chatterji, R. Ganapathy, and A. K. Sood. "A Micrometre-Sized Heat Engine Operating between Bacterial Reservoirs". In: *Nat. Phys.* 12.12 (2016), pp. 1134–1138. DOI: 10.1038/nphys3870.

[91]Y. Baek, A. P. Solon, X. Xu, N. Nikola, and Y. Kafri. "Generic Long-Range Interactions Between Passive Bodies in an Active Fluid". In: *Phys. Rev. Lett.* 120.5 (2018), p. 058002. DOI: 10.1103/PhysRevLett.120.058002.

[92]C. F. Lee. "Active Particles under Confinement: Aggregation at the Wall and Gradient Formation inside a Channel". In: *New J. Phys.* 15.5 (2013), p. 055007. DOI: 10.1088/1367-2630/15/5/055007.

[93]H. H. Wensink and H. Löwen. "Aggregation of Self-Propelled Colloidal Rods near Confining Walls". In: *Phys. Rev. E* 78.3 (2008), p. 031409. DOI: 10.1103/PhysRevE.78.031409.

[94]J. Elgeti and G. Gompper. "Wall Accumulation of Self-Propelled Spheres". In: *EPL* 101.4 (2013), p. 48003. DOI: 10.1209/0295-5075/101/48003.

[95]F. Oosawa. "The History of the Birth of the Asakura–Oosawa Theory". In: *J. Chem. Phys.* 155.8 (2021), p. 084104. DOI: 10.1063/5.0049350.

[96]K. Inokuchi. "Mechanisms of Agglomeration of Red Cells by High Polymer Compounds". In: *Bull. Chem. Soc. Jpn.* 24.2 (1951), pp. 78–82. DOI: 10.1246/bcsj.24.78.

[97]B. R. Monaghan and H. L. White. "EFFECT OF PROTEINS ON ELECTROPHORETIC MOBILITY AND SEDIMENTATION VELOCITY OF RED CELLS". In: *J. Gen. Physiol.* 19.5 (1936), pp. 715–726. DOI: 10.1085/jgp.19.5.715.

[98]M. J. Geoghegan and R. C. Brian. "Aggregate Formation in Soil. 1. Influence of Some Bacterial Polysaccharides on the Binding of Soil Particles". In: *Biochem. J.* 43.1 (1948), pp. 5–13. DOI: 10.1042/bj0430005.

[99]C. Bondy. “The Creaming of Rubber Latex”. In: *Trans. Faraday Soc.* 35 (1939), p. 1093. DOI: 10.1039/tf9393501093.

[100]S. Asakura and F. Oosawa. “On Interaction between Two Bodies Immersed in a Solution of Macromolecules”. In: *J. Chem. Phys.* 22.7 (1954), pp. 1255–1256. DOI: 10.1063/1.1740347.

[101]S. Asakura and F. Oosawa. “Interaction between Particles Suspended in Solutions of Macromolecules”. In: *J. Polym. Sci.* 33.126 (1958), pp. 183–192. DOI: 10.1002/pol.1958.1203312618.

[102]H. N. W. Lekkerkerker, W. C.-K. Poon, P. N. Pusey, A. Stroobants, and P. B. Warren. “Phase Behaviour of Colloid + Polymer Mixtures”. In: *Europhys. Lett.* 20.6 (1992), pp. 559–564. DOI: 10.1209/0295-5075/20/6/015.

[103]H. Lekkerkerker. “Osmotic Equilibrium Treatment of the Phase Separation in Colloidal Dispersions Containing Non-Adsorbing Polymer Molecules”. In: *Colloids Surf.* 51 (1990), pp. 419–426. DOI: 10.1016/0166-6622(90)80156-X.

[104]Y. Mao, M. Cates, and H. Lekkerkerker. “Depletion Force in Colloidal Systems”. In: *Physica A* 222.1-4 (1995), pp. 10–24. DOI: 10.1016/0378-4371(95)00206-5.

[105]H. De Hek and A. Vrij. “Phase Separation in Non-Aqueous Dispersions Containing Polymer Molecules and Colloidal Spheres”. In: *J. Colloid Interface Sci.* 70.3 (1979), pp. 592–594. DOI: 10.1016/0021-9797(79)90067-5.

[106]H. De Hek and A. Vrij. “Interactions in Mixtures of Colloidal Silica Spheres and Polystyrene Molecules in Cyclohexane”. In: *J. Colloid Interface Sci.* 84.2 (1981), pp. 409–422. DOI: 10.1016/0021-9797(81)90232-0.

[107]E. Dickinson and J. M. Rodríguez-Patino. *Food Emulsions and Foams: Interfaces, Interactions and Stability*. Cambridge: Royal Society of Chemistry, 1999.

[108]R. Tuinier, E. ten Grotenhuis, C. Holt, P. A. Timmins, and C. G. de Kruif. “Depletion Interaction of Casein Micelles and an Exocellular Polysaccharide”. In: *Phys. Rev. E* 60.1 (1999), pp. 848–856. DOI: 10.1103/PhysRevE.60.848.

[109]L. Angelani, C. Maggi, M. L. Bernardini, A. Rizzo, and R. Di Leonardo. “Effective Interactions between Colloidal Particles Suspended in a Bath of Swimming Cells”. In: *Phys. Rev. Lett.* 107.13 (2011), p. 138302. DOI: 10.1103/PhysRevLett.107.138302.

[110]J. Dzubiella, H. Löwen, and C. N. Likos. “Depletion Forces in Nonequilibrium”. In: *Phys. Rev. Lett.* 91.24 (2003), p. 248301. DOI: 10.1103/PhysRevLett.91.248301.

[111]J. Harder, S. A. Mallory, C. Tung, C. Valeriani, and A. Cacciuto. “The Role of Particle Shape in Active Depletion”. In: *J. Chem. Phys.* 141.19 (2014), p. 194901. DOI: 10.1063/1.4900720.

[112]J. Schwarz-Linek, C. Valeriani, A. Cacciuto, et al. “Phase Separation and Rotor Self-Assembly in Active Particle Suspensions”. In: *Proc. Natl. Acad. Sci. U.S.A.* 109.11 (2012), pp. 4052–4057. DOI: 10.1073/pnas.1116334109.

[113] S. K. Das, S. A. Egorov, B. Trefz, P. Virnau, and K. Binder. “Phase Behavior of Active Swimmers in Depletants: Molecular Dynamics and Integral Equation Theory”. In: *Phys. Rev. Lett.* 112.19 (2014), p. 198301. DOI: 10.1103/PhysRevLett.112.198301.

[114] K. Hayashi and S.-i. Sasa. “The Law of Action and Reaction for the Effective Force in a Non-Equilibrium Colloidal System”. In: *J. Phys.: Condens. Matter* 18.10 (2006), pp. 2825–2836. DOI: 10.1088/0953-8984/18/10/008.

[115] P. Liu, S. Ye, F. Ye, K. Chen, and M. Yang. “Constraint Dependence of Active Depletion Forces on Passive Particles”. In: *Phys. Rev. Lett.* 124.15 (2020), p. 158001. DOI: 10.1103/PhysRevLett.124.158001.

[116] R. Ni, M. A. Cohen Stuart, and P. G. Bolhuis. “Tunable Long Range Forces Mediated by Self-Propelled Colloidal Hard Spheres”. In: *Phys. Rev. Lett.* 114.1 (2015), p. 018302. DOI: 10.1103/PhysRevLett.114.018302.

[117] L. R. Leite, D. Lucena, F. Q. Potiguar, and W. P. Ferreira. “Depletion Forces on Circular and Elliptical Obstacles Induced by Active Matter”. In: *Phys. Rev. E* 94.6 (2016), p. 062602. DOI: 10.1103/PhysRevE.94.062602.

[118] J. R. Gomez-Solano, S. Roy, T. Araki, S. Dietrich, and A. Maciołek. “Transient Coarsening and the Motility of Optically Heated Janus Colloids in a Binary Liquid Mixture”. In: *Soft Matter* 16.36 (2020), pp. 8359–8371. DOI: 10.1039/D0SM00964D.

[119] S. Paul, A. Jayaram, N. Narinder, T. Speck, and C. Bechinger. “Force Generation in Confined Active Fluids: The Role of Microstructure”. In: *Phys. Rev. Lett.* 129.5 (2022), p. 058001. DOI: 10.1103/PhysRevLett.129.058001.

[120] J. R. Howse, R. A. L. Jones, A. J. Ryan, et al. “Self-Motile Colloidal Particles: From Directed Propulsion to Random Walk”. In: *Phys. Rev. Lett.* 99.4 (2007), p. 048102. DOI: 10.1103/PhysRevLett.99.048102.

[121] T. Speck and R. L. Jack. “Ideal Bulk Pressure of Active Brownian Particles”. In: *Phys. Rev. E* 93.6 (2016), p. 062605. DOI: 10.1103/PhysRevE.93.062605.

[122] A. Argun, A.-R. Moradi, E. Pinçe, et al. “Non-Boltzmann Stationary Distributions and Nonequilibrium Relations in Active Baths”. In: *Phys. Rev. E* 94.6 (2016), p. 062150. DOI: 10.1103/PhysRevE.94.062150.

[123] T. Speck. “Collective Forces in Scalar Active Matter”. In: *Soft Matter* 16.11 (2020), pp. 2652–2663. DOI: 10.1039/D0SM00176G.

[124] G. Volpe, I. Buttinoni, D. Vogt, H.-J. Kümmerer, and C. Bechinger. “Microswimmers in Patterned Environments”. In: *Soft Matter* 7.19 (2011), p. 8810. DOI: 10.1039/c1sm05960b.

[125] X. Wang, S. Ramírez-Hinestrosa, J. Dobnikar, and D. Frenkel. “The Lennard-Jones Potential: When (Not) to Use It”. In: *Phys. Chem. Chem. Phys.* 22.19 (2020), pp. 10624–10633. DOI: 10.1039/C9CP05445F.

[126] F. Ginelli, F. Peruani, M. Bär, and H. Chaté. “Large-Scale Collective Properties of Self-Propelled Rods”. In: *Phys. Rev. Lett.* 104.18 (2010), p. 184502. DOI: 10.1103/PhysRevLett.104.184502.

[127]H. Reinken, S. H. L. Klapp, M. Bär, and S. Heidenreich. “Derivation of a Hydrodynamic Theory for Mesoscale Dynamics in Microswimmer Suspensions”. In: *Phys. Rev. E* 97.2 (2018), p. 022613. DOI: 10.1103/PhysRevE.97.022613.

[128]X.-q. Shi and H. Chaté. *Self-Propelled Rods: Linking Alignment-Dominated and Repulsion-Dominated Active Matter*. 2018. arXiv: 1807.00294 [cond-mat].

[129]B. Liebchen and D. Levis. *Chiral Active Matter*. 2022. arXiv: 2207.01923 [cond-mat, physics:physics].

[130]M. Zeitz, K. Wolff, and H. Stark. “Active Brownian Particles Moving in a Random Lorentz Gas”. In: *Eur. Phys. J. E* 40.2 (2017), p. 23. DOI: 10.1140/epje/i2017-11510-0.

[131]C. Sándor, A. Libál, C. Reichhardt, and C. J. Olson Reichhardt. “Dynamic Phases of Active Matter Systems with Quenched Disorder”. In: *Phys. Rev. E* 95.3 (2017), p. 032606. DOI: 10.1103/PhysRevE.95.032606.

[132]C. Reichhardt and C. J. Olson Reichhardt. “Active Matter Transport and Jamming on Disordered Landscapes”. In: *Phys. Rev. E* 90.1 (2014), p. 012701. DOI: 10.1103/PhysRevE.90.012701.

[133]N. P. Kaur, S. Majhi, N. K. Dhami, and A. Mukherjee. “Healing Fine Cracks in Concrete with Bacterial Cement for an Advanced Non-Destructive Monitoring”. In: *Construction and Building Materials* 242 (2020), p. 118151. DOI: 10.1016/j.conbuildmat.2020.118151.

[134]I. Lazar, I. G. Petrisor, and T. F. Yen. “Microbial Enhanced Oil Recovery (MEOR)”. In: *Pet. Sci. Technol.* 25.11 (2007), pp. 1353–1366. DOI: 10.1080/10916460701287714.

[135]L. R. Brown. “Microbial Enhanced Oil Recovery (MEOR)”. In: *Curr. Opin. Microbiol.* 13.3 (2010), pp. 316–320. DOI: 10.1016/j.mib.2010.01.011.

[136]S. Sacanna, W. T. M. Irvine, P. M. Chaikin, and D. J. Pine. “Lock and Key Colloids”. In: *Nature* 464.7288 (2010), pp. 575–578. DOI: 10.1038/nature08906.

[137]E. Velasco, A. M. Somoza, and L. Mederos. “Liquid-crystal Phase Diagram of the Gay–Berne Fluid by Perturbation Theory”. In: *J. Chem. Phys.* 102.20 (1995), pp. 8107–8113. DOI: 10.1063/1.469222.

[138]R. Berardi, A. P. J. Emerson, and C. Zannoni. “Monte Carlo Investigations of a Gay—Berne Liquid Crystal”. In: *J. Chem. Soc. Faraday Trans.* 89.22 (1993), pp. 4069–4078. DOI: 10.1039/FT9938904069.

List of publications

Parts of this thesis are extensions and/or adaptations of the following peer-reviewed publications:

- A. Jayaram, A. Fischer, and T. Speck. *From scalar to polar active matter: Connecting simulations with mean-field theory*. Phys. Rev. E **101**, 022602 (2020).
  DOI: 10.1103/PhysRevE.101.022602
  Contribution: I developed the simulation code, derived the theory together with A. Fischer and T. Speck, prepared the figures and contributed to writing the manuscript.

- T. Speck and A. Jayaram. *Vorticity Determines the Force on Bodies Immersed in Active Suspensions*. Phys. Rev. Lett. **126**, 138002 (2021).
  DOI: 10.1103/PhysRevLett.126.138002
  Contribution: I performed the simulations and checked the validity of the theory using them. T. Speck derived the theory which I followed and verified. All authors contributed to preparing the figures and writing the manuscript.

- S. Paul, A. Jayaram, N. Narinder, T. Speck, and C. Bechinger. *Force generation in confined active fluids: The role of microstructure*. Phys. Rev. Lett. **129**, 058001 (2022).
  DOI: 10.1103/PhysRevLett.129.058001
  Contribution: I performed the simulations, obtained the analytical theory together with T. Speck and prepared the figures in the supplementary information. T. Speck and C. Bechinger planned the outline of the manuscript and all authors contributed to writing it.

Other works published or submitted during the PhD program:

- B. Deußen, A. Jayaram, F. Kummer, Y. Wang, T. Speck, and M. Oberlack. *High-order simulation scheme for active particles driven by stress boundary conditions*.

J. Phys.: Condens. Matter **33**, 244004 (2021).
DOI: 10.1088/1361-648X/abf8cf

- M. Gerhard, A. Jayaram, A. Fischer, and T. Speck. *Hunting active Brownian particles: Learning optimal behavior*. Phys. Rev. E **104**, 054614 (2021).
  DOI: 10.1103/PhysRevE.104.054614

- F. Siebers, A. Jayaram, P. Blümler, and T. Speck. *Exploiting compositional disorder in collectives of light-driven circle walkers*. Submitted.

Colophon

This thesis was typeset with LaTeX 2_ε. It uses the *Clean Thesis* style developed by Ricardo Langner. The design of the *Clean Thesis* style is inspired by user guide documents from Apple Inc.

Download the *Clean Thesis* style at `http://cleanthesis.der-ric.de/`.